5-2018

Development and Characterization of Lithium Indium Diselenide for Neutron Detection and Imaging Applications

Daniel Shane Hamm
University of Tennessee, dhamm@vols.utk.edu

To the Graduate Council:

I am submitting herewith a dissertation written by Daniel Shane Hamm entitled "Development and Characterization of Lithium Indium Diselenide for Neutron Detection and Imaging Applications." I have examined the final electronic copy of this dissertation for form and content and recommend that it be accepted in partial fulfillment of the requirements for the degree of Doctor of Philosophy, with a major in Nuclear Engineering.

Eric D. Lukosi, Major Professor

We have read this dissertation and recommend its acceptance:

Jason P. Hayward, Maik K. Lang, Mariya Zhuravleva

Accepted for the Council:

Dixie L. Thompson

Vice Provost and Dean of the Graduate School

(Original signatures are on file with official student records.)

Development and Characterization of Lithium Indium Diselenide for Neutron Detection and Imaging Applications

A Dissertation Presented for the

Doctor of Philosophy

Degree

The University of Tennessee, Knoxville

Daniel Shane Hamm

May 2018

This dissertation is dedicated to my wife, Molly Hamm, for her unparalleled kindness and support along this journey, to my mother, Lori Perry, for her love, dedication, and constant encouragement, to my brother, Dustin Hamm, for always leading by example, and to my grandmother, Mary Whitten, for first fostering my thirst for knowledge.

Acknowledgments

Abstract

Lithium indium diselenide [LISe] is under development as a single crystal semiconductor detector for neutron detection applications. Enriched in lithium-6, a neutron sensitive isotope, this wide-band gap semiconductor possesses the inherent neutron-gamma discrimination afforded by the thermal neutron capture reaction energy while providing distinct efficiency advantages over lithiated conversion layer detectors. The overarching theme of this work is to characterize the fundamental properties of this material to optimize its performance in neutron detection applications. The work presented here includes the identification of a suitable metallurgical contact for advanced detector fabrication, fundamental electronic property characterization, and proof-of-principle fast neutron imaging performance. Candidate contact materials were deposited through radio frequency magnetron sputtering. The primary metrics used to identify a robust contact were adhesion to the LISe surface and current voltage characteristics. Among the numerous contacts investigated, indium demonstrated the best adhesion properties. Its viability was demonstrated through the fabrication of a pixelated thermal neutron imaging detector (LTNI). Charge generation, transport, and trapping properties were investigated with emphasis on the stability of these properties post-operation in high thermal neutron flux fields. Neutron and alpha spectroscopy, photoinduced current transient spectroscopy, Raman spectroscopy, trap-filled limited voltage, and photoconductivity measurements were used to probe the charge transport and trapping mechanisms. Moderate transport properties were identified with respect to comparable technologies. Defect studies demonstrated that the type and density of defects strongly influenced performance of the detector. Encouraged by the performance of LTNI, an imaging detector was fabricated by coupling a LISe crystal to a 256×256 channel Timepix Application Specific Integrated Circuit to maximize spatial resolution.

The fast neutron spatial resolution for 9 MeV [electron-Volts] neutrons was investigated via a knife edge experiment. The measured efficiency was in agreement with the Evaluated Nuclear Data File cross-section database. The ultimate spatial resolution of the system was determined as 1.55 millimeters via the 10-90% decrease in contrast of the one-dimensional edge spread function. In conclusion, this material has been shown to exhibit suitable properties warranting further development for high efficiency slow neutron applications guided by the results of this work.

Table of Contents

List of Tables

List of Figures

xvii

Chapter 1

Introduction

1.1   Motivation

Neutron detection is an inherently difficult task due to the low probability of interaction with matter. Despite this (and because of it), there are a wealth of applications for neutron detection ranging from space exploration to national security to dosimetry. A perceived shortage of ^{3}He, the current gold standard for neutron detection, prompted a surge of research and developmental of new detection materials. Increased efficiency, faster signals, better neutron-γ discrimination, lower power, reduced cost, and more compact designs are among the most coveted improvements. Among the myriad of applications, neutron radiography is one of the most demanding due, in part, to the combination of high detection efficiency, spatial resolution, and fast timing requirements. Consequently, significant effort has been focused on the improvement of current detector technologies and new detection materials.

For a novel detector material or design, it is necessary to characterize their inherent properties as a part of the vetting process. This work is dedicated to developing a fundamental understanding of the ternary chalcogenide LiInSe$_2$ (LISe) as neutron detection material and provide a proof-of-principle for fast neutron imaging. LISe possesses inherent advantages over similar detection materials due to the incorporation of neutron sensitive ^{6}Li into the bulk crystal. Its unique scintillation and semiconduction properties provide parallel detector development avenues for a host of applications, especially where small detector sizes are desirable.

1.2 Novel Contributions

Future improvements in detector technology require an thorough understanding of the charge carrier transport properties in order to hone the growth process and optimize detector performance. Additionally, there is no data on the performance of LISe under high flux irradiation and its resistance to radiation damage, which is an important factor in long-term operation in commercial applications. Furthermore, commercialization requires the identification of a robust ohmic contact that facilitates detector packaging. Finally, LISe is capable of reducing integration time in neutron-imaging applications due to its inherent detection efficiency, requiring further investigation into its fundamental capabilities and limitations for radiography. This work seeks to fill these knowledge gaps and provide a guiding direction for application-specific development of LISe.

Chapter 2

Semiconductor Radiation Detectors

2.1 Theory of Operation

The development of solid state radiation detectors began, in earnest, in the mid-twentieth century when van Heerden [1–3] expanded earlier works on gas ionization chambers [4] and photoconduction [5–7]. Van Herdeen's silver chloride crystal counters were the first devices capable of particle detection. Shortly thereafter, a search for materials with similar properties unearthed promising candidates, such as thallium bromide [8–11]. From there, developments in crystal growth, pn junction detectors, and compound semiconductors spurred the evolution of the robust array of semiconductor radiation detectors available today [12–15].

2.1.1 Metals, Insulators, and Semiconductors

Semiconductors occupy a gray zone between insulators and conductors defined by the conductivity/resistivity, denoted as σ/ρ, of the material. Resistivity and its reciprocal, conductivity, quantify a material's ability to resist current flow when exposed to an external potential. These properties are governed by the material's electronic band structure, which is defined by the relative distance between the valence and conduction bands in energy space. The valence band, the outermost shell of electrons, is the highest energy state an electron can occupy without an excitation source. The lowest unfilled state is the conduction band, where electrons are only loosely bound to the nucleus and are generally free to drift and

3

diffuse from atom to atom. As its name suggests, the conduction band allows electrons to move or drift freely through a material. The forbidden region between these conduction bands in ideal insulators and semiconductors is devoid of quantum states (Figure 2.1). This space is characterized by the energy required to excite an electron from the top of the valence band to the conduction band (band gap energy) and the energy where 50% of the energy states are filled (Fermi level).

Lattice spacing and crystal structure dictate the size of the band gap. As such, both pressure and temperature exhibit slight influences [17–19]. The distribution of electrons within the available states in the conduction band is highly dependent on the thermal energy available to excite electrons from the valence band into the conduction band, which is described by the Fermi-Dirac distribution, $f(\epsilon)$,

$$f(\epsilon) = \frac{1}{\exp\left(\frac{(\epsilon - E_F)}{kT}\right) + 1} \tag{2.1}$$

where ϵ is the energy level in eV, k is the Boltzmann constant in eV/K, and T is the absolute temperature in Kelvin. Consequently, the density of electrons in the conduction
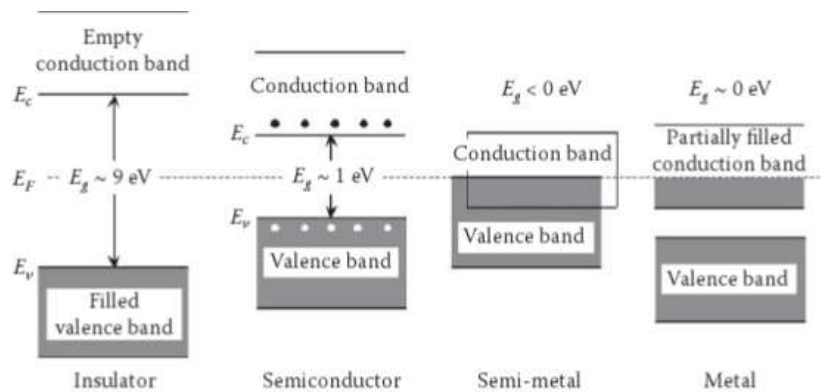
Figure 2.1: Energy band diagrams for insulator, semiconductor, semimetal, and metal. Insulators have a very large band gap resulting in low conductivity ($10^{-14} - 10^{-18}$ S/cm. Semimetals and metals have negligible band gaps and high conducitivity. Semiconductor band gaps range from 1 to several eV allowing limited current flow under sufficiently large voltages.The Fermi energy level, E_F, is a theoretical energy level related to the density of available states and the distributions of electrons within these states [16]

.

band is directly proportional to temperature as shown in Equation 2.1, which is integral to the performance and operation of semiconductor devices [20, 21].

2.1.2 Charge Carrier Generation, Transport, and Recombination

When discussing the nature of semiconductor devices, it is helpful to consider the distribution and transport of electrons within the conduction band as a pair of charge carriers. An electron excited into the conduction band always leaves behind a positively charged vacant state in the valence band, which often referred to as a hole. Generation of the electron-hole pairs requires an excitation source to transfer energy to the bound valence electron. Energy deposition and subsequent excitation can occur thermally or via interactions with electromagnetic or particle radiation, which will be further discussed in Chapter 3. Ionization energy (W) represents the average energy required to produce an electron-hole pair within a detection material. Intuitively, this value should be proportional to the band gap of the material since it is the minimum energy required to elevate an electron from the valence band to the conduction band. There are inherent losses in the energy transfer process that limits the conversion of deposited energy and the number of electron-hole pairs generated. Klein quantified the dependence of ionization energy on band gap based on experimental data from a wide range of semiconductor materials spanning 1-5 eV. The resulting phemonological model, as shown in Equation 2.2, accounts for optical phonon losses $[r(h\omega_r)]$, residual kinetic energy of the excited electron, and the band gap (E_G) [17].

$$W = \frac{14}{5}E_G + r(h\omega_r), [0.5 \leq r(h\omega_r) \leq 1.0eV] \tag{2.2}$$

The total charge generated by incident radiation, Q_0, is dependent on the number of charge carriers generated, N, and the elementary charge of an electron, q. For a given energy deposition of E, we find that

$$Q_0 = qN = \frac{qE}{W} \tag{2.3}$$

The proportionality of charge to energy in Equation 2.3 is the fundamental premise of radiation detection. The dissociated electron-hole pairs are free to drift or diffuse separately within their respective bands, giving rise to Equation 2.4,

$$\sigma = q(\mu_e e + \mu_h h) \tag{2.4}$$

where q is the electronic charge, e and h are the density of electrons and holes, respectively, and $u_{e,h}$ is the mobility of the charge carrier [22]. Charge-carrier mobility is a material-dependent proportionality factor relating the drift velocity of a charge-carrier to the applied electric field. Since the current flowing through a material is dependent on the drift velocity of charge carriers as described by the Shockley-Ramo theorem [23, 24], the performance of a semiconductor radiation detector is highly dependent on a large mobility [16].

Since electrons seek to occupy the lowest energy state, electron-hole pairs will recombine when they are are within close proximity to one another such that, in an equilibrium state, the recombination rate is equal to the generation rate. The charge-carrier lifetime, τ, is the average time an electron or hole remains liberated before recombining with its counterpart or becoming trapped. Due to inherent differences in free carrier concentrations for each charge carrier, their mobility within their respective bands, and the relative concentration of trapping sties, the lifetime of electrons and holes can differ by orders of magnitude. The mean lifetime is composed of three components representing the different modes of recombination. First, excess energy is emitted as a photon and/or as a phonon via lattice vibrations during direct band-to-band recombination. Secondly, a three-body de-excitation process transfers energy to another electron known as Auger recombination. Lastly, recombination is assisted by an intermediate state within the forbidden gap via Shockely-Read-Hall recombination. The relative size and prominence of these recombination modes are both highly dependent on the direct/indirect nature of the band gap (τ_{rad}), the availability of free carriers (τ_{Aug}), and the density of intermediate, or trap, states (τ_{SRH}). Larger values of τ are desirable in semiconductor radiation detectors, allowing charge to be collected before recombining [25].

2.1.3   Defects and Charge Trapping

Shockley-Read-Hall recombination is particularly important in radiation detection for both semiconductors and scintillators, a related material-dependent phenomenon. In a perfect crystalline lattice, these recombination sites, or trap states, are not present within the forbidden gap. These sites exist due to local band bending at crystallographic defects within the single-crystal lattice. The umbrella term defects covers a wide range of imperfections that can exist, often categorized as point, line, planar, and bulk defects. While each of these impact the behavior of a material, point defects are emphasized here for their influence at the most fundamental level of semiconductor device operation.

Point defects encompass a range of defect types that involve a single or pair of lattice sites. The primary defects impacting semiconductor device operation include vacancy, interstitial, and substitutional defects. For a binary compound semiconductor, AB, as shown in Figure 2.2, the absence of A or B in the crystalline lattice induces a strain on the bonds surrounding the vacancy $(V_{A/B})$, causing neighboring bonds to stretch thereby creating a localized deviation in the electronic band structure.
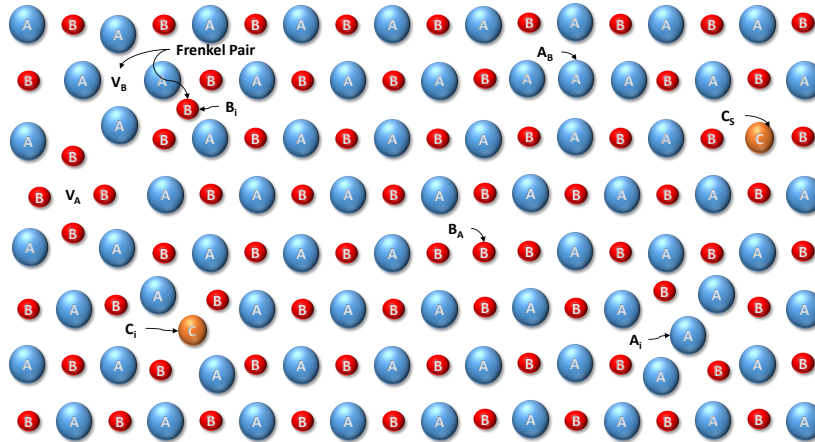
Figure 2.2: Binary compound semiconductor, AB, lattice with relevant point defects. The vacancies (V_A, V_B), interstitials (A_i, B_i, C_i), substitutional defects (C_s), and antisites (A_B, B_A) create localized perturbations in the electronic band structure leading to intermediate states within the forbidden gap. These defect states act as charge carrier traps and recombination centers.

Interstitials (X_i) and substitutional (X_s) defects induce stresses on the nearby lattice. Interstitial defects occupy a space within the crystallographic framework, but not on one of the primary lattice positions of the pure material. Conversely, substitutional defects are created when an atom occupies a lattice site that is typically occupied by another atom. These defects can be caused from an impurity atom or by a displaced atom within the lattice. The latter case gives rise to Frenkel pairs (adjacent interstitial-vacancy pairs) and antisites (lattice atoms occupy their counterpart's lattice position).

The influence of defect states depends on the size and charge of the displaced atom, the lattice spacing, and the density of states in the valence and conduction bands. Charge-carrier lifetime is a combination of the energy of defect states, their spatial distribution, and their capture cross-section. The capture cross-section, $\sigma_{e/h}$, is temperature-dependent, fundamental property that quantifies the probability that an electron or hole will be captured. Defect states with very large capture cross-sections ($> 10^{-16}\ cm^2$) for both electrons and holes are primarily responsible for electron-hole pair recombination [25]. Conversely, defect states that preferentially trap electrons or holes immobilize a free charge carrier such that it is unavailable for recombination or collection via an electric field. These trap states are said to be electrically active.

2.1.4   Defect States in Semiconductors and Scintillators

Here, it is important to introduce the analog to semiconductor radiation detectors, scintillators, since their operation depends on trap-assisted radiative recombination. Scintillation is the process of photonic emission in the visible light range from radiative recombination in these intermediate defect states. This holds true for inorganic scintillators, whereas the scintillation mechanism in organic materials operate at a molecular level and not the crystalline lattice [26]. Exemplary scintillation materials are transparent to their own emission wavelengths and have very short recombination lifetimes, such that doping the material with a specific impurity with a desired trap energy improves their performance. Conversely, semiconductor detector performance is negatively impacted by trap states, as they are an avenue for charge loss. Both detector types suffer from high concentrations of single-carrier trap states [16].

2.2 Device Fabrication and Charge Collection

Collecting the generated charge requires the application of an electrical potential to the detector material in order to separate the electron-hole pairs before trapping or recombination can occur. As these charges drift apart, their movement can be detected as a transient current proportional to the number of charge carriers drifting within an applied electric field. From Equation 2.3, the number of charge carriers available in the conduction band is directly proportional to the energy deposited in the system. Detectors are typically built in a planar configuration with electrical contacts on opposing faces of a semiconductor slab although more sophisticated structures are used for particular detector materials and applications [27].

2.2.1 Electrical Contacts

The electrical contacts can be ohmic (non-rectifying) or Schottky (rectifying), depending on the detector material and its electronic properties. Contact material selection and deposition is an important and difficult aspect of semiconductor device fabrication as it requires a delicate balance of material compatibility and leakage current. Rectifying, often referred to as blocking or non-injecting contacts, are typically used for low band-gap materials in order to reduce leakage current. Leakage current is the steady-state flow of electrons in a material under bias in the absence of an excitation source like ionizing radiation. Reducing leakage current improves signal-to-noise ratio for radiation-induced currents thereby increasing detector performance. Many detectors require leakage currents on the order of nA in order to observed radiation-induced currents above the noise floor [26].

Depending on the semiconductor band gap and free carrier concentration, contacts can range from completely ohmic to completely Schottky. Ohmic contacts have no influence on the current flow through the detector, producing a current-voltage relationship that follows Ohm's Law ($V = IR$). Schottky contacts block current flow in one direction by disallowing one charge carrier from entering the system, increasing the resistivity of the integrated semiconductor-contact structure, which effectively reduces leakage current.

This phenomenon is produced at the interface of the semiconductor heterojunction as the electronic band structure of the two materials flex to accommodate one another [28].

The Schottky barrier is an energy disparity that exists between the two dissimilar materials, and its height dictates the magnitude of the rectification. This effect plays an important role in the development of junction-based detectors, which are not the focus of this work ([26, 29, 30]). For wide-bandgap materials capable of operating at room-temperature with minimal leakage current, ohmic and Schottky contacts are both widely used, depending on the material. Ohmic contacts are preferred, assuming leakage current is sufficiently suppressed, due to inherent limitations in current-voltage linearity over the operational range and large contact resistance of Schottky contacts [16].

Robust ohmic contacts should be stable and provide minimal contact resistance. Additionally, the contact material should strongly adhere to the detector material since it is the interface between the semiconductor and the accompanying peripheral equipment used to collect and interpret the response to incident radiation. For example, coupling of semiconductor detectors to readout electronics is often achieved via wire bonding, a process similar to welding where a thin wire is ultrasonically heated in direct contact with the semiconductor contact [31]. Finding a suitable contact material that is ohmic and provides sufficient adhesion to withstand wire bonding is often difficult in practice. The composition of the wire and bond pad, temperature, and ultrasonic frequency play a role in the survivability and longevity of the bond. Additionally, the amalgamation of the contact metal and the wire has some influence on the electronic properties of the system due to complex interfaces and the introduction of surface defects. These effects can be mitigated through the use of very thick ($\geq 1\mu m$) contacts and elevated bonding temperatures to reduce the force and sonication power required to complete the bond [31–33].

2.2.2   Carrier Drift and Charge Collection

Under the influence of the applied electric field, the electron and holes drift towards the anode and cathode, respectively. The movement of these charges induces a reciprocal current on the electrodes according to the Shockley-Ramo Theorem. This theorem relates the current,

I, on an electrode to the charge, q, electric field, E, and the drift velocity of the charge carrier, v_d, as shown in Equation 2.5 [23, 24].

$$I = qEv_d \qquad (2.5)$$

The drift velocity of a charge carrier is a function of the previously discussed charge-carrier mobility, $\mu_{e/h}$, and the electric field according to

$$v_d = \mu E \qquad (2.6)$$

However, if the applied electric field is sufficiently high, the drift velocity begins to saturate such that the drift velocity becomes [34]

$$v_d = \frac{\mu E}{(1 + (\frac{\mu E}{v_s})^\alpha)^{1/\alpha}} \qquad (2.7)$$

where v_s is the saturation velocity and α is a constant. Figure 2.3 illustrates this effect. At low electric fields, the relationship is linear until reaching a saturation velocity at high electric fields, as seen for silicon. More complex semiconductor materials, like gallium arsenide, will display a more complicated relationship between electric field and drift velocity.

Combining drift velocity with the trapping time constant of the material, τ, gives the trapping length ($\mu\tau E$), sometimes referred to as *schubweg*, representing the average distance between trapping events. Ideally, this value should be much larger than the distance between the two electrodes, d, such that the probability of a charge carrier being trapped (or recombining) is very low so that all charge generated by the incident radiation may be collected.

Since the two charge carriers are independent of one another and exhibit their own mobility and lifetime (trapping time), the current induced in the system will be different. Assuming there is no trapping, the drift current density, J, can be given by

$$J = (q_e\mu_e + q_h\mu_h)E \qquad (2.8)$$

11
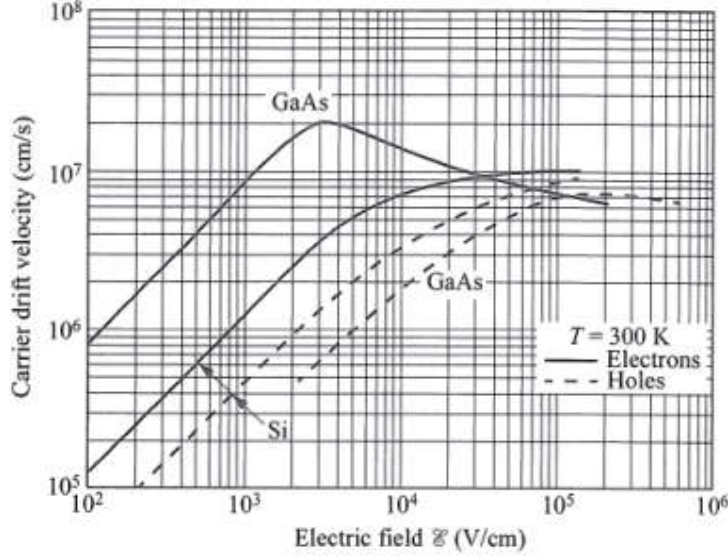
Figure 2.3: Saturation velocity as a function of electric field for Si and GaAs for both electrons and holes [29].

The ramifications of this relation is the dependence of the induced current on the slower (less-mobile) charge carrier. Now the charge induced on the collecting electrode from the charge generated by the incident radiation, Q_0, at distance, x, from the anode as a function of time, t, is given by the relation:

$$Q(t) = Q_0 \left[\frac{\mu_e \tau_e E}{d} \left(1 - exp\left(-\frac{t}{\tau_e}\right) \right) + \frac{\mu_h \tau_h E}{d} \left(1 - exp\left(-\frac{t}{\tau_h}\right) \right) \right] \qquad (2.9)$$

Integrating Equation 2.9 over the total transit time, $t_r = d/v_d$, gives the Hecht relation:

$$\frac{Q}{Q_0} = \left[\frac{\mu_e \tau_e E}{d} \left(1 - exp\left(-\frac{x}{\mu_e \tau_e E}\right) \right) + \frac{\mu_h \tau_h E}{d} \left(1 - exp\left(-\frac{d-x}{\mu_h \tau_h E}\right) \right) \right] \qquad (2.10)$$

where Q/Q_0 is known as the charge collection efficiency, CCE, of the detector. From Equation 2.10, it is clear that the significant differences in the electron and hole transport parameters, μ and τ, creates a position dependency in the response function of the detector, as shown in Figure 2.4. Charge-carrier mobility-lifetime products are usually much closer than the three orders of magnitude shown in Figure 2.4, but the stark contrast effectively illustrates the influence of the $\mu\tau$ product on charge collection efficiency.
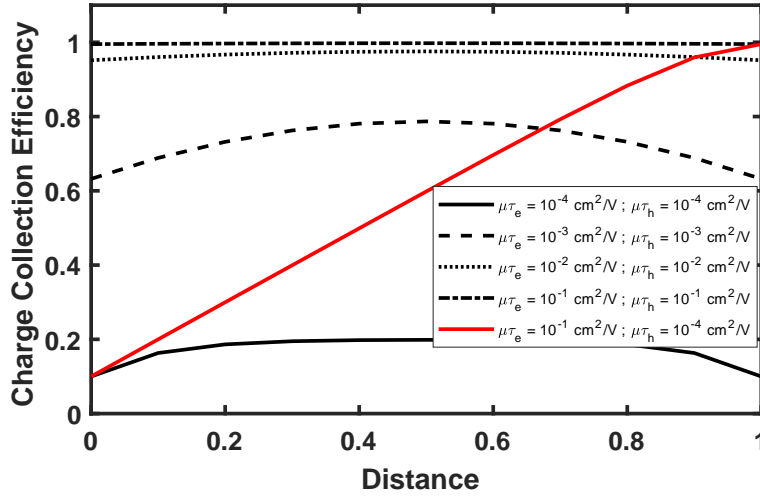
Figure 2.4: Charge collection efficiency as a function of position between the anode and the cathode. The black traces show equivalent $\mu\tau$ products for electrons and holes. The red trace illustrates a situation where one charge carrier (electrons) has a significantly larger mobility-lifetime product than the other (holes).

Since semiconductor radiation detectors are predicated on accurately representing the energy deposited within the device, materials with vastly different mobility-lifetime products are undesirable, often requiring more sophisticated techniques to produce reliable results [27]. Intuitively, charge collection efficiency asymptotically approaches unity as you increase the electric field due to a proportional decrease in the trapping length, which is important for materials with poor charge transport properties. As a consequence, semiconductor radiation materials have an operation voltage range known as the saturation region similar to the ion saturation region in gas-filled detectors. For reference, widely used semiconductor materials silicon and germanium have very large ($\mu\tau > 1 \ cm^2/V$) mobility-lifetime products. Materials like gallium arsenide ($10^{-4} cm^2/V$) and cadmium zinc telluride ($10^{-2} cm^2/V$) have electron $\mu\tau_e$ products that are two order of magnitude larger than hole $\mu\tau$ products [16].

2.2.3 Charge Integration, Shaping, and Amplification

Charge drift induced currents are typically small for even large energy depositions. An energy deposition of 1 MeV into a material with an electron-hole pair ionization energy of 10 eV generates 100,000 e-h pairs with a total charge of 16.2 fC. In order to detect this

small charge, a charge sensitive preamplifier is required to integrate the current and convert the current pulse into a voltage pulse. The time constant of the preamplifier must be long compared the duration of the current pulse, which is equal to the transit time of the charge carriers. Figure 2.5 depicts the typical processing chain for a planar detector configuration. The rise time of the preamplifier output voltage signal is a combination of the rise time of the preamplifier and the transit time of the charge carriers. The amplitude of the voltage pulse is directly proportional to the charge generated by the incident radiation. The preamplifier pulse is shaped and amplified by a linear amplifier preserving the functional relationship between pulse height (amplitude) and radiation energy.

Pulse height spectra (PHS) built from the frequency distribution of accumulations of thousands of voltage pulses can be used to identify the radiation source. The fidelity of these spectra are dependent on the charge collection efficiency and charge carrier transport properties of the detection material, the proportionality of the pulse processing chain, and the system noise. Expanding on the charge collection efficiency discussion, a monoenergetic particle depositing all of its energy within the bulk of the detection material uniformly across the detector can produce the spectra shown in Figure 2.6. Higher mobility-lifetime products, assuming all other parameters constant, produce larger voltage pulses, which becomes increasingly important for low-energy radiation. While poor transport properties are undesirable, energy calibrations can be used to compensate for the low-output pulses. Dissimilarities in electron and hole transport properties present much more deleterious effects for the spectroscopic capabilities of a given detector material as can be seen in Figure 2.6.

2.3 Summary

This chapter briefly covered the properties of semiconductor radiation detectors with a specific focus on the role charge transport properties play in detector operation. In the development of novel detection materials, these properties are often the first to be studied in order to quantify their viability as radiation detectors. Even for well-developed materials, significant research is directed towards improving the charge transport properties or circumventing their contributions. Semiconductor radiation detectors occupy a significant
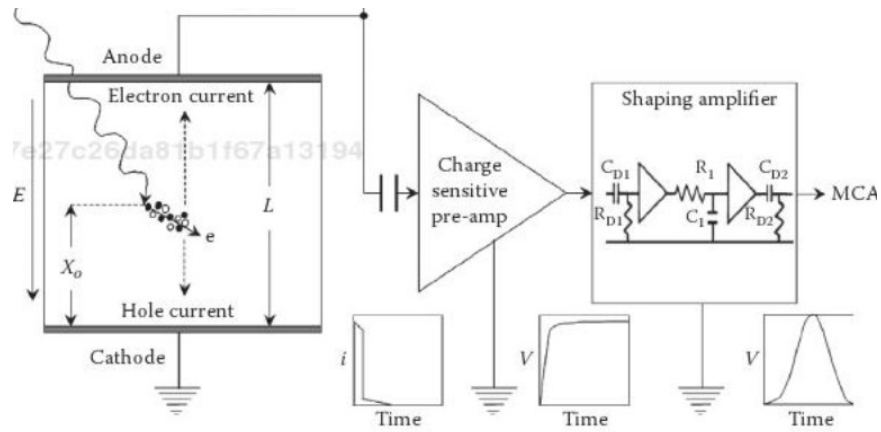
Figure 2.5: Pulse processing chain for semiconductor radiation detectors operated in pulse mode.
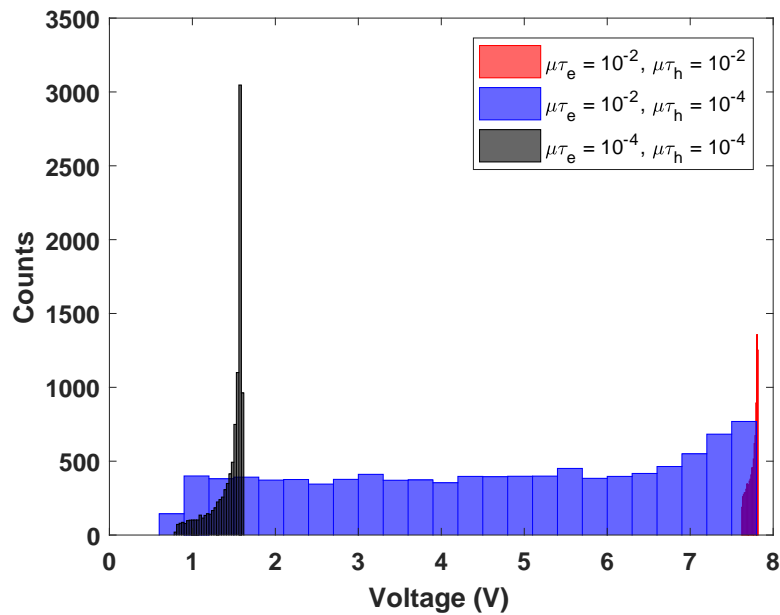
Figure 2.6: Pulse height spectra for combinations of electron and hole transport properties.

15

fraction of the radiation detection market for good reason. Due to direct charge readout and the low conversion losses, these detectors can offer faster response times and greater energy resolution, but the number of materials with adequate properties are limited. The pool of detectors suitable for neutron detection for additional reasons explained in Chapter 3 providing the motivation for the investigation of novel, promising materials.

Chapter 3

Neutron Detection and Radiography

3.1 Overview

This chapter focuses on the principles of neutron detection and radiography. The current state-of-the-art of the field is discussed with special emphasis on the semiconductor detection materials. First, the fundamental aspects of neutron interactions with matter are described to provide context to the intricacies of building a detector to exploit those properties. The fundamental limitations of current semiconductor detectors are discussed as they relate to the application space of lithium indium diselenide.

3.2 Principles of Neutron Detection

3.2.1 Interactions with Matter

Radiation detection is predicated on the transfer of kinetic energy from the incident radiation to the detection material, where the energy deposited is proportional to the detector response. Among the four types of radiation, heavy charged particles (HCPs), electrons (β), photons (X-rays and $\gamma's$), and neutrons, only the latter interact exclusively with the nucleus. As charged particles, HCPs and electrons interact heavily with the electron cloud via Coulombic interactions, while uncharged X-rays and gamma rays interact with the nucleus and the electron cloud through a variety of processes. Neutrons, however, must be detected indirectly

through the products of their interactions, which are comprised mostly of scattering or capture reactions depending on neutron energy. All interaction types are governed by the probability of the interaction occurring as it traverses a specific material. The cross section, σ, expressed in units of area, is a material and energy-dependent property quantifying the probability of interaction in a given material. The conventional unit for cross section is the barn (10^{-28}m^2), which is calculated on a per nuclei basis. The macroscopic cross section, Σ, is the product of the cross section, σ, and the nuclear density in the material yielding a probability of interaction per unit length traversed within the material. Each interaction type has its own probability and associated cross section [26, 35, 36]. The details of these interactions are more thoroughly discussed in Sections 3.3 and 3.4 according to their importance in the detection process over specific energy ranges.

Neutron Energy

For the purposes of this work, neutrons are divided into two energy categories: thermal and fast. In many applications, these major divisions are further reduced to subdivisions such as cold and epithermal. Thermal, or slow, neutrons are typically called such because their kinetic energy is in thermal equilibrium with their surroundings. At room temperature, a true thermal neutron has an energy of 0.025eV ($E = kT$). In this case, thermal neutrons are defined as those with a kinetic energy below the cadmium cutoff of 0.5eV. The cadmium cutoff is the energy where the immense neutron capture cross section falls off abruptly. Compared to thermal neutrons, fast neutrons are significantly more difficult to detect since the probability of interaction is inversely proportional to neutron energy.

Applications

A wide range of applications exist for neutron detection including reactor instrumentation, particle physics, space exploration, special nuclear material accountability, and materials science. The properties that make neutron detection difficult are precisely the same properties that make them useful. Low interaction probabilities mean that they can pass through very dense materials without interacting with the material, which is particularly

useful for imaging the internal structures of materials that are opaque to conventional X-ray and gamma imaging techniques. Neutron radiography is discussed more thoroughly in Section 3.5. Other nuclear security applications include materials identification using fast neutrons with systems such as the Fieldable Nuclear Material Identification System (FNMIS) [37, 38]. The fundamental physics community use neutron detection to answer questions about the fundamental structure and decay of nuclei with systems like the Versatile Array of Neutron Detectors at Low Energy (VANDLE) [39].

3.3   Thermal Neutron Semiconductor Detectors

Thermal neutron detection has been a key area of research in recent years for its applications in neutron science and imaging. Since neutrons are charge neutral, a material is required to convert them to charged particles or gammas via a capture process, which can then be detected. The products of thermal neutron capture reactions deposit their kinetic energy into the bulk of the material as they slow down via Coulombic scattering [40]. The combined kinetic energy of these capture reactions, known as the Q value, is the excess energy of the unstable capture nucleus when it decays into the reaction products [41]. For instance, the helium-3 thermal neutron capture reaction, a widely used neutron detection material, is:

$$^{3}_{2}\text{He} + ^{1}_{0}\text{n} \rightarrow ^{3}_{1}\text{H} + ^{1}_{1}\text{p} \underset{0.764\text{MeV}}{Q-value}$$
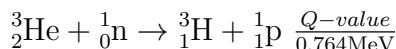
In this reaction, the 0.764 MeV released is divided among the triton ($^{3}_{1}\text{H}$) and proton ($^{1}_{1}\text{p}$) with 0.191 MeV and 0.573 MeV, respectively. The division of energy is governed by conservation of momentum such that the lighter product receives the most kinetic energy [26]. Large Q-value reactions are desirable in neutron detection due to the larger signal produced within the detection material. This section is dedicated to the various detection materials and devices used in low-energy neutron detection with special focus on semiconductor materials.

3.3.1   Neutron Capture

There are several isotopes that are generally useful for detecting thermal neutrons. Helium-3 is currently the gold standard due to a variety of factors including its high capture cross

section of 5333 barns [16]. However, in recent years, the threat of a shortage of ^{3}He has driven the development of new thermal neutron detectors. Additionally, as a gaseous detector, ^{3}He has its limitations in volumetric efficiency. Several other isotopes have large thermal neutron capture cross sections as well, including ^{6}Li (940 barns), ^{10}B (3837 barns), ^{113}Cd (20600 barns), ^{155,157}Gd (60900, 254000 barns), ^{235}U (583 barns), and ^{239}Pu (748 barns). Cadmium and gadolinium have exceedingly large capture cross sections, but their high Z values make them sensitive to gamma rays complicating neutron-gamma radiation discrimination. Furthermore, uranium and plutonium boast substantial Q-values (201 and 160 MeV, respectively) representing an immense amount of energy carried by the reaction products [16].

The lighter isotopes ^{6}Li and ^{10}B have much smaller Q-values in the 2-5 MeV range. The thermal neutron capture reactions for both isotopes are commonly referred to as neutron to alpha conversion reactions and can be visualized in Figure 3.1 [40]. While this nomenclature persists, any of the heavy charged particles generated in the neutron capture are important to detection. Due to their low Z-values and reasonably sized Q-values, they are inherently excellent candidates for applications that require neutron-gamma discrimination. While ^{10}B has a thermal neutron capture cross section that is nearly four times larger than ^{6}Li and is more chemically stable, ^{6}Li boasts a Q-value that is more than double that of boron-10. Furthermore, the reaction products for the ^{6}Li$(n,\alpha)^3$H reaction have larger ranges due to their higher energies, which is important when considering thin film conversion layer device configurations in addition to 3-D structures.

3.3.2 Device Architectures

Due to the inherent difficulty of detecting thermal neutrons, a number of device architectures and variations on those architectures have been explored. Intuitively, one of the most common solutions for incorporation of these neutron reactive isotopes is accomplished through thin film deposition onto current technologies. While this method capitalizes on previous technologies and a simplistic implementation method, certain limitations relating to the geometry and range of the reaction products require more complex device structures including micro-structures and 3-D configurations. Furthermore, pure lithium metal is highly
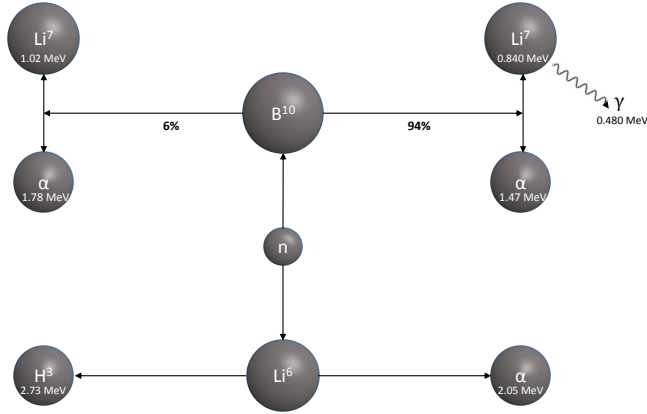
Figure 3.1: Notional diagram of neutron to alpha conversion reactions in ^{6}Li and ^{10}B with the reaction products [40].

reactive and poses a formidable obstacle in implementation as a neutron sensitive film. A more stable compound like ^{6}LiF is used to mitigate the issues, but not without drawbacks. The addition of a higher Z material like fluorine reduces the range of the reaction products limiting the thickness and efficiency of neutron reactive films [26]. In contrast, compound semiconductors are currently under development that incorporate ^{6}Li as a component in the crystalline lattice of the semiconductor. Among these lithium containing chalcogenides such as lithium indium diselenide (^{6}LiInSe$_2$), demonstrate promise as viable options for thermal neutron detection [42]. Semiconductors that contain a neutron reactive material like ^{6}Li offer the benefit of capturing thermal neutrons throughout the bulk of the semiconductor.

3.3.3   Thin Film Coated Semiconductors

The general design of thin film coated semiconductor is illustrated in Figure 3.2. An incident neutron is captured by the neutron reactive film generating two reaction products. To conserve momentum, the two particles travel in opposite directions. One of these particles must then travel through a dead layer into the active area of the semiconductor detector where the generated charge carriers can be collected [40]. Now, there are some important considerations that should be addressed. First, recognize that only one of the two particles reaches the active volume of the detector.
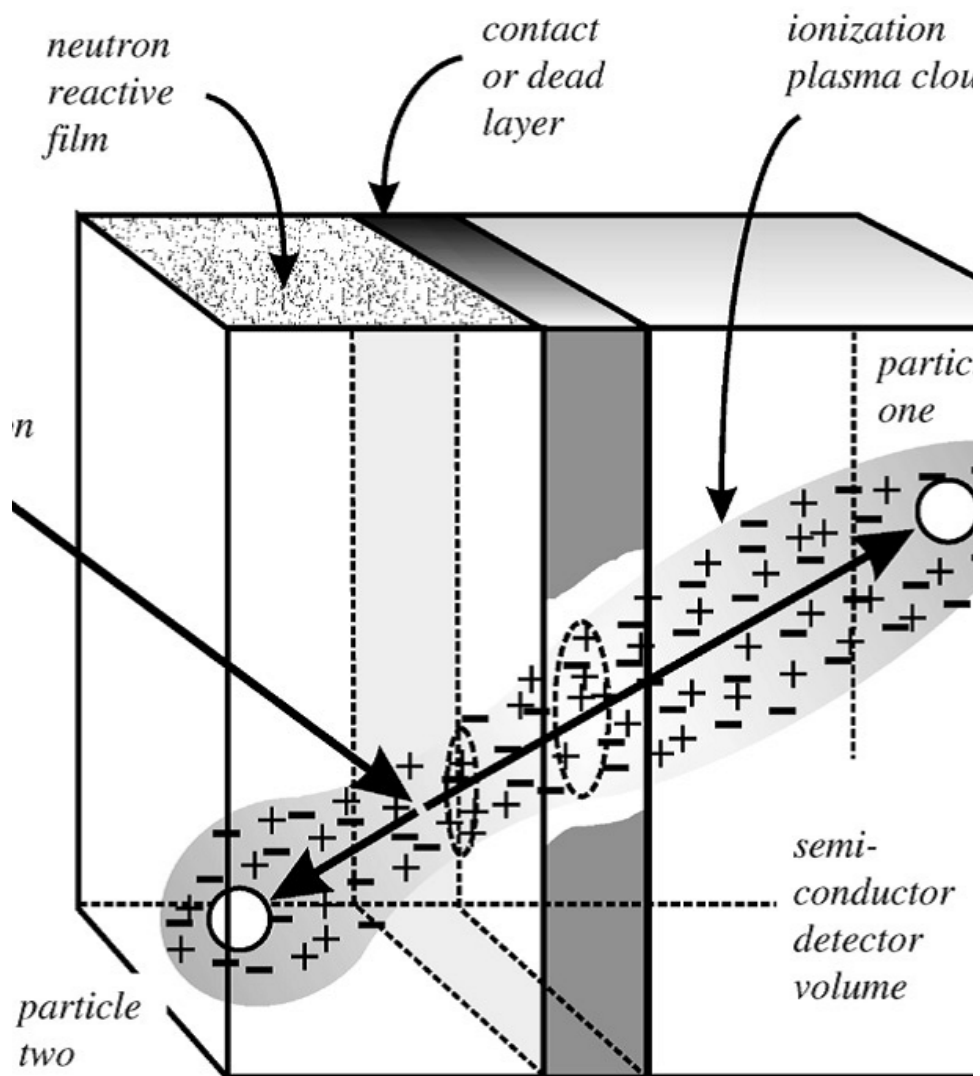
Figure 3.2: General design principle of thin film coated semiconductor thermal neutron detector architecture. The incident neutron is captured and the reaction products are emitted in opposite directions. Charge carriers are created in the active volume of the detector as the reaction products undergo Coulombic scatting [43].

Since the reaction products have a limited range in the film and the semiconductor, it follows that the thickness of the film should not exceed the distance traveled by the particle with the longest range. Otherwise, neutrons captured on the front face of the film will lose all of their energy before reaching the active detector volume. Since the highest capture probability is on the incident face of the detector, additional thickness only degrades the efficiency. Even so, capture reactions that occur near the front-face of the detector and emit the shorter range particle towards the semiconductor are undetectable. Since the reaction products can be emitted at any angle respective to the plane of the detector, many neutron captures go undetected as the reaction products never reach the semiconductor bulk. Therefore, the probability (p) of one of the reaction products (subscript p) entering the semiconductor is a function the capture position, x, and is described by the equation,

$$p_p(x) = \frac{\Omega(x)}{4\pi} = \frac{2\pi}{4\pi}(1 - \frac{x}{L}) = \frac{1}{2}(1 - \frac{x}{L}), x \leq L \tag{3.1}$$

where $\Omega(x)$ is the solid angle subtended by the detector and L is the average effective range of the reaction products [40].

McGregor analyzed the effective range (L) of the reaction products within the film for ^{10}B, ^{6}Li, and ^{6}LiF films. Additionally, he used the product ΣL to compare the relative detection efficiency of each of the films where Σ is the macroscopic thermal neutron capture cross section. This relation combines the effects of capture probability with the range of the reaction products to give a general sense of the detection sensitivity of the film. For a given lower level discriminator (LLD) of 300 keV, the range and L values are given in Table 3.1. The LLD represents the minimum detectable energy that reaches the active volume of the detector. This data demonstrate that ^{6}LiF is comparable to ^{10}B in terms of ΣL, but both are outperformed by the pure lithium coating. Furthermore, for a front side irradiation, the ^{10}B, ^{6}LiF, and ^{6}Li have maximum thermal neutron detection efficiency of 4%, 4.5%, 11.5% at 2.4, 26, and 100 μm thick, respectively [40].

Various methods have been employed to enhance the thermal neutron detection efficiency for this class of detectors. When a neutron beam is incident on the detector, the rate of reaction is highest where the beam enters the reactive film. Backside irradiation yields a

Table 3.1: Thermal neutron capture products and ranges for various conversion materials.

FILM	PRODUCT	ENERGY (MeV)	RANGE (μm)	ΣL
^{10}B ($\Sigma = 500\,\mathrm{cm^{-1}}$)	α	1.777	3.5233	0.1762
	α	1.470	2.6475	0.1324
	^{7}Li	1.015	1.0453	0.0523
	^{7}Li	0.840	0.8102	0.0405
^{6}Li ($\Sigma = 43.6\,\mathrm{cm^{-1}}$)	t	2.730	126.77	0.5522
	α	2.050	19.055	0.0830
^{6}LiF ($\Sigma = 57.5\,\mathrm{cm^{-1}}$)	t	2.730	29.239	0.1682
	α	2.050	4.5454	0.0287

slightly higher efficiency by allowing the beam to enter the reactive film at the film-detector junction. However, the detector must be insensitive to neutrons in order to preserve the incident neutron beam. For a given film thickness, the efficiency can be increased by changing the angle of incidence creating a longer path for the neutron beam to pass through the film. Consequently, there is a decrease in the area subtended by the beam on the detector, which decreases the sensitivity. Therefore, tilting is only advantageous for the case in which the detector is larger than the incident beam [40].

Unruh et al. demonstrated the viability of a ^{6}LiF coated silicon detector for use in beam port monitoring. This 5 x 5 pixelated sensor ($0.25\,cm^2$) was fabricated from 400 μm thick n-type Si wafers ($\rho > 10\,\mathrm{k\Omega - cm}$). The reactive film coating was deposited via physical vapor deposition to a thickness of 1 μm, which corresponds to a thermal neutron detection efficiency of 0.5%. With appropriate scaling factors, the 5 x 5 array recorded counts in a $2 \times 10^4\,\mathrm{n\,cm^{-2}s^{-1}}$ flux to within 2% deviations [44].

Furthermore, the advantages of using a ^{6}Li based converter layer were shown by Jakubek et al. at CERN when applied to the Medipix-2 device. Medipix-2, a hybrid silicon pixel detector with a 256 x 256 array of 55 μm pixels, was developed as an X-ray photon detector, but can be used for neutron imaging when a reactive film is applied. In this case, the silicon substrate was coated in powdered ^{6}LiF suspended in a glue through an aerosol spray. Once the glue evaporates, the film is approximately 95% ^{6}LiF ($3\,\mathrm{mg/cm^2}$) and has a thermal neutron detection efficiency of 3%. Using a Cd plate, the spatial resolution of the configuration was quantified using the full-width half maximum of the line spread function.

In addition to ^{6}LiF,^{10}B, Cd, and Gd were also tested as a neutron conversion layer. The ^{10}B conversion layer demonstrated the best spatial resolution of 50 μm while the ^{6}LiF converter had a spatial resolution of 100 μm. However, the ^{6}LiF converter showed a higher detection efficiency of 3%, which was twice the efficiency of ^{10}B. The remaining converters performed poorly. Moreover, the ^{6}LiF and ^{10}B conversion film on the Medipix-2 device outperformed both the ^{6}Li-doped scintillation screen/CCD and imaging plate used at the Paul Scherer Institut (PSI) in spatial resolution as illustrated in Figure 3.3 [43].

3.3.4 Microstructure Devices

Due to the limited geometrical efficiency of thin film coated detector designs, significant effort has been focused on developing more complex 3-D configurations that incorporate ^{6}Li into the bulk of the semiconductor. Uher (2006) developed a 3-D Si thermal neutron detector by etching $62\,\mu$m deep and $50\,\mu$m pitch pores into a 25 mm^2 sample of Si ($\rho = 5\,\mathrm{k\Omega - cm}$) and filling them with 89% enriched ^{6}LiF (Figure 3.4). The resultant pulse height spectrum shows counts above the 2.73 MeV energy of the tritons from the ^{6}Li$(n, \alpha)^3$H reaction, indicating that the energy of both reaction products has been collected. However, the gain in full charge collection of both reaction is counteracted by the reduced surface area available for reaction [45]. Uher (2007) expanded on this work to characterize the detection efficiency of this 3-D configuration via simulation and experimentation. Their results showed that the predicted 33% thermal neutron efficiency was valid for 3-D detectors. Additionally, they determined that a detector of this type demonstrated nearly 100% charge collection efficiency down to a pillar size of 30 μm [46].

Shultis and McGregor (2004) simulated various device configurations to compare the efficiency of a perforated and a trench based design. They sought to identify the optimum, feasible micro-structure architecture via Monte Carlo simulation. Their model consisted of a Si p-v-n junction diode detector with deep (300 μm), columnar holes etched into the pn junction side of the detector for the perforated design or a series of parallel trenches for the trench design. These cavities were back filled with ^{6}LiF or ^{10}B nanoparticles. The simulations demonstrated that ^{6}LiF coated semiconductors generally produced higher detection efficiency due to the longer ranges of its reaction products. The perforated design results indicated
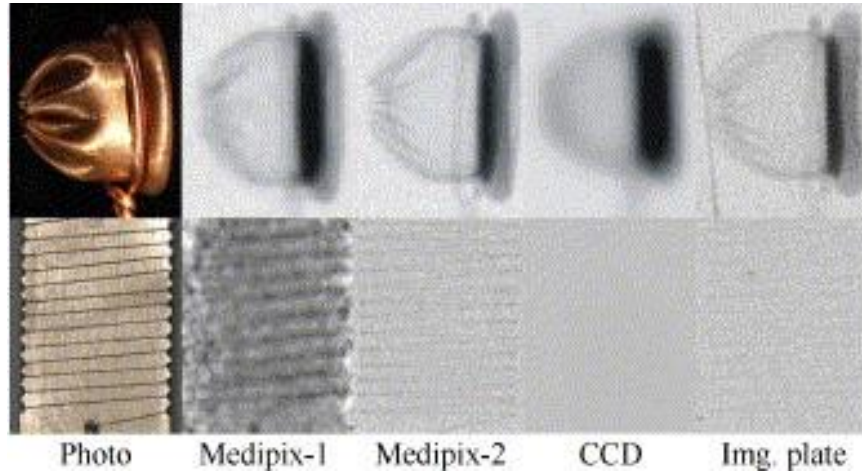
Figure 3.3: Comparison of thermal neutron images from different devices.
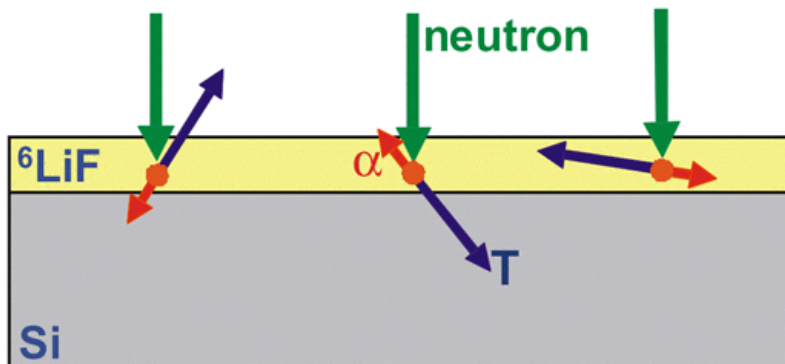
Figure 3.4: Illustration of the design principles of the 3-D neutron detector. Incident neutrons that travel through the ^{6}LiF reactive material are captured and emit their reaction products in opposite directions, which deposit their energy into the bulk of the Si substrate [45].

26

that efficiencies greater than 20% can be achieved when limiting their data to feasible feature sizes. Dry etching can produce a perforated sample with 30 μm holes. Additionally, it should be noted that the efficiency can be maximized using a 20 μm thick cap layer (^{6}LiF) on the surface of the detector. Similarly, it was shown that the parallel trench design is capable of reaching thermal neutron detection efficiencies of 30% or greater within the practical limits of detector fabrication [47].

As micro-structure designs have evolved, they become exceedingly complex as is the case with the sinusoidal device configuration reported by McGregor et al. (See Figure 3.5). For a 100 μm deep structure yielded an average efficiency of 11.94   0.078%, which is less than the predicted 13.65%. This is attributable to the difference in packing fraction of the ^{6}LiF nanoparticles between simulation and experiment. Furthermore, as the width of the trenches is decreased from the 25 μm reported above to 12.5 μm, the efficiency increases to approximately 25% [47].

To further increase detection efficiency, detector stacking can be employed as reported by Bellinger et al. A 10 $k\Omega - cm$ n-type Si wafer was prepared via a 45% KOH wet-etching process to produce trenches 250 μm deep and 25 μm wide with a pitch of 50 μm. The trenches were then back-filled with nanoparticle ^{6}LiF powder via mechanical pressing. Using Silvaco, it was demonstrated that the full charge integration time is approximately 10 μs. Figure 3.6 demonstrates the neutron and gamma ray response of the Micro-structure Semiconductor Neutron Detectors (MNSD). Using a He-3 tube as a calibration device, the thermal neutron detection efficiency was determined to be 42%, which is a marked increase over previous designs. Additionally, the MNSD demonstrates high gamma ray rejection (Figure 3.6) [48].

Overall, the limited thermal neutron detection efficiency of planar thin-film coated thermal neutron detectors can be increased by creating 3-D device structures. These structures not only increase the total thermal neutron reactive volume, but also increase the probability of the capture reaction products reaching the active volume of the detector volume. As evidenced by the works presented, ^{6}LiF is a popular thermal neutron reactive material for these micro-structure devices due to the high Q-value of the ^{6}Li$(n, \alpha)^3$H reaction, the long range of the alpha and triton reaction products, and the chemical stability of the ^{6}Li over the pure ^{6}LiF.
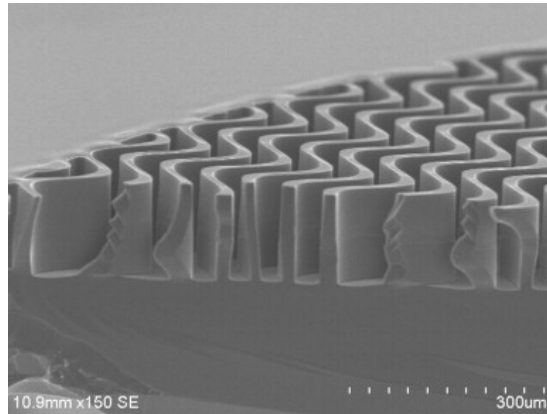
Figure 3.5: Magnified image of the sinusoidal micro-structure Si detector prior to backfilling with ^{6}LiF. The sinusoidal shape is achieved using inductively-coupled plasma reactive ion etching (ICP-RIE) [47].
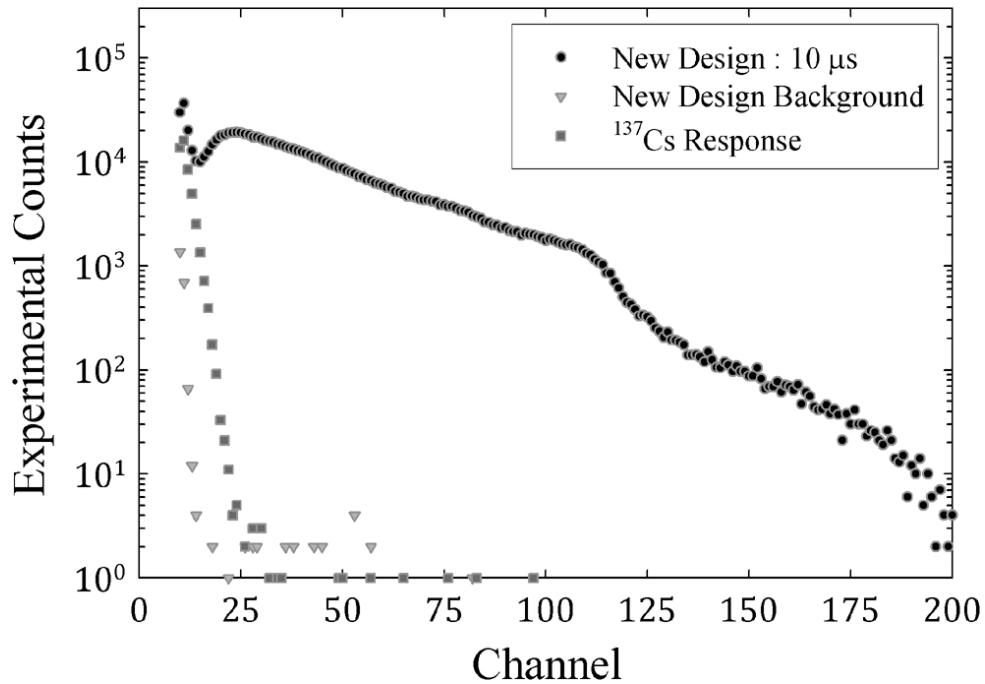
Figure 3.6: Measured neutron and Cs-137 gamma ray pulse height spectrum for the stacked MNSD with 250 um deep trenches and 10 us charge integration time [48].

3.3.5 Summary

Thermal neutron detection presents a unique challenge requiring development of novel detection mechanisms. Some developments have their roots in modification of existing semiconductor technologies while others probe the viability of a new class of semiconductors. In order to detect a neutral particle like a neutron, a converter material is required to transfer the neutron energy to reaction products like heavy charged particles through a capture process. Among these candidate materials, ^{6}Li and ^{10}B are most promising due to their low Z value and high Q value making pulse height rejection of gamma rays possible. ^{6}Li is often used due the longer range of the alpha and triton reaction products. The stable compound ^{6}LiF has become the reactive material of choice for many applications due to its ease of implementation compared to pure, corrosive ^{6}Li in both thin film coated and micro-structure devices.

Thin film devices can reach neutron efficiencies of approximately 3%, but are limited by the loss of one or both of the heavy charged particles. To mitigate this, 3-D micro-structure devices employ perforations or trenches etched into the bulk semiconductor filled with ^{6}LiF nanoparticles to enhance the probability of collection of both reaction products reaching thermal neutron detection efficiencies greater than 30%. Furthermore, a stacked device configuration can push the thermal neutron detection efficiency over 40%.

Ideally, a high concentration of ^{6}Li in the bulk of a semiconductor ensures a majority of the Q-value energy from both reaction products will be deposited within the active volume of the semiconductor. Lithium containing chalcogenide, ^{6}LiInSe$_2$, seeks to fill that void with promising properties such as gamma ray rejection. Due to the inherently large content of ^{6}Li in the composition, approximately 80% of the incident thermal neutrons are captured by ^{6}Li at a reasonable thickness of 0.5 mm. While the efficiency of the lithium indium diselenide exceeds that of the coated and perforated devices, the charge carrier properties are noticeably inferior to well-developed materials like Si. Recent developments in this area provide encouraging results for devices that serve as both a complement to the widely-used ^{3}He detector and novel solutions to unique challenges.

3.4 Fast Neutron Detection

Thermal neutron detection, while more difficult than alpha, beta, X-ray, and gamma detection, is feasible using the various thermal neutron capture reactions described in section 3.3. These reactions have relatively large cross sections and deposit large amounts of energy into the bulk of the detection material. Conversely, fast neutron capture reactions have much smaller cross sections. For neutron counting, fast neutrons may be converted to heavy charged particles in the same manner as described previously by first thermalizing the neutrons. Thermalization is the process of slowing neutrons down via scattering collisions in a hydrogenous material. A single elastic scattering collision with a proton can completely thermalize a fast neutron, regardless of energy. These scattering cross sections are much larger than the fast neutron capture reactions. However, the initial energy of the fast neutron cannot be derived since the number of collisions is unknown. Using a series of moderator thicknesses, an approximate spectrum can be derived using unfolding techniques, but with significant uncertainties [26].

Fast neutron spectroscopy is typically performed using detectors that rely on capture and/or scattering reactions rather than thermalization. Among the capture reactions, the $^3\mathrm{He}(n, p)$ and $^6\mathrm{Li}(n, \alpha)$ are most commonly used due to their large cross sections compared to other materials. For energies between 4 and 10 MeV, the $^6\mathrm{Li}$ capture reaction has a fairly uniform cross section of 1 barn, as shown in Figure 3.7. Detectors that fall under this category include helium proportional counters, ionionization chambers and scintillators as well as lithium based scintillators. Scattering based detector designs rely on the detection of the recoil nuclear (typically protons). Proton recoil detectors include scintillators containing hydrogen, gas proportional counters, and proton recoil telescopes [26].

The primary factors affecting performance are similar to those affecting thermal neutron detection - efficiency and detector size limitations. Fehrenbacher et.al (1997) studied the performance of a $^6\mathrm{LiF}$ converter layer on Si in a 5 MeV neutron field. Of note, it was shown that a coated detector can be used in a higher energy field due to the thermalization of back-scattered neutrons as well as direct capture reactions. The pulse height spectrum also shows counts beyond the 5 MeV neutron energy. This is attributed to both reaction products
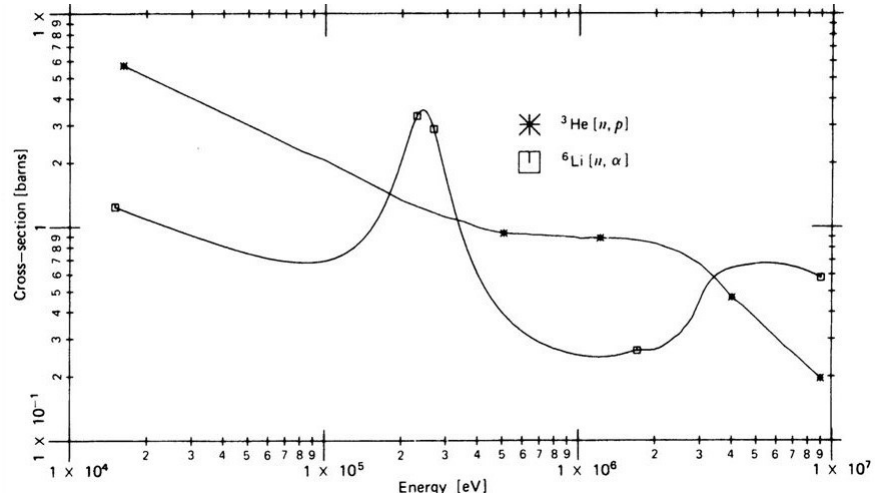
Figure 3.7: Fast neutron capture cross sections for ^{3}He(n, p) and ^{6}Li(n, α).

reaching the active detector volume, which occurs, when the energy of the neutron is high enough such that the reaction products move in the same direction as the incident neutron [49]. As such, conversion layers configurations with both semiconductors and scintillators are still important in fast neutron detection. Other detectors commonly used in fast neutron detection include liquid organic scintillators in large volume applications, boron doped plastic scintillators, and $CLYC$, which all have issues with gamma sensitivity [50].

3.5 Radiography

Neutron radiography and tomography have evolved as a powerful non-destructive technique to probe the structure of matter. As a complementary analog to X-ray interrogation, neutron imaging is useful for visualizing both static and dynamic systems containing hydrogenous and/or other low-Z materials that are not efficiently interrogated via X-ray imaging. Applications of these techniques have evolved to include organic and biological systems and fuel cells [41, 51]. Additionally, fast neutron imaging has additional applications in extremely dense materials impervious to other imaging techniques with significant interest in nuclear security applications [52–54].

3.5.1 Design Principles

A radiography system is typically comprised of an interrogation source, an imaging object, and a neutron detector, as shown in Figure 3.8. The technique is predicated on the ability to visualize interesting features in an imaging object based on the attenuation of the neutron beam. Attenuation is the reduction in the impinging beam via interactions with the object between the detector and the beam source.

This reduction in beam intensity from the source I_0 to the detector I is given by the relation

$$I = I_0 \exp(-\Sigma t) \tag{3.2}$$

where Σ is the macroscopic cross section and t is the thickness of the material and the beam intensity are expressed in units of flux $(n/cm^2 - s)$. From Equation 3.2, it is clear that, with sufficient neutron flux, small differences in material composition or structures can be identified based on the local attenuation of the beam.

Radiography typically employs scintillating screens optically coupled to a charge-coupled camera or a pixelated semiconductor detector to provide positive sensitive neutron intensity information. From this information, a radiograph, like the one shown in Figure 3.9, can be generated to provide a useful depiction of otherwise invisible structures.
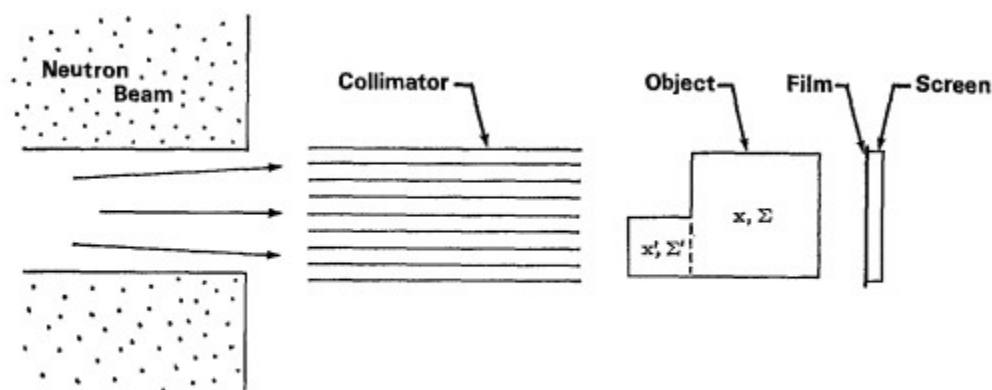
Figure 3.8: Notional diagram of a neutron radiography system [55].

plastic lens mounts→

plastic lens mounts→

plastic insulators
in ionisation
chamber   →

←glass lens

←metal clip

←glass lens

central
←metal
conductor
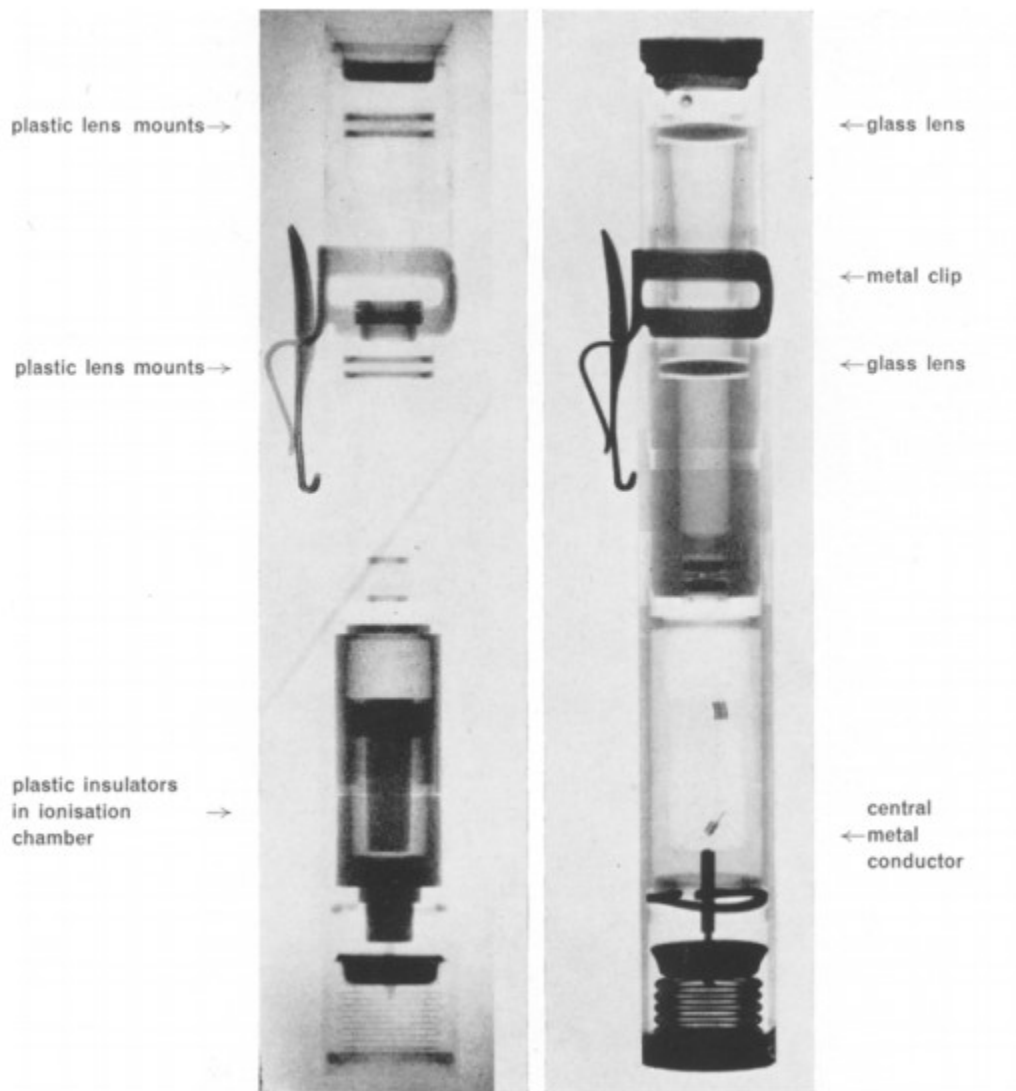
Figure 3.9: Comparison of neutron (left) and X-ray (right) radiographs of a pocket dosimeter illustrating the complementary capabilities of each technique. The plastic (highly hydrogenous) materials are clearly present in the neutron radiograph, whereas, the glass and metal components are more defined in the X-ray image [55]

.

3.5.2 Detector Considerations

As the application diversifies, the need for higher neutron detection efficiency, spatial resolution, and temporal resolution has grown. Detection efficiency dictates the acquisition time for a given imaging object and beam intensity. Larger efficiency allows for shorter integration times for the same level of contrast. The spatial resolution is a quantity that defines the finest structures the imaging system can resolve. Spatial resolutions of $< 10\,\mu\mathrm{m}$ have been achieved for thermal neutron radiography using enriched ^{157}Gd conversion screens, but is not an easily scalable solution due to cost and scarcity [56]. For fast neutron radiography, spatial resolution on the order of mm is desirable and has been achieved using zinc sulphide scintillation screens, However, ZnS screens are limited in detection efficiency due to the thickness limitations [57]. Many factors influence the spatial resolution including the range of the reaction products within the detector to pixel size. Additionally, spatial resolution and integration time can be inversely proportional for scintillation screens due to internal light spreading effects.

3.6 Summary

Significant research has been devoted to the development of new imaging detectors with increased efficiency and resolution to meet the needs of the nuclear security and safeguard community to provide faster, more reliable safeguards inspection systems. The inherent difficulties in thermal neutron detection have necessitated the continued investigation of novel detection materials and device configurations to meet these demands. While a significant fraction of the field is dedicated to the use of ^{6}Li as a conversion material, there are few materials that incorporate the neutron sensitive isotope within the bulk of the material so detection efficiencies are limited by the range of the secondary particles. This work focuses on the characterization and development of a novel semiconducting material, ^{6}LiInSe$_2$, to determine if its semiconducting properties are sufficient to meet the growing demands of the neutron detection and imaging field.

Chapter 4

Lithium Indium Diselenide

The limitations of thin film and micro-structure thermal neutron detectors center on the energy loss of the reaction products before reaching the active volume of the detector. Including ^{6}Li in the bulk of the semiconductor can vastly increase the thermal neutron detection efficiency. Recently, research has been focused on developing lithium containing chalcogenide crystals including $LiInSe_2$, $LiGaSe_2$, $LiInTe_2$, and $LiGaTe_2$. One of the most promising of this new class of semiconductors is lithium indium diselenide ($^6LiInSe_2$), which was first investigated in 1973 for its use in nonlinear optics [58]. Lithium indium diselenide, or LISe for short, was first investigated as a neutron detector in 2005 by Bell et al. [59]. From this, a collaboration between Y-12 National Complex, Fisk University in Nashville, TN, and Oak Ridge National Laboratory began developing the material for a variety of compact detector applications resulting in a Research and Development 100 Award.

4.1   Growth

Various growth techniques have been implemented to reliably produce single crystal LISe including horizontal and vertical Bridgman techniques [60, 61], gradient freeze technique [58], and directional solidification [62]. For this research, the vertical Bridgman technique was implemented at Fisk University as described by Tupitsyn et al. [60]. Synthesis begins with the metal alloy LiIn in a 1:1 molar ratio with high purity. The precursor Li was enriched to 95% ^{6}Li through a vacuum distillation process developed and implemented at CNS Y-12

National Laboratory [63]. The alloy is placed in a pyrolytic boron nitride crucible under 300 Torr of argon pressure and heated in a Se atmosphere to 940°C.

The single crystalline material grown via the vertical Bridgman method was produced at a growth rate of 5-10 mm/day [42]. LiInSe$_2$ can have exhibit several different different colors depending on growth parameters, where the predominant variants being yellow and red, as shown in Figure 4.1a. Further delineations of color include dark red and greenish-yellow. The color of the material provides some indications of the quality of the crystal and it semiconducting properties as discussed in Section 4.2.2. Isaenko et al. noticed that as-grown yellow crystals revert to a dark red color upon annealing in a Se atmosphere [61].

4.2 Material Properties

4.2.1 Crystal Structure

As a single crystalline material, LISe possesses an orthorhombic symmetry with lattice parameters: $a = 7.162$, $b = 8.543$, and $c = 6.769$ Å for a crystal grown via the vertical Bridgman-Stockbarger method.[60]. Additional first principle studies and experimental

(a)   (b)
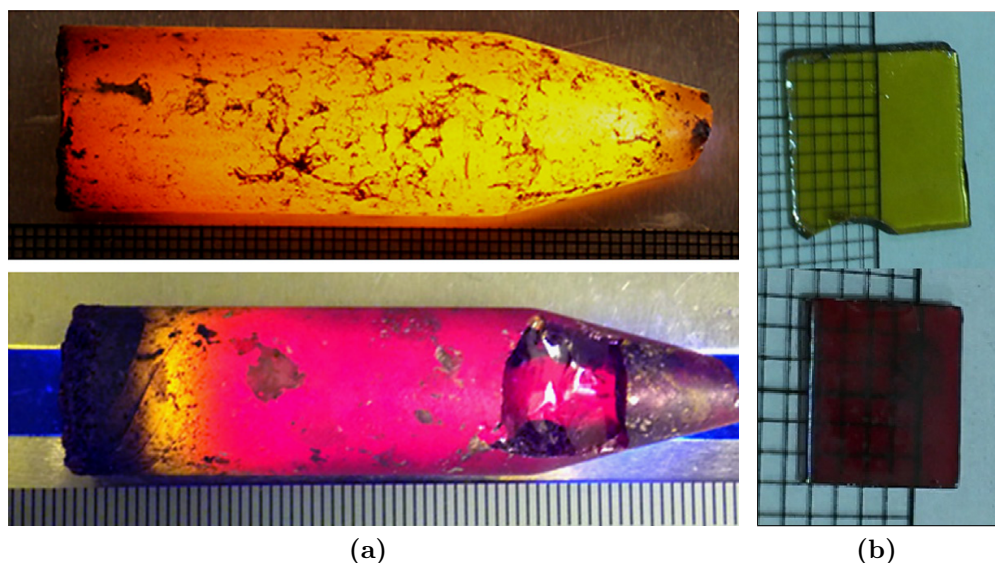
Figure 4.1: ^{6}LiInSe$_2$ crystal boules as grown via the vertical Bridgman method. The yellow color predicts improved semiconductor properties compared to the red color [42].

measurements have produced similar lattice parameters for this material [61, 64–73]. LISe, as a ternary chalcopyrite, exhibits a wurtzite-derived βNaFeO$_2$ structure belonging to the Pn$_2$a$_1$ space group [74]. Figure 4.2 depicts the ternary βNaFeO$_2$ and binary wurtzite structures [75].

4.2.2   Crystal Color and Defects

The aforementioned color disparity, as shown in Figure 4.1b, observed in LiInSe$_2$ provides a visual indication of crystal quality due to a strong correlation in electronic properties despite consistent crystal structure. Color-related effects have been analyzed via experimental and theoretical studies to understand the differences in electrical, optical, and vibrational properties of LISe with varied, and sometimes conflicting, results. Weise et al. noted that the deep red color was indicative of a Li deficient secondary phase LiIn$_5$Se$_8$ [76]. The lighter red color, sometimes coexisting with the yellow color within a singular boule, is a solid solution enriched in In$_2$Se$_2$ precipitates that form within the crystal creating a micro-heterogeneity too small to be detected by conventional methods. Vasilyeva et al. demonstrated this unique property through differential dissolution concluding that very small deviations from stoichiometry within the melt during growth leads to an unstable LiInSe$_2$ − In$_2$Se$_3$ system [77]. These precipitates act as scattering centers severely impacting its optical and electronic properties. The In$_2$Se$_3$ phase has a much smaller band gap (≈ 1.2 eV) compared to LiInSe$_2$ (≈ 2.8 eV) creating a significant deflection of the energy bands and consequent charge loss.

Reddish crystal color has been attributed to point defects arising from Li deficiencies by Isaenko et al.[78]. Conversely, Badikov et al. attributes the yellowish color to an abundance of scattering centers [79]. Vijayakumar et al. similarly attributed the coloration to Li vacancies (V$_{Li}$), Se interstitials, and In$_{Li}$ antisite defects [69]. Ma et al. demonstrated that red crystals suffered from a Se deficiency via the stoichemetric ratio Se/(Li$^+$In) [80]. Laser-Induced Breakdown Spectroscopy measurements, an optical emission spectroscopy technique used to identify atomic constituents by the light emitted from a laser-generated plasma, performed by Wiggins et al. identified the reddish color as Li rich compared to yellow crystals. Impurity atoms of Na, Ca, and K were also identified within this material that tend to concentrate in reddish portions of an analyzed sample. These impurities are an expected contaminate
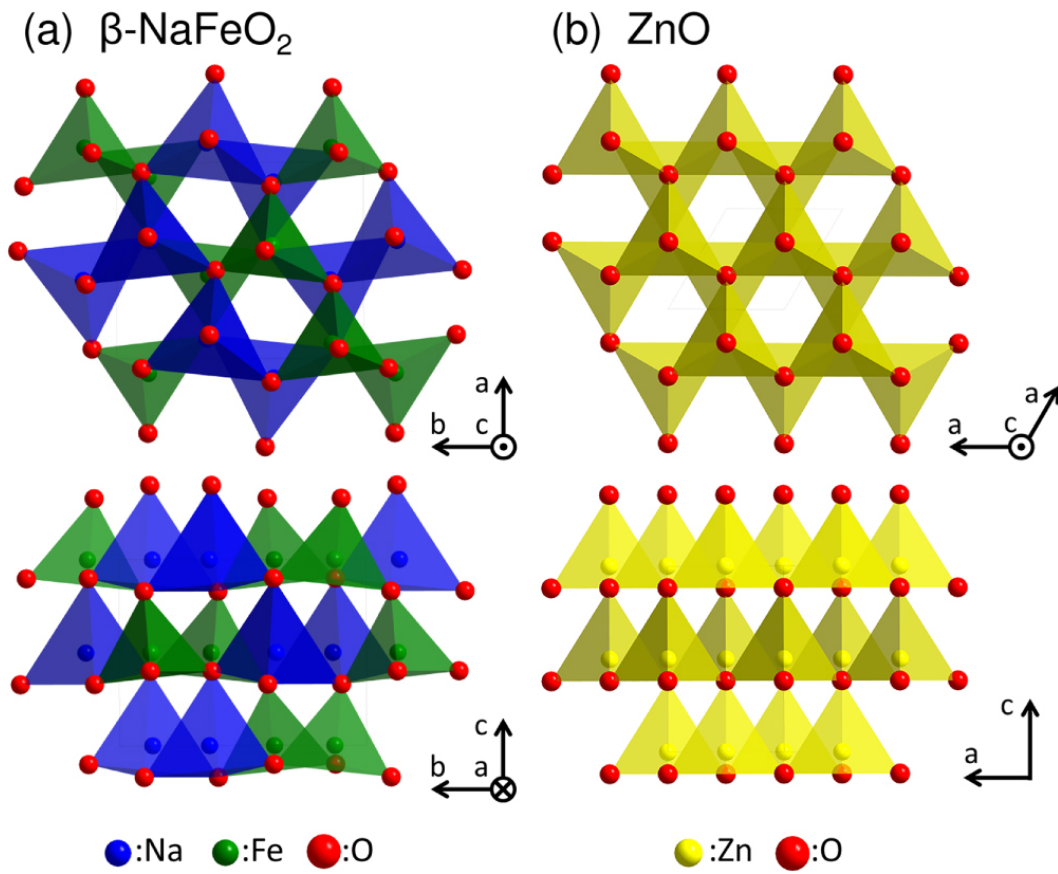
Figure 4.2: βNaFeO$_2$ (left) and wurtzite (right) crystal structures. Substitutions of Li−Na, In−Fe, and Se−O give the structure of ternary I−III−IV$_2$ semiconductor LiInSe$_2$. [75].

from the ^{6}Li enrichment process. Clearly, there is no consensus on the source of the color distinction, but significant progress has been made in identifying the primary defects in LISe.

Photo-induced Current Transient Spectroscopy (PICTS), a technique further described in Section 5.3.2, performed by Cui et al. identified six intrinsic defects for the yellowish crystal. The charge carrier traps were categorized according to their location with respect to the valence band, E_V, and the conduction band, E_C, due to the single polarity nature of the PICTS measurement, as shown in Figure 4.3. Electron and hole trapping defects were observed at E_C - 0.22, 0.36, and 0.55 eV and E_V + 0.19, 0.30, and 0.73 eV, respectively. These defects were tentatively assigned to In and Se vacancies and various charge states of the In-Li antisites [67]. Similarly, Kamijoh et al. identified Se vacancies at E_C - 0.85 eV and Li vacancies at E_V + 0.89 eV for p-type LiInSe$_2$.

Tangentially, Li et al. used Density Functional Theory (DFT) to investigate the role of point defects and defect complexes on the color of the material. Through investigation of the defect formation energies in both a Li-sufficient and Li-deficient growth environment, this study concluded that point defects and defect complexes red shift the optical absorption cutoff. Furthermore, the doubly-charged antisite defect In_{Li}^{2+} and the associated defect complex In_{Li}^{2+} + $2V_{Li}^{-}$ red shift the absorption edge $0.7\,eV$ exhibiting close agreement with the energy difference between the red and yellow crystals [81]. In summary, the color differences in LISe are likely attributable to Li deficiencies leading to non-stiochiometric precipitates and defect complexes. Consequently, these defects play a significant role in the electronic properties and the performance of LiInSe$_2$ radiation detectors.

4.2.3 Electrical Properties

LISe is a wide band gap ($E_g > 2eV$) semiconductor making it an ideal candidate for room-temperature radiation detection. As discussed in Section 2.1.1, a large band gap reduces the leakage current of a detector allowing smaller signals to be detected at room-temperature. Additionally, LISe exhibits high resistivity ($\rho > 10\,G\Omega - cm$) allowing the detector to be operated in resistive mode (See Section 2.2.1) with ohmic contacts. Table 4.1 provides band gap energies (E_g), dielectric constants (ϵ), and resisitivities (ρ) for LISe determined through experimental and theoretical studies [60–62, 64, 67–69, 71, 72, 76, 82–85].
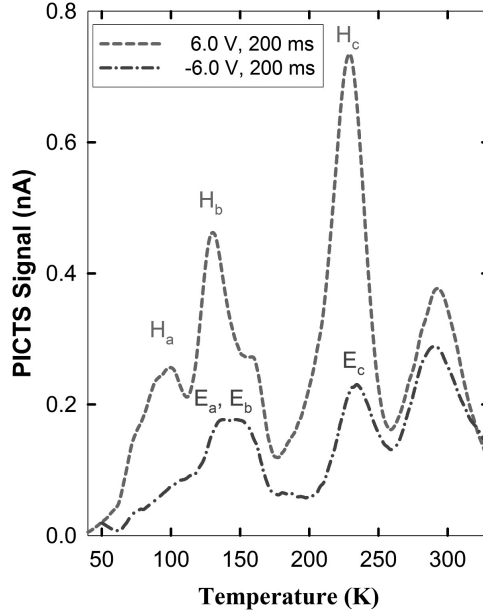
Figure 4.3: Photo-induced Current Transient Spectroscopy measurements of yellow LiInSe$_2$ demonstrating three electron and three hole-related defects [67].

Table 4.1: Band gap energy, dielectric constant (ϵ), and resistivity (ρ) for LiInSe$_2$ from various studies.

SOURCE	$E_g(eV)$	ϵ	$\rho(\Omega - cm)$	COLOR	METHOD
Kamijoh et al. (1981)	1.88	9.4	2.67×10^{11}	red	Experimental
Kamijoh et al. (1983)	2.06	8.1		red	Experimental
Beister et al. (1991)	2.03			red	Experimental
	2.90			yellow	Experimental
Weise et al. (1996)	2.85				Experimental
Eifler et al. (2000)	2.83			yellow	Experimental
Li et al. (2009)	2.35	6.02			DFT
Petrov et al. (2010)	2.86		3.00×10^{11}	yellow	Experimental
Li et al. (2011)	2.29	5.73			DFT
Tupitsyn et al. (2012)	2.85		6.50×10^{11}	yellow	Experimental
Cui et al. (2013)	2.03			red	Experimental
	2.85			yellow	Experimental
Vijayakumar et al. (2014)		9.8	3.43×10^{10}	yellow	Experimental
Ma et al. 2015	1.98			red	Experimental
	1.685	8.5			DFT
Wiggins2016	2.99			yellow	Experimental

The band gap is strongly correlated with the material with yellow crystals ($E_g \approx 2.8\,\text{eV}$) exhibiting band gap a 47% larger than red crystals ($E_g \approx 1.9\,\text{eV}$). While the band gap energy has been heavily studied due to interest from the infrared optics community, charge carrier transport properties have not received significant attention. Bell et al. investigated the charge carrier mobility product by observing spectral features from neutron exposure as a function of electric field. Using a variation of Equation 2.10, a combined electron-hole $\mu\tau$ of $3 \times 10^{-6}\,\text{cm}^2/\text{V}$ was calculated. The electron-hole pair ionization energy has yet to be determined outside of the work presented in Chapter 6.

4.3 Detection

Due to the high Q-value, as described in Section 2.1 of the ^{6}Li (n, α) ^{3}H reaction and the 100% energy deposition of the reaction products within the active volume of the detector [42]. When enriched to 95% ^{6}Li, the 25% atom fraction of lithium in the composition can reach a thermal neutron capture efficiency of 99% in a 5 mm thick sample, which more than doubles the efficiencies of the most complex micro-structure detector designs. However, it should be noted that ^{115}In content of the crystal contributes to the thermal neutron capture efficiency, which constitutes approximately 20% of the total capture efficiency. Therefore, the total ^{6}Li neutron capture efficiency is approximately 78% [86]. While ^{6}LiInSe$_2$ has some relatively high Z components, it has demonstrated to have a limited response to γ rays such that pulse height rejection is feasible in dual neutron γ fields [85].

4.3.1 Semiconductor Mode

LiInSe$_2$ has been shown to respond to α particles, cold neutrons, and a moderated Pu/Be neutron spectrum in semiconduction mode [42, 63, 86–90]. Figures 4.4a and 4.4b show typical α and neutron spectra for semiconducting LISe. The impact of charge transport properties are evident in these spectra. Poor hole transport with respect to electrons is evident from the broad response to thermal neutrons in Figure 4.4b and the absence of a peak in the α spectrum when collecting holes only. The 4.8 MeV capture reaction should result in a Gaussian distribution well separated from the noise floor. However, as shown

in Figure 2.6, significant hole trapping and low hole mobility result in a neutron response function dependent on the neutron interaction depth.

4.3.2 Scintillation Mode

LISe also belongs to a exclusive group of semiconducting materials possessing sufficient scintillation properties to operate in both modes of detection. Wiggins et al. estimated the yellow scintillating LISe light yield to be 4400 photons/MeV at a wavelength of 512 nm by coupling the crystal to a Hamamatsu 6533 PMT. The decay-time components were found to be 31 ns and 143 ns demonstrating a faster response than a comparably efficient CLYC detector (400 ns) [85]. Unlike semiconducting LISe, scintillating LISe demonstrates a narrow peak since scintillation yield is independent of charge carrier transport properties [85]. Similarly, Lukosi et al. demonstrated $\approx 80\%$ neutron absorption efficiency in a 960 μm thick LISe crystal compared to 11% efficiency for a 50 μm thick ZnS(Cu):^{6}Li scintillation screen [88]. Dual scintillation and semiconduction operation was investigated by Burger et al. demonstrating scintillation arriving 74 ns before the semiconduction signal as depicted in Figures 4.5a and 4.5b. Furthermore, the energy resolution for α spectroscopy was improved from 35% to 31% when summing coincident signals. These results prove scintillation occurs
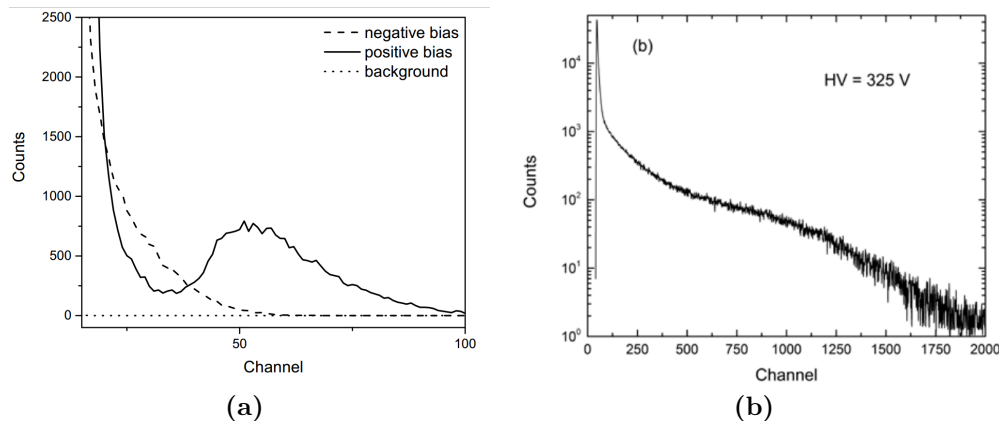
Figure 4.4: Early (a) α [63] and (b) neutron spectra [89] for LISe. The discrepancy in the α spectrum for positive and negative bias indicates electron transport is significantly better than hole transport for this material.

coincidentally with semiconduction indicating radiative recombination has a strong effect on the charge carrier transport properties.

4.3.3 Imaging

The aforementioned properties make LISe an interesting candidate for thermal and fast-neutron imaging applications. As such, the thermal neutron imaging capabilities have been investigated in semiconductor and scintillator modes [91–94]. As a part of the group developing LISe for neutron imaging applications, I contributed significantly to the work discussed in this section. It is presented here as a basis for the individual research discussed in Chapter 6. Spatial resolution measurements (Figures 4.6a and 4.6b) for scintillating LISe have demonstrated high spatial resolution and neutron absorption efficiency with a suitable light yield. Images were generated by coupling LISe to an ANDOR™ DW936 charge-coupled device (CCD) at the CG-1D beamline at Oak Ridge National Laboratory (ORNL). Spatial resolution was further improved, as high as $34\,\mu$m, by reducing back scattering with an anti-reflective backing (ARB) with the adverse effect of reducing light yield by a factor of 1.97. An internal memory effect due to the activated ^{115}In was not observed indicating this material would be useful for dynamic imaging applications. While the scintillation mechanism has yet to be identified, greenish-yellow regions of LISe have demonstrated significant increases in light yield while exhibiting $\approx 1\%$ decrease in absorption efficiency. These results indicate that
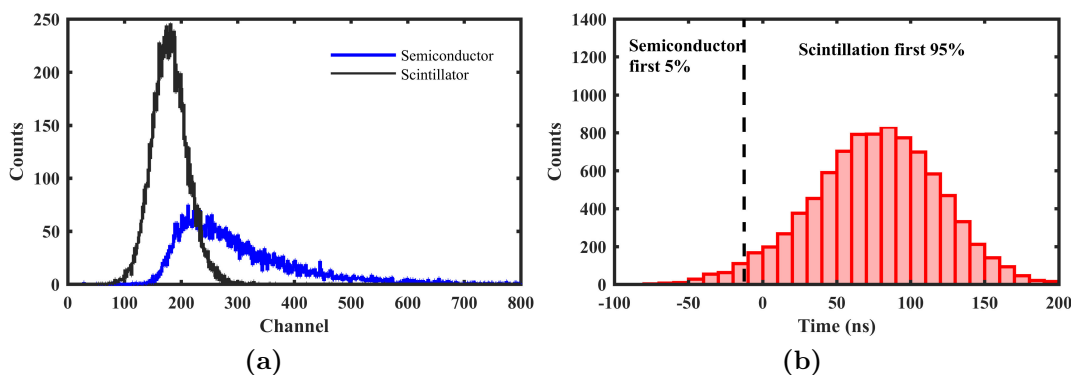
Figure 4.5: (a) Dual scintillation and semiconduction mode operation of LISe showing simultaneous response to α particles. (b) Time of arrival of scintillation and semiconduction signals. Scintillation signals arrive before semiconducting signals (95%) with a mean difference of $74\,$ns.

43

the increased brightness is a related to the scintillation activation site, which is a potential improvement vector [88, 93].

Herrera et al. demonstrated sub-pixel spatial resolution, $0.34\,\text{mm}$, in a 4×4 pixel ($0.55\,\text{mm}$ pitch) LISe imaging detector through the use of a super sampling technique where multiply images are taken of the same object as it traverses the imaging plane in sub-pixel steps. Encouraged by these results, LISe was coupled to a TimePix Application Specific Integrated Circuit (ASIC) to decrease the pixel pitch to $55\,\mu\text{m}$. Through slit (Figure 4.7a) and Siemens star (Figure 4.7b) resolution tests, the ultimate edge resolution of $34\,\mu\text{m}$ was found, while the high frequency resolution was determined to be on the order of $200\,\mu\text{m}$. High resolution images were acquired in a matter of minutes with the $10 \times 10^{11}\,\text{n}-\text{cm}^{-2}\text{s}^{-1}$ flux available at the CG-1D beam line housed at ORNL High Flux Isotope Reactor. Further improvements in performance are expected as the device fabrication and ASIC bonding process is improved.
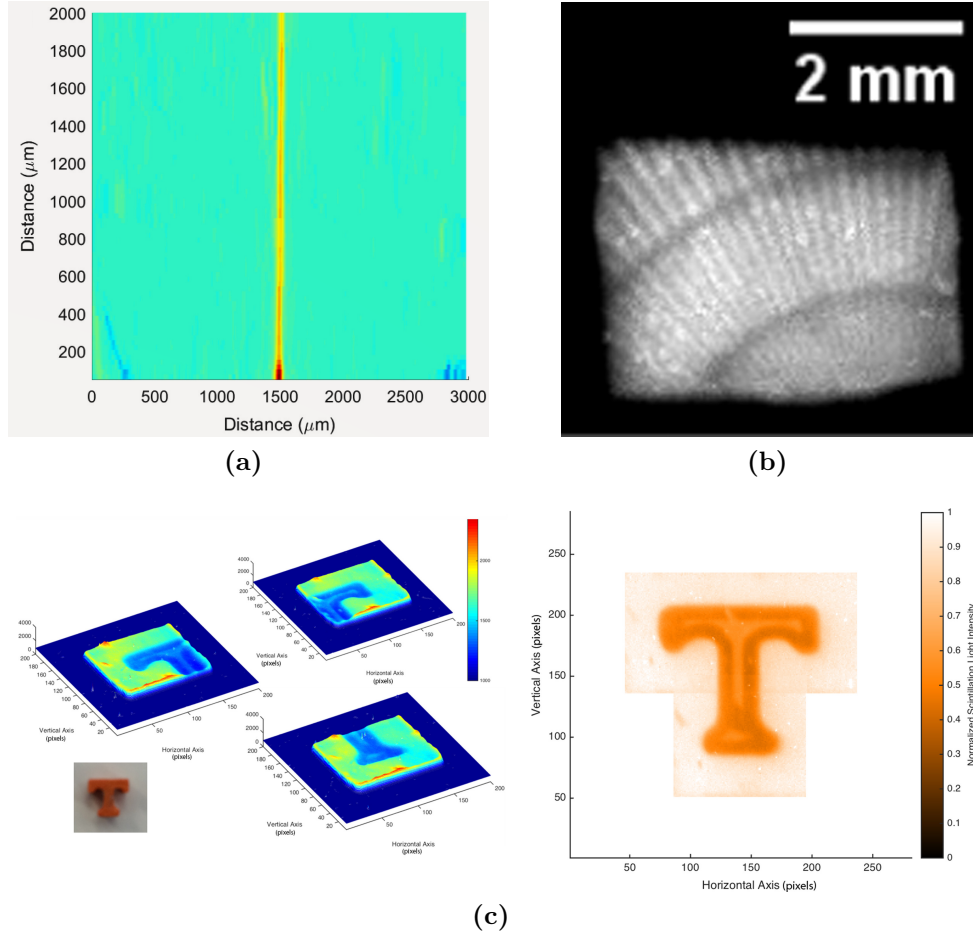
Figure 4.6: Cold neutron radiographs of (a) a thin gadolinium slit, (b) a Siemens star, and (c) a 3D-printed Power T™ using scintillating ^{6}LiInSe$_2$ imaged at HFIR's CG-1D beam line [88, 93].
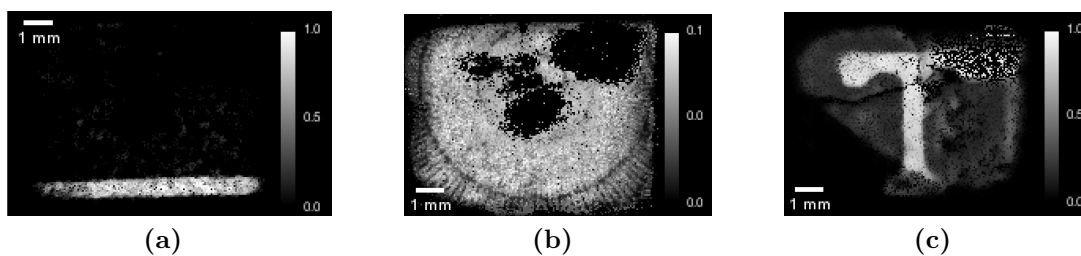
Figure 4.7: Cold neutron radiographs of (a)175 μm slit, (b) a Siemens star, and (c) a 3D-printed Power T™ using a pixelated (55 μm) ^{6}LiInSe$_2$ detector coupled to a TimePix ASIC imaged at HFIR's CG-1D beam line [94].

Chapter 5

Materials and Methods

5.1 Analyzed Samples

Due to the breadth of the studies discussed herein, it is important to clearly identify the various samples used. Samples are identified according to the following defining parameters - detector area and thickness, color, and high flux neutron exposure. Table 5.1 consolidates the sample identities as well as the experiments performed on those samples. In all cases, sample preparation remained consistent across all experiments, except for small changes for specific applications discussed in Sections 5.3 and 5.4. Crystal substrates of various sizes were cut from boules produced via the Vertical Bridgman technique detailed by Tupitsyn et al.[60]. Diamond lapping pads were used to polish the samples to a near optical finish to promote contact adhesion. A 5% bro-methanol etchant further reduced the surface roughness and removed any surface defects generated by the polishing process. Finally, semiconductor samples were metallized via RF magnetron sputtering in an AJA plasma sputtering chamber at a pressure of 3-5 mTorr. For fundamental characterization studies, gold planar contacts were deposited using a shadow mask configuration. In order to identify a robust, ohmic contact, numerous contact metals were investigated. Further discussion may be found in Section 5.2. For neutron imaging applications, substrates were patterned with pixelated arrays using photolithography as thoroughly discussed by Herrera et al. [94].

Table 5.1: Samples analyzed to characterize the electronic properties of LISe.

Sample	Area (mm^2)	Thickness (μm)	Color	Type	Irradiation (n/cm^2)	Study
L1	5×5	300 - 1700	yellow	semi	-	^aCCE
L2	5×5	532	yellow	semi	10^{12}	^aCCE ^bPICTS ^cRaman ^dPC $^eV_{TFL}$
L3	4×4	505	red	semi	-	^bPICTS ^cRaman ^dPC $^eV_{TFL}$
L4	4×4	454	yellow	semi	-	^bPICTS ^cRaman ^dPC $^eV_{TFL}$
L5	6×3	714	yellow	scint	10^{12}	^eRaman

^{a} Charge Collection Efficiency measurements
^{b} Photo-Induced Current Transient Spectroscopy
^{c} Raman Spectroscopy
^{d} Photoconductivity
^{e} Trap-Filled Limited Voltage

5.2 Contact Study

Semiconductor device packaging requires a robust contact that possesses excellent adhesion characteristics and appropriate electronic properties. As such, the development of any novel semiconductor relies heavily on the identification of a suitable contact material and deposition technique for both optimum performance characteristics and long-term operation of the device. This becomes increasingly important for advanced detector designs beyond the planar configuration. This study sought to identify a suitable Ohmic contact material with sufficient adhesion to withstand ultrasonic wire bonding as a prerequisite to the development and testing of the 16-channel LISe imaging detector reported on by Herrera et al. [91]. As described in Section 2.2.1, ultrasonic wire bonding is a technique used to electrically connect two components through an ultrasonic welding process. Preliminary studies showed that gold contacts demonstrated sufficient Ohmic behavior, but as shown in Figure 5.1, wire bonding failed due to poor contact adhesion. Several typical contact metals were deposited onto non-detector grade LISe and examined for ohmic behavior and good adhesion.

5.2.1 Contact Deposition

Aluminum, gold, chromium, and titanium contacts were investigated due to their extensive use in traditional wire bonding applications. Layered contacts employing a thin ($< 250\,\mathrm{nm}$) adhesion layer of chromium or titanium were also investigated. The use of an adhesion
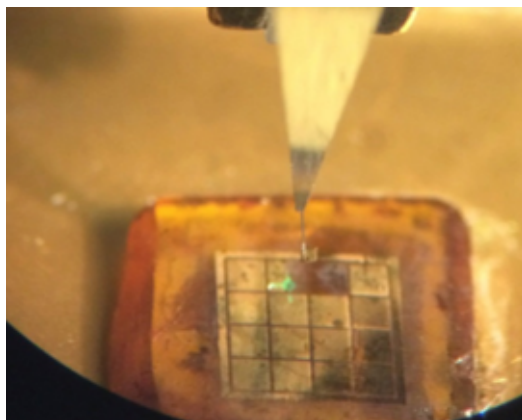
Figure 5.1: Preliminary testing of wire bonding on a LISe substrate with a pixelated array of gold contacts.

48

layer is widely used because Cr and Ti offer very good adhesion to a variety of substrates, a hard protective buffer against the force of wire bonding, and stability against diffusion [95]. Additionally, indium selenide (In$_2$Se$_3$) and pure indium (In) contacts were used due to their incorporation in bulk LISe with the expectation of good adhesion while protecting the single crystalline structure from surface defects. The surface of LISe was prepared through a polishing and etching procedure that reduced the surface roughness to the nm scale. This was done to promote adhesion and reduce the probability of non-uniform contact formation due to large ($> 1 \, \mu$m) substrate surface features. Contacts were deposited through the physical vapor deposition (PVD) technique, radio frequency magnetron sputtering. Sputtering is the process of bombarding a target material (e.g. Au, Ti, Al) with argon ions resulting in ablated target atoms being accelerated towards the substrate surface. The inner chamber of the AJA sputtering machine used in this study is shown in Figure 5.2. In order to create uniform contacts, substrate rotation is used to eliminate the deleterious effects of the mono directional deposition process. Similarly, the effects of in-situ and post-deposition contact annealing, a technique that promotes the metallurgical bonding of contact to the substrate, were also investigated. Contact deposition occurred at at the working pressure of the sputtering chamber (30-50 mTorr).
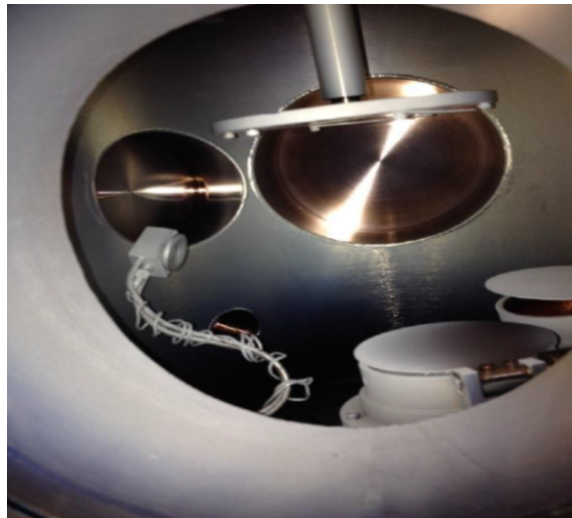
Figure 5.2: Internal image of an AJA sputtering chamber with a bottom-up deposition configuration. This system is equipped with a rotating substrate holder (top), quartz crystal thickness monitor (left), and two source cathodes (bottom right).

5.2.2 Contact Analysis

Electrical Characterization

Deposited contacts were characterized using current-voltage (IV) measurements to determine the electrical behavior is Ohmic or Schottky. As a highly resistive material with an operating voltage on the order of 150-700 V, the IV relationship was determined up to $\pm100\,\text{V}$ and examined for rectification. Due to an observed relaxation response, the positive and negative voltage sweeps were acquired separately beginning at 0 V. The leakage current was measured using a Keithley 6485 Picoammeter, which also supplied the external bias. Ten consecutive current measurements were made at each voltage in order to decrease the noise at low currents and ensure the crystal stabilized at each applied bias.

Adhesion

Initial adhesion testing employed the simple, but effective, tape test. Kapton tape was applied directly to the contact surface and subsequently removed. Contacts that survived the tape test procedure were then examined for wire bondability. An exemplar diagram of a wire bond is shown in Figure 5.3, where the first bond is typically made on the elevated bond pad surface of a die or printed circuit board (PCB). The second bond is then made on the substrate surface. In this study, the relative elevation of the two bonds are inverse due to the relatively large thickness of the LISe substrate and PCB design. Gold wire with a diameter of 0.001" (1 mil) was chosen due to its stability over the cheaper, but effective, aluminum wire often used in wire bonding applications. Gold wire, as a noble metal, does not form an appreciable oxide layer that can sometimes lead to bond failure.

The bonding process occurs in several steps:

1. The gold wire is fed through a small capillary in the wedge tip outfitted with custom groove designs to promote bonding.

2. The wedge is slowly lowered to a "search height" just above the surface of the first bond location. This height is typically 2-3 times the diameter of the wire.

3. Bonding is initiated as the wedge tip is pressed against the bond pad while a clamp secures the wire. This force applied by the wedge to the bond pad is variable and depends on the contact material.

4. A transducer vibrates the wedge at an ultrasonic frequency while maintaining contact between the wire and bond pad. The variable parameters, ultrasonic power and sonication time, are used to optimize the bonding procedure.

5. Once the first bond is complete, the wedge makes a series of movements designed to reduce the force applied to the first bond site while the second bond is performed.

6. Finally, the second bond is completed in the same manner as the first with an additional shearing motion. Since the bond pad/contact materials are almost always different, the force, power, and duration settings are often different from the first bond.

This is typically a trial and error process for each contact material, with careful consideration of the fragility of the LISe substrates. Wire bond failure is typically evident during the bonding process due to either contact liftoff (poor adhesion) or bond failure (improper bond parameters). However, a pull test is required to ensure that the wire bond is successful and not simply resting on the surface of the contact. A gentle pull on the apex of the wire, as shown in Figure 5.3, is the final adhesion test.
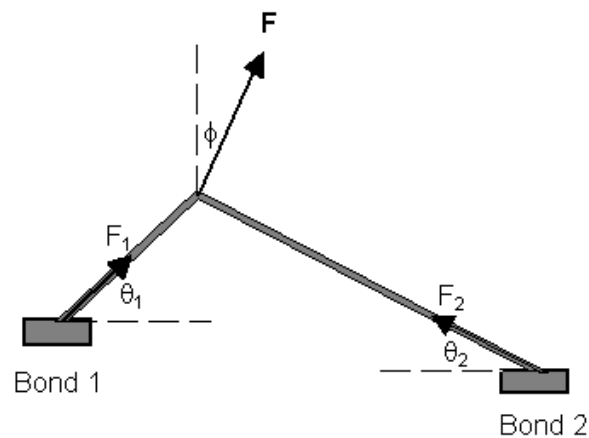
Figure 5.3: Force diagram of the wire bonding process. Ultrasonic/thermosonic wire bonding form a metallurgical joint by superheating the wire and bond pad through ultrasonic vibrations.

5.3 Characterization

Development of LISe for neutron detection and imaging applications, as with every new detection material, requires a fundamental knowledge of the electronic properties of the material. The fundamental properties, W-value and $\mu\tau$ product, are important to understand the limitations of this material, while characterizing defects and the effects of radiation damage are necessary for growth optimization and long-term stability. This section describes the numerous studies performed on LISe to provide insight on the fundamental characteristics of the material. The ionization energy per electron-hole pair, W, and the charge carrier mobility-lifetime products, $\mu\tau$, were investigated through charge collection efficiency (CCE) techniques like alpha spectroscopy and preamplifier rise time studies. A highly irradiated LISe sample was investigated to compare its post-irradiation operation properties to non-irradiated samples using the aforementioned CCE studies, as well as additional defect studies. Defect energies were characterized using photoinduced current transient spectroscopy. Trap density was identified through trap-filled limited voltage (V_{TFL}) measurements. Neutron and alpha spectroscopy under various conditions were investigated to understand the emergent polarization phenomenon exhibited by the irradiated LISe sample. Additionally, Raman spectroscopy and temperature-dependent Photoconductivity measurements were used to supplement these studies and identify differences as a function of color and irradiation.

5.3.1 Charge Transport Properties

Alpha and Neutron Spectroscopy

LISe samples were placed in a device under test (DUT) enclosure where the contacts were electrically connected to processing electronics using a spring-loaded electrode on top and conductive pad underneath. The bottom circuit board was outfitted with a 3-mm diameter exposure port for α irradiation. The pulse processing chain consisted of a CAEN A1422 preamplifier with a gain of 8.4 V/pC, an ORTEC 572A Linear Amplifier with a shaping time of $1\,\mu$s and a gain of 100 for electrons and 250 for holes, and an ISEG NHQ High Voltage Power Supply. The analog voltage pulses were digitized using an ORTEC 927 ASPEC MCA. The experimental setup was calibrated with a diamond detector, where the rate of alpha

particles impinging the detector for the two ^{210}Po sources used was 2.3 and 6.9 α/second. Additionally, electron transient voltage pulses from the preamplifier were acquired using a 1.5 GHz Agilent Oscilloscope 54845A to directly measure the mobility and trapping time constant of LISe.

The pulse processing chain for alpha and neutron spectroscopy measurements are depicted in Figure 5.4. The small pulse amplitudes of holes inhibited effective acquisition of transient voltage pulses from the preamplifier due to noise interference. Several experimental measurements were conducted to quantify the influence of alpha exposure, the magnitude of the applied bias, and diode wavelength on the observed charge collection and subsequent polarization observed in the irradiated sample.

Due to the short range of α particles ($24\,\mu$m for 5.3 MeV $\alpha's$), the Hecht relation, given in Equation 2.10, can be simplified for a single charge carrier since the majority of the signal is generated by the charge carrier that is drifted towards the distance electrode [23, 24]. Thus, electron/hole only charge collection can be accomplished by irradiating the cathode/anode, respectively. This simplification makes it possible to determine the electron and hole mobility-lifetime product separately, as shown in Equation 5.1. Since CCE is a function of the applied electric field, E, $\mu\tau$ can be extracted from a fit of Equation 5.1 to a plot, shown in Figure 5.5, of the charge collected, Q, where Q is defined as the peak of the alpha spectrum.

$$CCE = \frac{Q}{Q_0} = \frac{(\mu\tau)_{e,h}E}{d}\left(1 - exp\left(-\frac{d}{(\mu\tau)_{e,h}}\right)\right) \tag{5.1}$$

Separating the $\mu\tau$ product into its constituents requires a time-dependent analysis of the charge collection process [96]. Applying the single carrier approximation to Equation 2.9, $Q(t)$ becomes

$$Q(t) = Q_0\frac{\mu\tau E}{d}\left(1 - exp\left(-\frac{t}{\tau}\right)\right) \tag{5.2}$$

At time $t = \infty$,

$$Q(t = \infty) = \frac{Q_0\mu\tau E}{d} \tag{5.3}$$
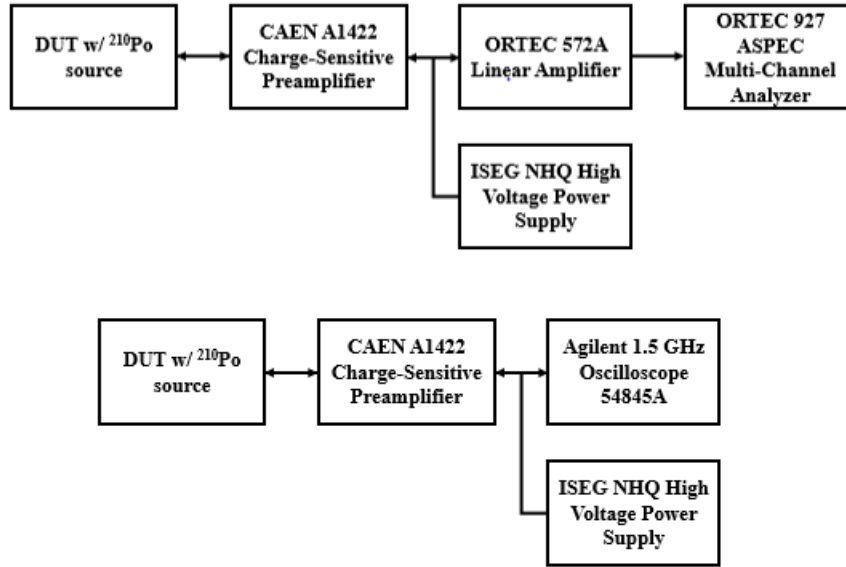
Figure 5.4: Pulse processing chains for alpha and neutron spectroscopy (top) and alpha-induced electron time-of-flight (ToF) measurements.
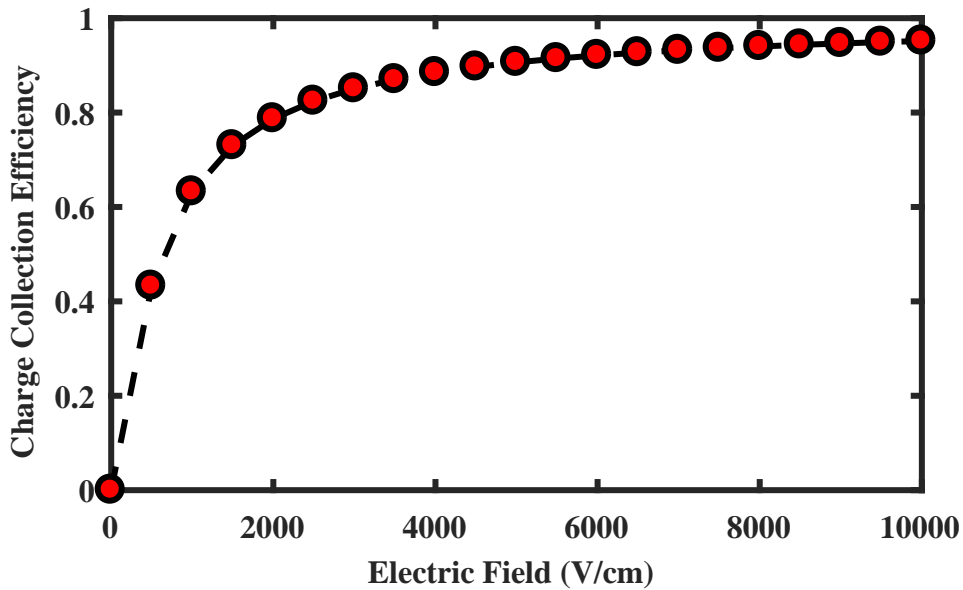
Figure 5.5: Charge collection efficiency as a function of applied bias assuming no trapping. CCE approaches 100% as $\frac{d}{\mu\tau E}$ approaches 0.

Therefore, Equation 5.2 can be expressed as

$$Q(t = \infty) - Q(t) = \frac{Q_0 \mu \tau E}{d} \exp\left(-t/\tau\right) \tag{5.4}$$

$$\log Q(t = \infty) - Q(t) = \log\left(\frac{Q_0 \mu \tau E}{d}\right) - t/\tau \tag{5.5}$$

Thus, the charge carrier lifetime, τ, can be determined independently of the mobility by applying Equation 5.5 to the integration of the drifting charge by the preamplifier, as shown in Figure 5.6a. Given that the rise time of the preamplifier is much less (2 ns) than the drift time of the charge carriers, the preamplifier rise time is equivalent to the transit time, t_r. Not only is this useful for determining τ, but also can be used to identify μ since t_r is proportional to the drift velocity, v_d, as shown in Equation 5.6.

$$v_d = \frac{d}{t_r} = \mu E \tag{5.6}$$

Due to the amplitude small pulses $(4mV)$ and high signal-to-noise ratio (SNR), 1,000 preamplifier pulses were acquired at each voltage between 100 and 500 in 25 V steps and analyzed using MATLAB. Waveforms were collected at a 500 MHz sampling frequency by triggering on the amplified preamplifier pulse since the preamplifier signals were too small to reliably trigger acquisitions. The signals were then smoothed using a broad low-pass filter to eliminate the high frequency noise component. Due to an effect known as time jitter, caused by inconsistencies in oscilloscope triggering on the amplified current pulses, the filtered pulses were aligned so that averaging the waveforms would not artificially inflate t_r. Once the waveforms were averaged for a given applied bias, the 10-90% rise time was evaluated by first identifying the state levels, Q_0 and $Q(t = \infty)$, as shown in Figure 5.6b. These measurements were performed on L1 as a function of thickness and L2.

Since L2 demonstrated polarization during the CCE measurements, long-term stability measurements and combined α-n spectroscopy were performed to characterize this phenomenon. Polarization is a process often observed in highly irradiated semiconductor detectors where radiation induced damage create a time-dependent radiation response within the detector. The effect of polarization on the CCE measurements was removed by switching
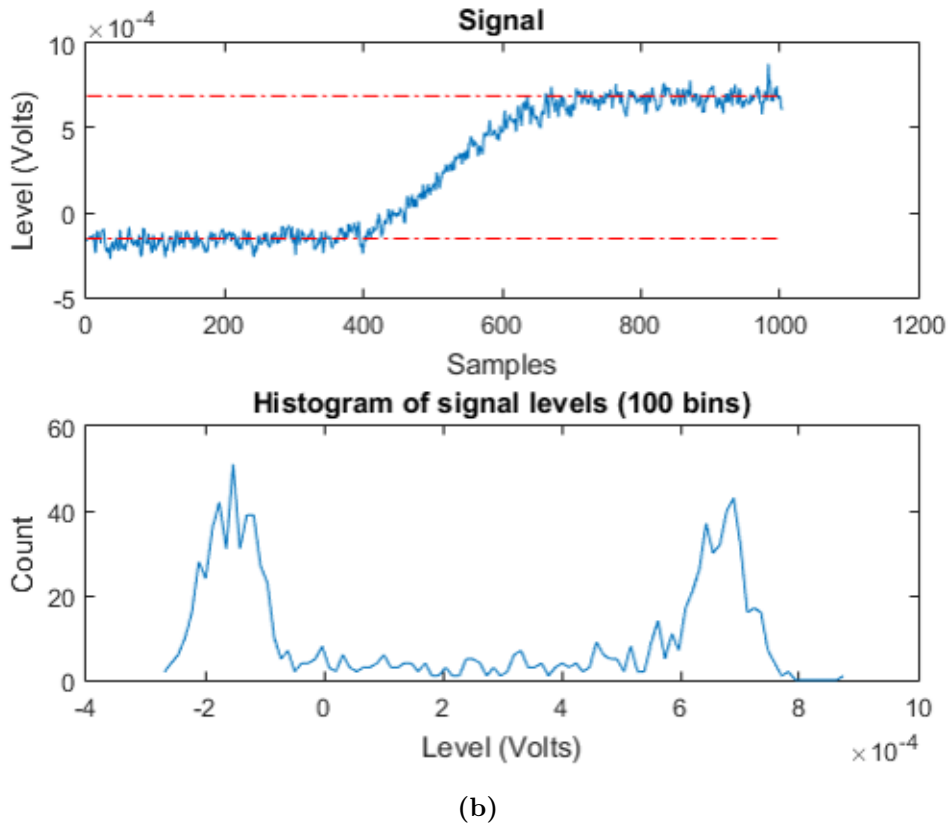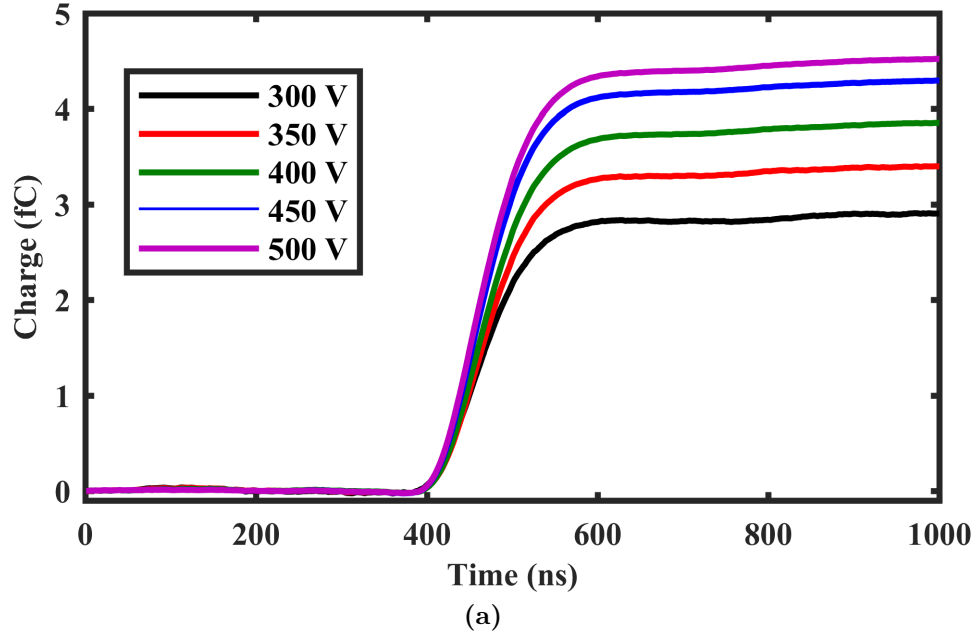
Figure 5.6: (a) Current pulses captured from a CAEN A1422 charge-sensitive preamplifier for LISe exposed to 5.31 MeV α-particles (^{210}Po). Amplitude and rise time are expected to increase with increasing electric field as dictated by the Hecht relation.(b) Rise time analysis technique. An amplitude histogram (bottom) of the waveform defines the upper and lower state levels in order to quantify the 10-90% rise time (top).

the applied bias between measurements and allowing the built up charge to detrap. This typically occurs when a high charged-defect density creates a layer of charge, also known as space-charge buildup, that opposes the applied electric field. This effect is analogous to the formation of the depletion region in p-n junction detectors. A moderated plutonium-beryllium (2 Ci) α-n source was used to characterize the response of L2 in a neutron-only and mixed-α-n field to compare the charge collection of the 5.3 MeV α particles from ^{210}Po and the 4.78 MeV ^{6}Li thermal neutron capture reaction, which are expected to have similar peaks. The pulse processing chain shown in Figure 5.4 was used, but the amplifier gain was reduced to ensure the spectrum remained within the dynamic range of the MCA. Additional long-term stability measurements were made to understand how the α and neutron spectra change as a function of time under bias and the effects of reverse biasing.

5.3.2 Defect Characterization

Photo-induced Current Transient Spectroscopy

Photo-induced Current Transient Spectroscopy (PICTS), a method for determining the charge carrier trap energies, evolved from deep-level transient spectroscopy (DLTS). These techniques probe deep-levels by filling the traps with charge carriers and observing the detrapping lifetime as a function of temperature. While DLTS is a proven and powerful technique for junction based semiconductors, it fails for high resistivity materials where charge injection is more difficult [97]. PICTS overcomes this obstacle by using a pulse of light to generate charge carriers in the material while under bias, filling the trap states with drifting carriers. Once the traps are filled, the photocurrent saturates. The excitation source has a relatively short penetration depth such that the majority of carrier drift is from only one carrier. As the pulse cycles off, the photocurrent decays in two stages: (1) a rapid decay due to free carrier recombination (0 to t_0) and (2) a thermally stimulated release of trapped carriers (t_0 to t_∞). Since a majority of these carriers are either electrons or holes, this technique can differentiate electron and hole traps. The photocurrent difference $\Delta i_{12} = i(t_1) - i(t_2)$ as a function of temperature and emission rate, e_n, can be used to determine the activation energy, E_{Act}, of the charge carrier traps via the relation,

$$e_n = e_0 T_m^2 \exp\left(-\frac{E_{Act}}{kT_m}\right) \tag{5.7}$$

where e_0 is the emission coefficient, T_m is temperature where Δi_{12} peaks, and k is the Boltzmann constant. The relationship between the photocurrent decay and temperature is illustrated in Figure 5.7.

By varying the rate window and recording T_m, an Arrhenius plot can be constructed where the slope is proportional to the E_{Act}, as demonstrated in Figures 5.8a and 5.8b. The rate window is inversely proportional to the initial delay, t_1, such that t_2 is dependent on the selection of t_1. The normalized two-gate method is used due to the strong temperature dependency of μ [98]. Here, the PICTS signal, Δi_{12}, is normalized by the photocurrent amplitude to reduce the sometimes overbearing shift in photocurrent as a function of temperature. Therefore, the PICTS signal is the fractional decay of the photocurrent within the selected rate window. Additionally, the emission rate, e_n, is then given by the relation

$$\frac{1}{e_n} = \tau_m = \frac{t_2 - t_1}{ln(t_2/t_1)} \tag{5.8}$$
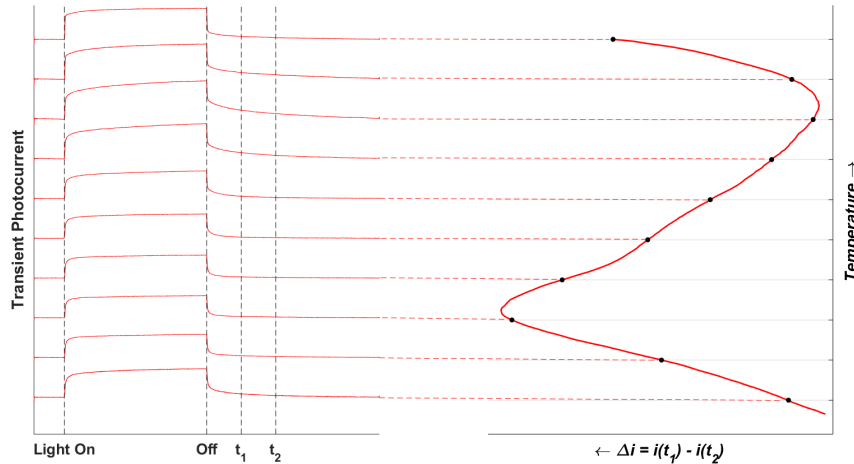
Figure 5.7: Transient current pulses (left) at increasing temperatures and the current differential, Δi, (right) at each of those temperatures. The peak corresponds to a specific electrically active trap.
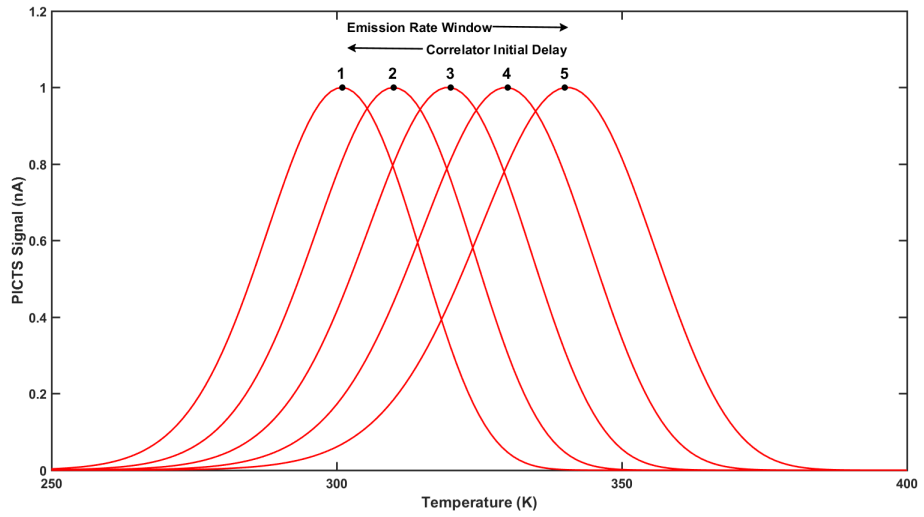
(a)
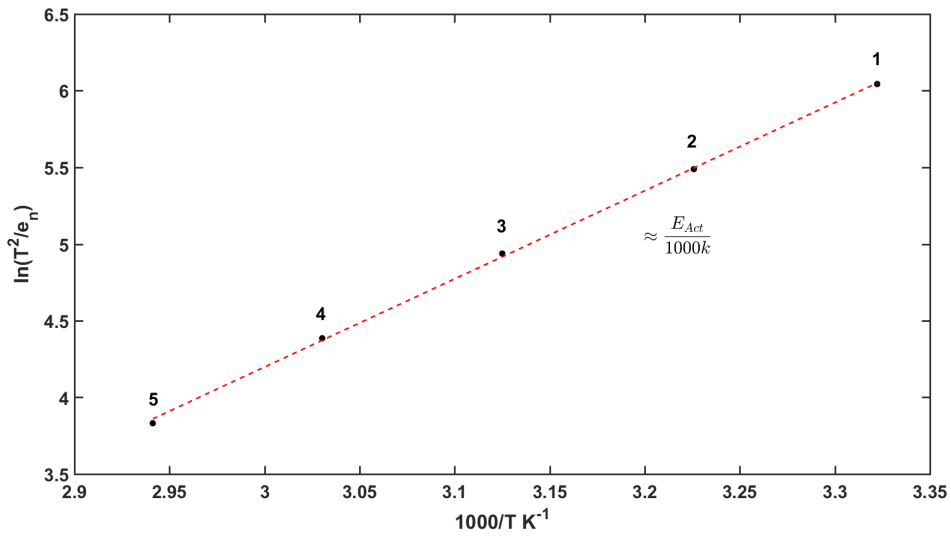
(b)

Figure 5.8: (a) Simulated PICTS spectrum for a $0.5\,\mathrm{eV}$ trap for various correlator delays/emission rates. (b) Arrhenius plot of the peak temperatures from (a) where the slope is proportional to the activation energy, E_{Act}, of the trap.

PICTS measurements were performed on samples L2, L3, and L4, but only L2 produced a sufficient response. Early attempts at this measurement used a SULA DLTS system designed for lower resistivity materials like Si and GaAs. The amplification stages were not well suited for LISe so a custom two-stage transimpedance amplifier (TIA) was built with a gain of 1000 including low-pass filtering. Similarly, the data processing software did not allow fine control of the rate windows so a custom LabVIEW software was developed to collect and store raw waveforms in list mode for offline processing in MATLAB. Photocurrent decay waveforms were generated by pulsing a nine LED array of white light (emission spectrum shown in Figure 5.9) at 5 Hz (50% duty cycle) while the crystal was biased at $\pm 10\,V$. The crystal was cooled in a JANIS VPF800 Cryostat to liquid nitrogen temperatures. To increase the signal-to-noise ratio of the system, RG-174 cables were installed to reduce to the leakage current as shown in Figure 5.10.

Photocurrent decay waveforms were collected continuously (1 MHz sampling frequency) as the sample was heated at a rate of $\approx 4\,K/min$ using a LakeShore 335 Temperature controller. The decay profiles were averaged at every 1 K interval to reduce the overall noise of the signal, then each average waveform was passed through a Fourier low-pass filter to remove high frequency noise components. The normalized signals for electrons and holes are shown in Figures 5.11a and 5.11b , respectively. Normalized two-gate PICTS spectrum was extracted using a double-boxcar averaging technique, where the currents i_1 and i_2 are computed by averaging the currents around t_1 and t_2. Since the decay current approaches the noise floor as t increases, the width of the boxcar around t_1 and t_2 are proportional to their magnitude. Finally, the PICTS spectral peaks were extracted to build the Arrhenius plot depicted in Figure 5.8b. The validity of this process was verified by simulating the photocurrent decay with a single trap at $0.5\,eV$. The results ($E_{Act} = 0.497 eV$) are shown in Figures 5.8a and 5.8b. The results are compared to a similar PICTS study by Cui et al. [67].
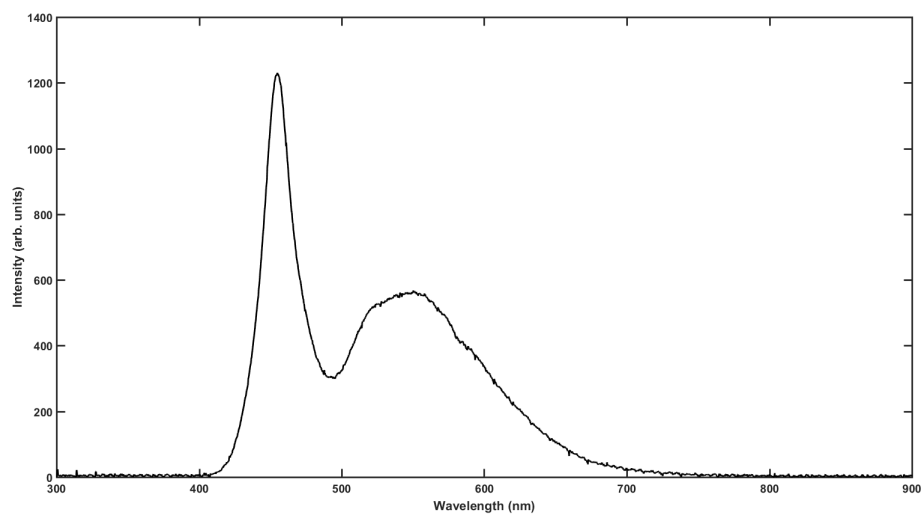
Figure 5.9: Wavelength spectrum of white light led array used for Photoconductivity and Photoinduced Current Transient Spectroscopy measurements.
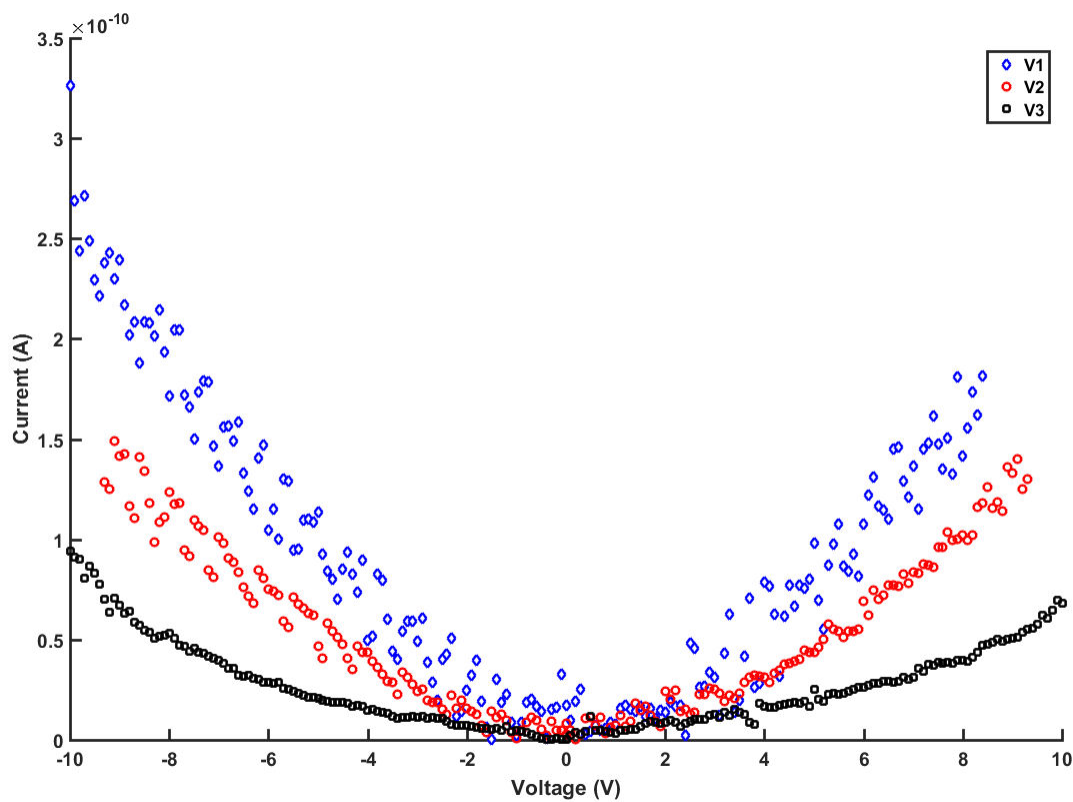
Figure 5.10: Leakage current in the JANIS VPF800 cryostat after various iterations. The leakage current was measured with probe tips suspended in vacuum.
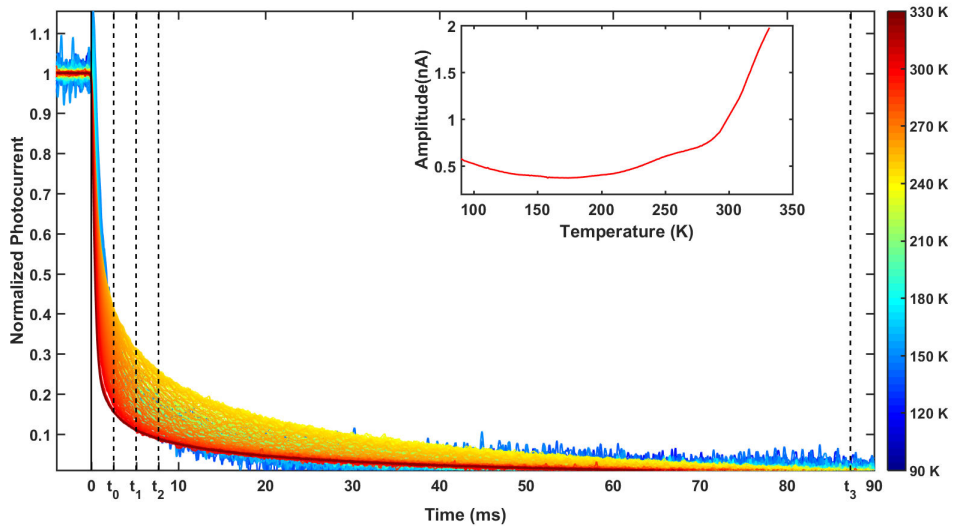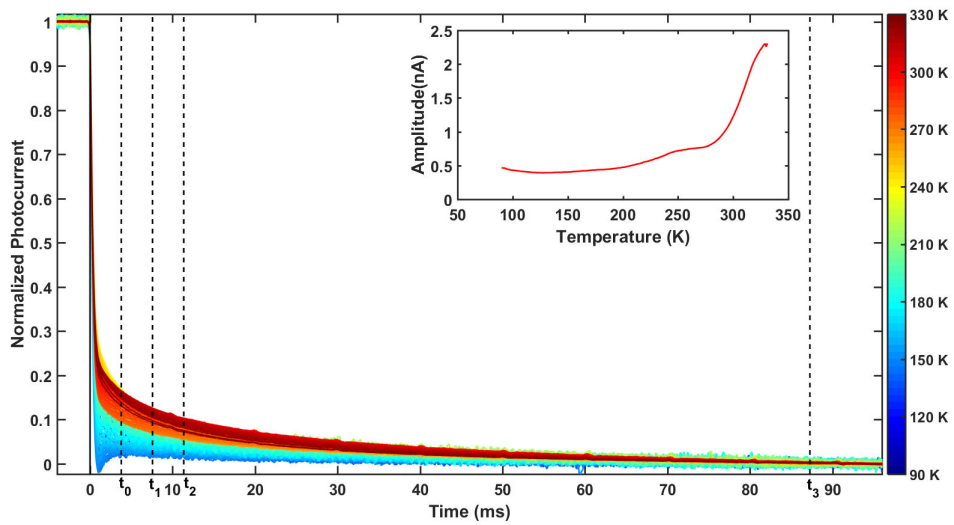
Figure 5.11: Normalized photocurrent decay of L2 over the temperature range 90 K to 330 K for (a) cathode and (b) anode illumination at a constant 10 V bias. (inset) Photocurrent amplitude over the same temperature range.

Trap-filled Limited Voltage

Trap-filled limited voltage (V_{TFL}) measurements, first described by Lampert [25], is predicated on the current-voltage characteristics of a semiconductor. At low applied biases, current density, J, is proportional to voltage according to Ohm's law,

$$J = \frac{I}{A} = \frac{qn_0\mu V}{L} \tag{5.9}$$

where q is the charge of an electron, n_0 is the thermal equilibrium free electron concentration, and L is the distance between the electrodes. As the current and the free carrier density increases, these free carriers begin to fill the charge carrier traps in perpetuity. Thus, the IV relationship shifts from trap-dominated to trap-free as described by Child's (Mott-Gurney, for semiconductors) Law,

$$J = \frac{9}{8}\frac{\epsilon\mu V^2}{L^3} \tag{5.10}$$

where ϵ is the dielectric constant. The transition point, as shown in Figure 5.12, is V_{TFL} and is given by,

$$V_{TFL} = \frac{qN_tL^2}{\epsilon} \tag{5.11}$$

where N_t is the trap density. V_{TFL} measurements were performed on samples L2, L3, and L4 using the same methodology described in Section 5.2.2 to compare the relative trap density of detector grade, non-detector grade, and irradiated LISe. V_{T}FL was estimated from the deviation from the power law ($\propto V^2$). Trap density, N_t, was calculated assuming a dielectric constant of 8.5 as demonstrated in literature (see Section 4.2).

5.3.3 Miscellaneous Measurements

Raman Spectroscopy

Raman spectroscopy is a technique often used to examine the vibrational properties of a material. Since the vibrational modes are related to the chemical and molecular bonds
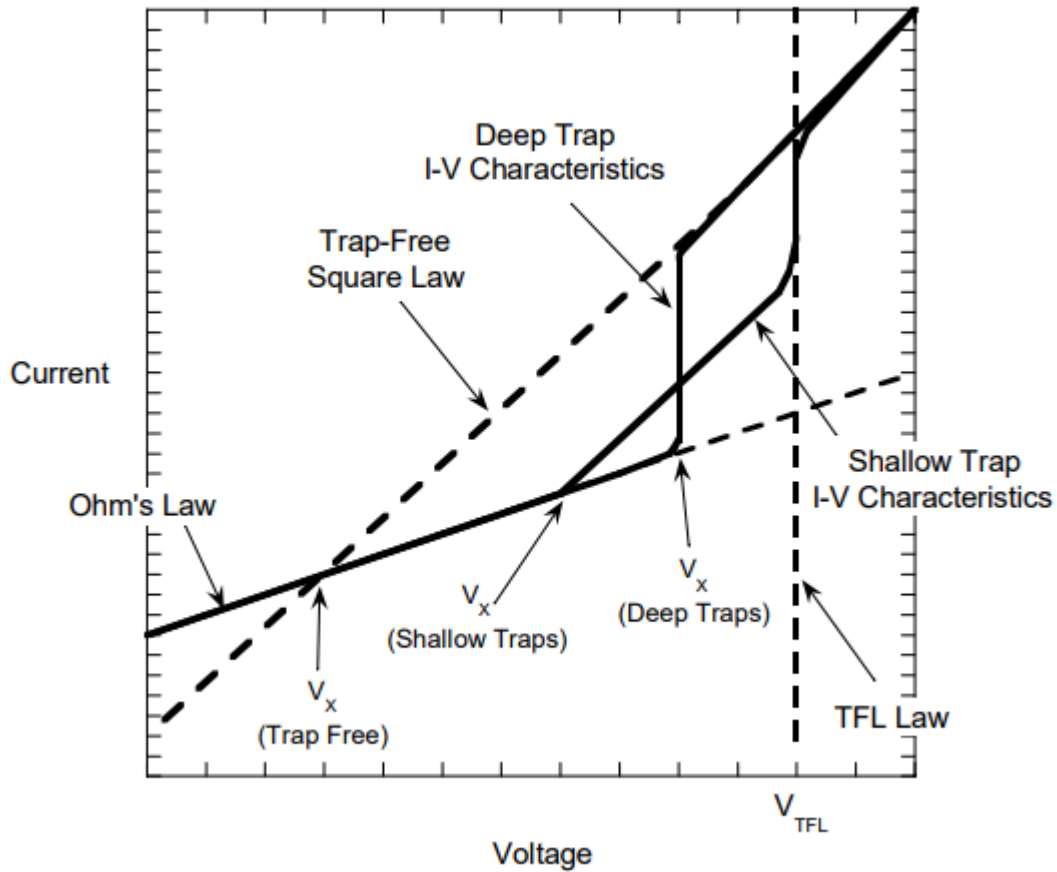
Figure 5.12: Space-charge limited current voltage relationship assuming a single, exponentially distributed trap energy. The trap-filled limited voltage marks the beginning of the Child's Law ($I \propto V^2$) regime indicating the current density is large enough to fill all charge carrier traps [99].

present, it can be used to identify certain materials. The fundamental principle of Raman spectroscopy is the slight energy loss or gain of an incident light source due to interactions with the vibrational modes of a material. A photon with energy, $h\nu$, impinges the target where the oscillating electromagnetic wave induces a reciprocal oscillating molecular dipole moment.

Raman scatter photons only comprise a very small fraction of the incident photons with the majority being reflected or photoluminescence. Photoluminescence photons are emitted when an incident photon is absorbed and the excited electron releases the absorbed energy in the form of other photon PL peaks can appear in Raman spectra, but, unlike Raman peaks, their energy is independent of the incident photon. Different wavelengths of light can be used to discern Raman spectral peaks from photoluminescence since the Raman shift (energy lost or gained) is constant, irrespective of the incident photon energy. Figure 5.13a illustrates the Jablonski band diagram illustrating the energy loss/gain from Stokes/Anti-Stokes Raman scattering.

Raman spectra for samples L2, L3, L4, and L5 were recorded with a Horiba Scientific LABRAM HR Evolution. A 785-nm wavelength laser was projected onto the surface of the samples. A 50x objective lens and 1800 gr/mm grating were used to focus the laser and record the spectra. After a preliminary investigation, the spectrometer range was limited to

(a)	(b)
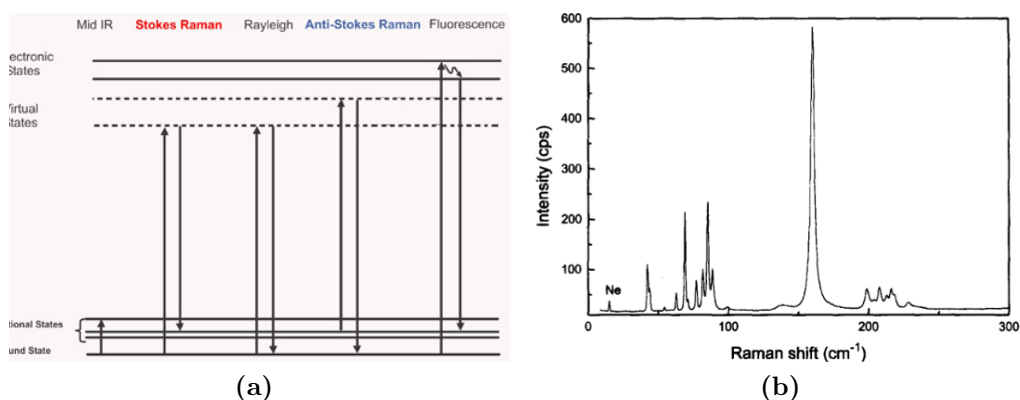
Figure 5.13: (a) Jablonski energy band diagram describing the excitation/de-excitation processes that can occur. Stokes/Anti-Stokes Raman shifts are a result of photonic energy loss/gain from interaction with the vibrational modes of a crystalline structure, which are a product of the chemical bonds within a material. Image courtesy Horiba. (b) Representative Raman spectrum of LISe from literature [74].

0-350 cm^{-1} as this region was found to be devoid of PL photons. The results were compared against color and irradiation and to literature [68, 74]. An exemplar Raman spectrum from Lorenz et al. is shown in Figure 5.13b.

Photoconductivity

As a supplement to PICTS, photoconductivity measurements were acquired as a function of temperature for three photon sources - broad spectrum white light, UV (395 nm), and green (520 nm). The spectrum for the white light is provided in Figure 5.9 with strong emissions in the blue and green wavelengths. The photocurrent was recorded at a constant bias of 100 V continuously from 90-300 K in order to quantify the dependence of the PICTS decay on the amplitude of the photocurrent. Samples L2, L3, and L4 were investigated to compare the relative response to color and irradiation.

5.4 Fast Neutron Radiography

LISe has demonstrated promise in thermal neutron imaging. This section outlines the expansion of the thermal neutron imaging work to fast neutron imaging in semiconductor mode. As a proof-of-principle, the spatial resolution of the Timepix-coupled LISe detector was investigated for monoenergetic fast neutrons. Section 5.4.1 covers the construction of the Timepix module as detailed by Herrera et al. [94]. Section 5.4.2 describes the monoenergetic fast neutron source at Edwards Accelerator Laboratory at Ohio University. Section 5.4.3 describes the experimental design and processing technique used to determine the spatial resolution of the LISe detector.

5.4.1 Timepix Coupled Detector

The Timepix ASIC is a high spatial resolution charge readout chip originally developed for medical X-ray and γ-ray imaging applications, although its been demonstrated for neutron detection [43]. It is an evolution of the Medipix2 ASIC with additional read-out modes for time-sensitive imaging applications like time-over-threshold and time to first detection. The full ASIC is an array of 256×256 pixels with dedicated preamplifiers and discriminators for

each channel. The pixelated array spans 14.08 mm with each pixel occupying a $55\,\mu\text{m} \times 55\,\mu\text{m}$ area. In Medipix mode, the ASIC operates as a simple single channel analyzer (SCA) registering counts above a user-defined threshold. The ASIC is coupled to the LISe substrate via a flip-chip bump bonding process performed by X-ray Imatek. Figures 5.14 and 5.15 show the $9 \times 7 \times 0.5\,\text{mm}^3$ LISe crystal bonded to the Timepix ASIC only covering a quarter of the available pixels. The ASIC and detector module are coupled to the pulse processing module (right in Figure 5.15) via a ribbon cable. A custom MATLAB-based graphical user interface (XRI-GUI) was provided by X-ray Imatek (XRI) to control the detection module.

5.4.2 Edwards Accelerator Laboratory

Edwards Accelerator Laboratory at Ohio University is home to a 4.5-MV Tandem Van de Graaff accelerator as depicted in Figure 5.16a. Equipped with a Peabody Scientific cesium source, the facility is capable of accelerating ^{1}H, ^{2}H, Li, B, and C beams. The accelerated beam is directed using a beam swinger, described in [100], toward two target rooms and time-of-flight tunnel. The 30-m flight tunnel provides ToF capabilities for high energy resolution neutron beams. The target source located at the end of the beam swinger, coupled with the variety of beams available, allows the facility to generate continuous monoenergetic neutrons up to 26 MeV [101]. Figure 5.16b shows the various monoenergetic neutron energy spectra for the d(d,n) reaction measured 6.195 m from the center of a 3-cm diameter deuterium gas cell. These spectra were acquired with the beam swinger at 0° with respect to the time-of-flight tunnel demonstrating 1×10^8 neutrons/(sr MeV μC) capabilities.

5.4.3 Spatial Resolution

Spatial resolution is a defining factor for imaging detectors as it succinctly quantifies the smallest feature a device can resolve. For fast neutron imaging applications, spatial resolutions on the order of millimeters are desirable for many applications. Knife-edge resolution tests are one of the most widely used methods to quantify the spatial of an imaging system due in part to its simplicity. The knife edge is a highly attenuating material with a sharp, well-defined edge with sufficient size to shield part the detector from the incident

(a)   (b)
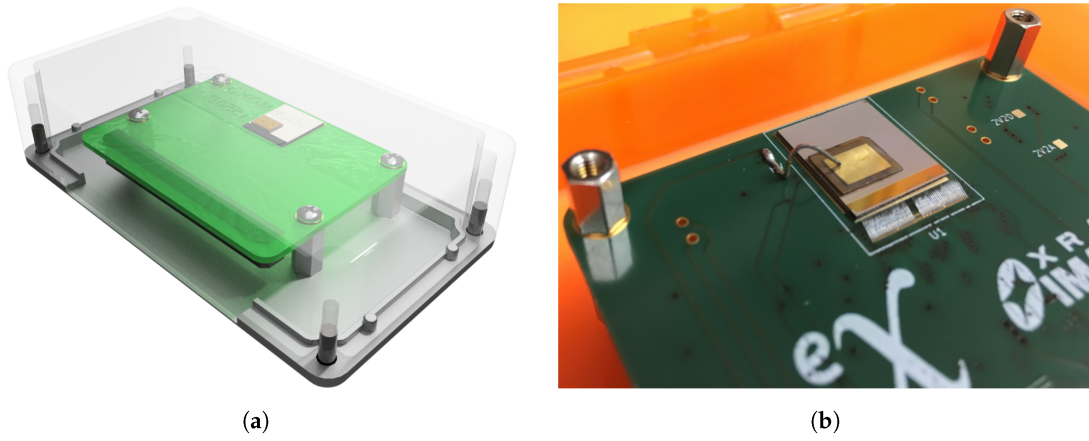
Figure 5.14: (a) Computer-aided design (CAD) drawing of the Timepix-coupled LISe detector. (b) LISe crystal coupled to Timepix ASIC via flip-chip indium bump-bonding process by X-ray Imatek [94].
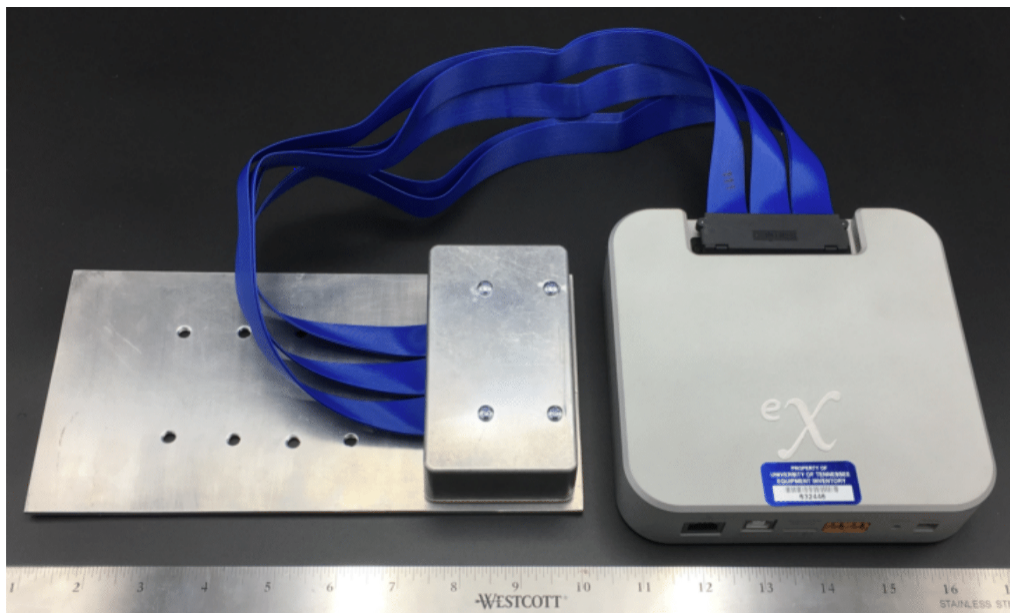
Figure 5.15: Timepix-coupled LISe module with readout electronics.
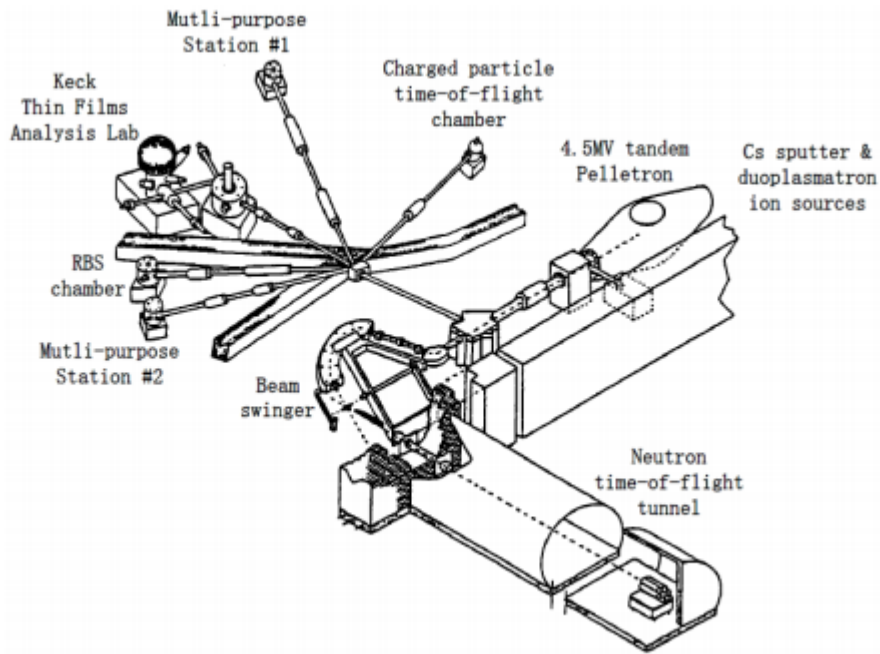
(a)
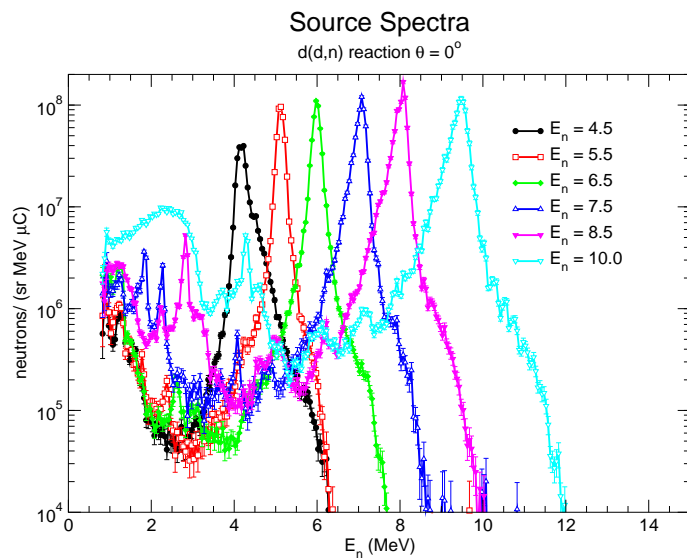
(b)

Figure 5.16: (a) Diagram of Edwards Accelerator Laboratory at Ohio University. (b)Source spectra for the d(d, n) reaction at various accelerated deuteron energies [101].

neutron (or photon) beam. The attenuating object must be positioned as close as possible to the imaging plan (e.g., LISe surface) to reduce blurring effects from geometric unsharpness of the beam.

Beam Divergence

"Geometric blur" emerges from a loss of contrast due to divergence of the interrogation beam as shown in Figure 5.17. The degree of resolution degradation is a function of the collimation of the system, which can be characterized by the source-to-target distance, L, and the diameter of the collimation aperture, D. From Figure 5.17, it is clear to see that the ratio L/D is equivalent to the ratio of the object-to-detector distance, l, to the geometric blurring, d [102].

$$\frac{L}{D} = \frac{l}{d} \tag{5.12}$$

The geometric blurring and spatial resolution limit of the imaging system are additive in nature so the ultimate resolution, U_t, has a lower bound for a given geometric configuration. Increasing the source-to-target distance and/or decreasing the diameter of the collimation aperture reduces geometric blurring, at the expense of neutron flux. Since flux from a point source is governed by the inverse-square law, every 2-fold decrease in geometric blurring reduces the geometric efficiency by a factor of 4 for a fixed object-to-detector distance. This trade-off is best optimized according to the specific experimental requirements for acceptable resolution and image acquisition time. Here, the detector was placed 4.1 m from the centerline of the deuterium gas cell. The collimation port leading to the ToF tunnel has a diameter of 20 cm giving an L/D ratio of 20.5, which is small for many neutron imaging applications. The knife edge object, a $15 \times 5 \times 3\text{cm}^3$ copper block, was placed in contact with the detector housing so d is the distance from the outside face of the aluminum enclosure to the front surface of the LISe detector, or 2.1 cm. Thus, the expected geometric blurring is on the order of 1 mm.
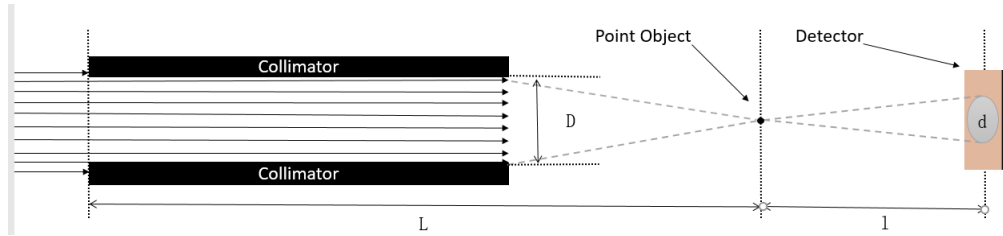
Figure 5.17: Notional diagram of geometric blurring due to uncollimated neutrons. The scale is exaggerated for clarity. For the knife edge test, L = 4.1 m, D = 0.2 m, l = 0.02 m, and d is ≈ 1 mm.

Modulation Transfer Function

The Modulation Transfer Function (MTF) is a well-documented and extensively employed method for quantifying spatial resolution across a broad spectrum of imaging systems. The MTF of an imaging system is best described in terms of contrast as it relates the loss of contrast, or blurring, to the spatial frequency of an imaged object. Contrast is a measure of the intensity range of a given imaging system. Figure 5.18 illustrates the loss of contrast as the spatial frequency of line pairs increases. This relationship between contrast and spatial frequency comprises the theoretical framework of the MTF. A knife edge is an impulse input into the MTF for a given detector since the system is given a sharp sub-pixel step change from an open beam to a highly attenuated beam. The output of the MTF in the spatial domain is visualized as image blurring. To obtain the MTF, the response of an imaging detector perpendicular to the knife edge, known as the edge spread function (ESF), is extracted, as shown in Figure 5.19. Differentiation of the ESF yields the line spread function (LSF), which is Gaussian in shape. Both ESF and LSF have been used, historically, to quote spatial resolution. The 10-90% rise in contrast in the ESF has been shown to approximate the spatial resolution of a system. Similarly, the full-width at half-maximum (FWHM) of the LSF possesses some theoretical foundation as a metric for spatial resolution. However, MTF, which can be obtained using a discrete Fourier transform of the LSF, provides the most informative definition of spatial resolution due to its relevance to the spatial frequency of an imaged object. From this measure, spatial resolution is often quoted at 10% of the MTF, a value rooted in the Rayleigh Criterion for diffraction-limited circular aperatures [103].
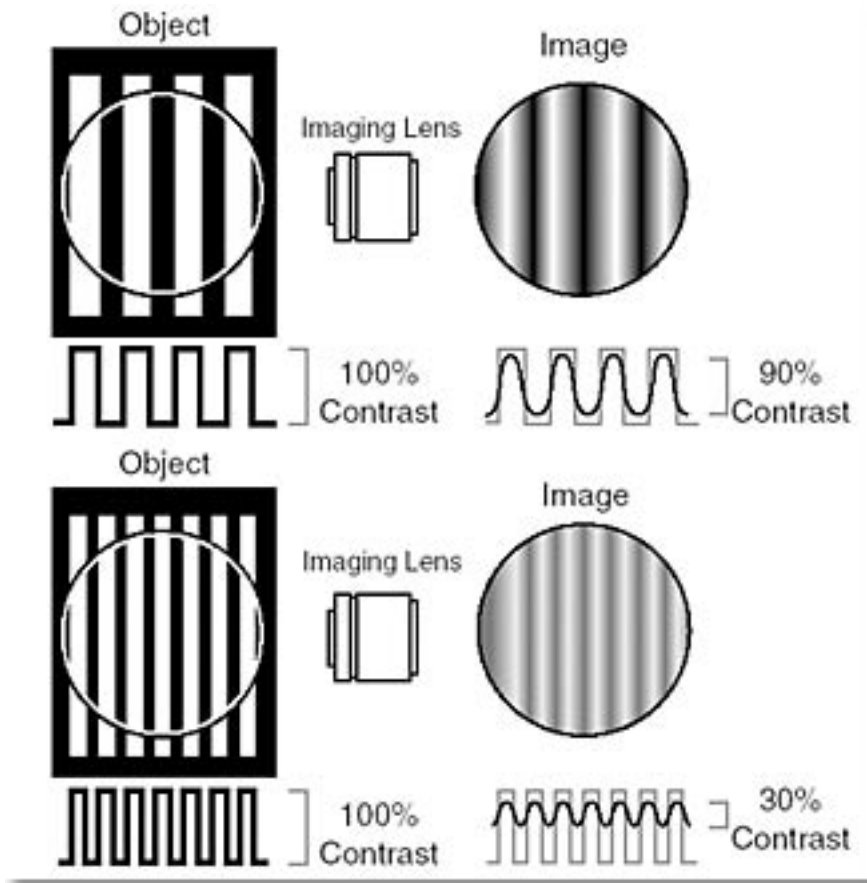
Figure 5.18: Fundamental limitations of spatial resolution are dependent on the loss of contrast as a function of spatial frequency. Courtesy Edmund Optics.
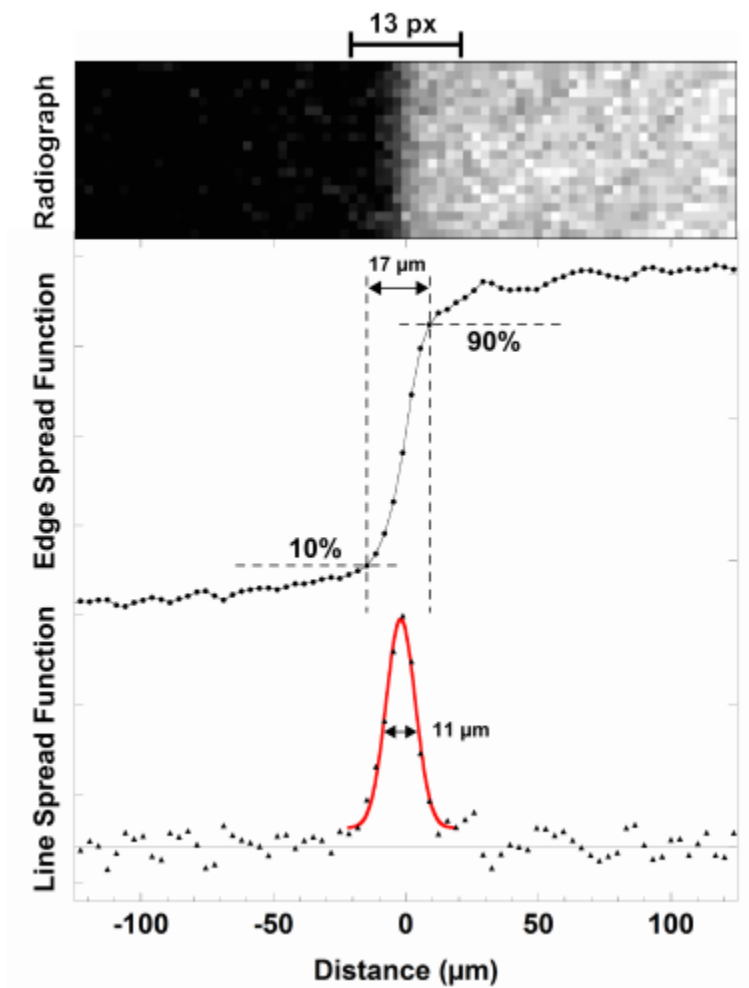
Figure 5.19: Example of calculation of the Edge Spread Function and Line Spring Function from a Knife Edge [103].

5.4.4 Experimental Setup

For this investigation, a fast neutron energy of $9\,\text{MeV}$ was desired so a deuteron beam and target gas cell were chosen resulting in an approximate flux of 2×10^8 neutrons/(MeVsrμC) as shown in Figure 5.16b. The accelerator provided a steady beam current of $3.4\,\mu\text{A}$ during operation. Due to flux and detection efficiency constraints, the parameters for operation were derived for thermal neutron imaging application. As such, a constant 250 V bias was applied to the detector during acquisition while a threshold of 4 mV was employed to maximize the number of true fast neutron counts. Figures 5.20, 5.21, and 5.22 depict the beam swinger, ToF Tunnel, and the detector setup. Sheets of cadmium foil were used to eliminate any thermal neutrons from the source and down scattering from nearby walls.

Dark field measurements were acquired to identify "hot" pixels, which are defined pixels that recorded counts while the beam was off before and after neutron exposure. Since this measurement spanned two days, four total dark field measurements were acquired. The "hot" pixels identified in the dark field were masked during post processing. A $15 \times 5 \times 3$ cm^3 solid copper block was used to create the knife edge effect across the imaging plane effectively attenuating the $9\,\text{MeV}$ to 3% of the open-beam intensity. As a consequence of low count rate, the edge spread function had to be constructed by summing pixel columns perpendicular to the knife edge. The LSF was calculated by differentiating ESF in the typical manner, then normalized. A spline interpolation fit was used to super sample the LSF for the conversion to MTF. A discrete, fast Fourier transform (MATLAB fft) was applied to the LSF to obtain the MTF where the final resolution was determined at the intersection of the MTF and 10% threshold.
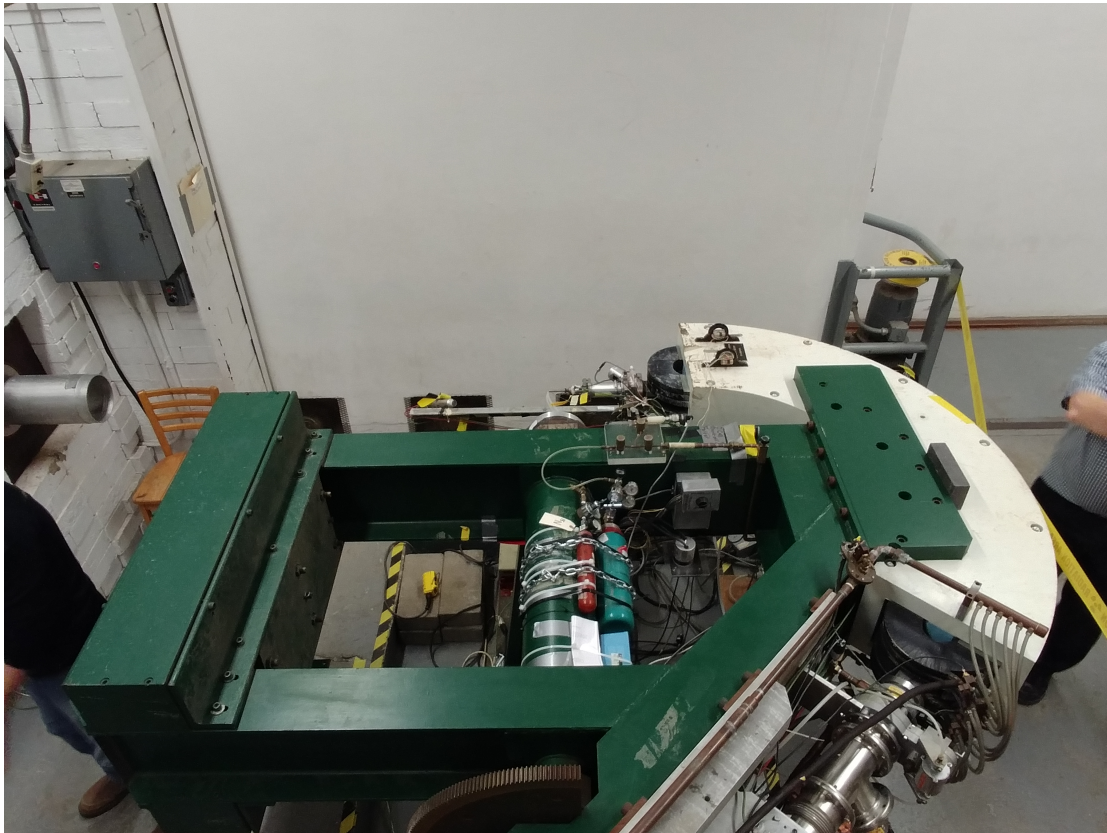
Figure 5.20: Image of the beam swinger position at 0°. The deuterium gas cell is mounted parallel with the flight tube allowing the accelerated deuteron to pass through the long axis of the gas cell. The 20-cm collimation port on the right leads to the 30-m ToF tunnel.

Figure 5.21: Image of the experimental setup with the detector. The collimation port and detector were covered with a thin layer of Cd to eliminate moderated thermal neutrons.
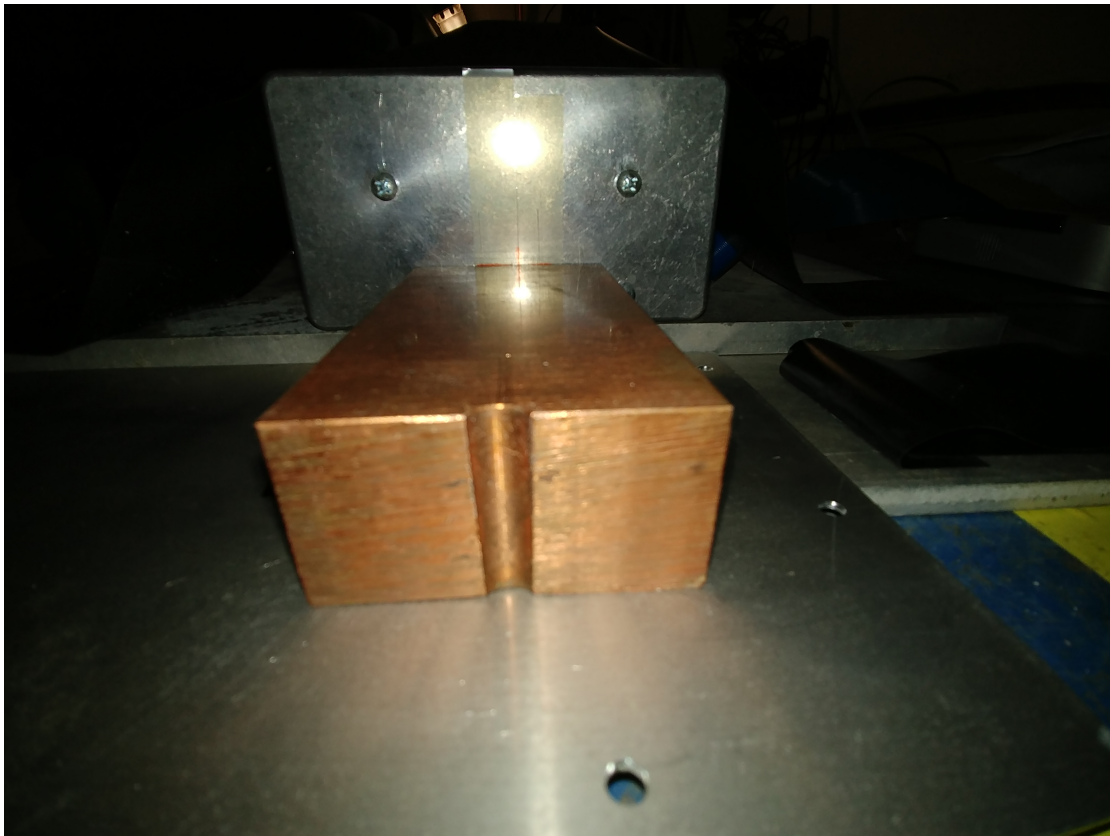
Figure 5.22: Image of the knife edge experiment where the top edge of the copper attenuator was aligned to the centerline of the detector.

Chapter 6

Results and Discussion

As the penultimate chapter, the results of the various studies are presented and discussed. Section 6.1 provides an overview of the contact materials, structures, and deposition techniques investigated in the search for a robust contact suitable for semiconductor packaging. Section 6.2 details the study of the electronic properties of LISe and the emergent polarization phenomenon observed in irradiated samples. Section 6.3 presents the fast neutron radiography proof-of-principle studies outlining the total spatial resolution and efficiency of the system. Congruently, these results represent a series of novel contributions to the development of a promising neutron detection material that will influence future development at the fundamental growth level and provide insight on the applicability of this material for the varied uses of neutron detection and imaging.

6.1   Robust Wirebondable Contact

Through trial and error, RF magnetron sputtered indium contacts were shown to possess ohmic current-voltage characteristics and excellent adhesion to LISe. The oft-used Cr/Ti adhesion layers did not increase the survivability of sputtered contacts despite their well-documented use in wire bonding applications. In thin layers, these materials are often useful due to the strongly bonded oxide states and their resistance against deformation during wire bonding. Due to the force required to create strong bond-wire connections, unprotected substrate surfaces are prone to cratering, where the surface becomes visibly damaged.

This surface damage creates defects and strongly increases the surface recombination rates. Without the mechanically hard CrO/TiO interface states, thick films ($\approx$ 1000 nm) are employed to reduce surface damage.

When the aforementioned contact structures consistently failed, two contact materials, In_2Se_3 and In, were identified as potential candidates. It was hypothesized that elementally similar contacts would provide mechanically stable metal-semiconductor hetero-junctions. However, In is a notoriously soft material with a low melting point, indicating it would not perform well as an adhesion layer. While In_2Se_3 exhibited excellent adhesion, wire bonding failed at the bond-wire interface. Thus, indium contacts were deposited with the additional application of in-situ substrate heating at 350 K. The elevated substrate temperature promotes metallurgical bonding at the substrate interface like post-growth annealing. Figures 6.1a and 6.1b show the wire bonding for the In:LISe hetero-junction. Table 6.1 catalogs the various materials and layers studied in the search for a mechanically robust contact.

<div align="center">(a)   (b)</div>
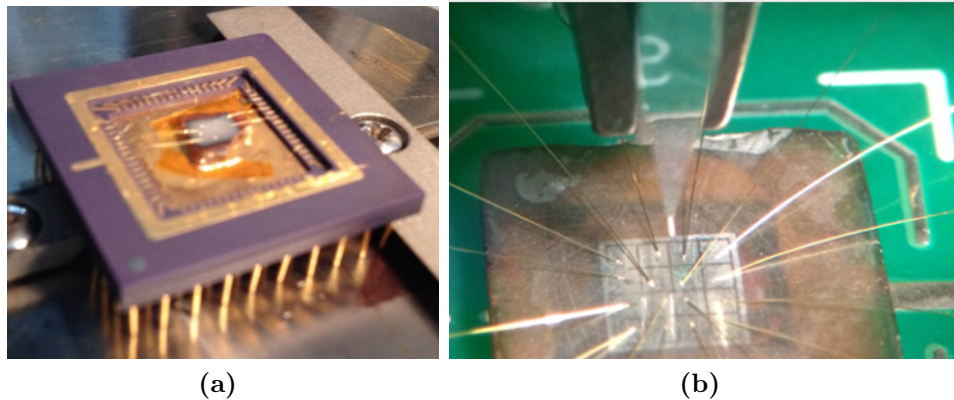
Figure 6.1: (a) Initial successful wire bond with a final In thickness of 1000 nm deposited via RF magnetron sputtering at 100 W and 75 °C. (b) Final successful wire bonding on the LISe Thermal Neutron Imager (LTNI).

IV measurements were taken for each of the contact materials, as described in Section 5.2. Ohmic behavior was observed for all materials, with a representative sample provided in Figure 6.2a. The In:LISe heterojunction exhibited a slight rectifying behavior as illustrated by the asymmetry of the leakage with respect to bias polarity. Further, the quality and uniformity of the Au wire bond was investigated for the 16-channel LTNI by examining pixel-by-pixel IV relationship. As shown in Figure 6.2b, slight differences in IV are observed for each channel. The variation in IV is a combination of material inhomogeneities and the repeatability of the wire bonding process. Nevertheless, the pixelated substrate was used to demonstrate semiconductor-mode thermal neutron imaging capabilities for LISe as reported in [104].

6.2 Fundamental Characterization

Understanding the fundamental charge carrier generation, transport, and recombination properties drives the development of novel detection materials. Often, materials are selected based on these properties, and then modified to suit specific detection applications. Conversely, LISe was identified for its intrinsic neutron absorption efficiency. Consequently, development of this material requires a well-defined growth-characterization feedback loop to refine and optimize the crystal quality. This section details efforts to characterize LISe.
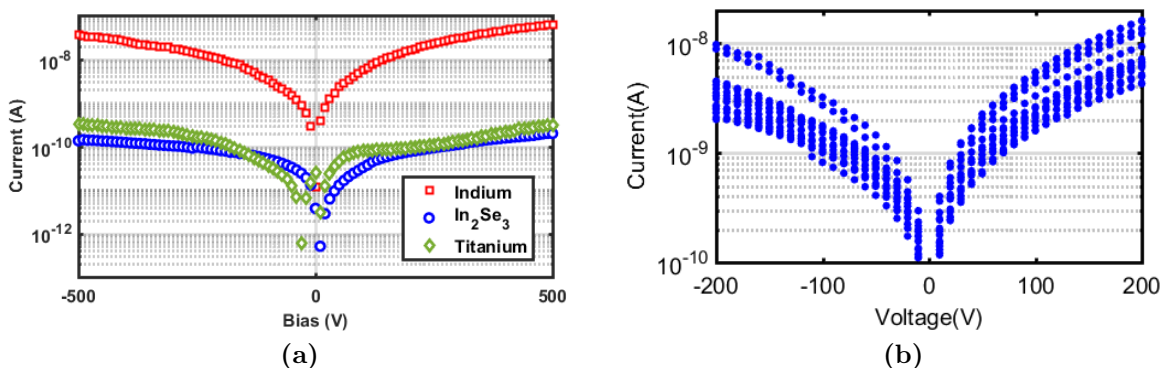
Figure 6.2: (a) Representative IV characteristics of In, In_2Se_3, and Ti contacts on LISe. (b) IV characteristics of all 16 pixels of LTNI showing slightly rectifying behavior.

Table 6.1: Summary of adhesion test results for each of the investigated contact schemes. The contact material and thickness, t, are described for the adhesion layer and bond layer. For single layer contacts, the properties are listed under bond layer.

Adhesion Layer		Bond Layer		Annealing		Adhesion Test	
Material	Thickness (nm)	Material	Thickness (nm)	T (°C)	Time (hr)	Tape	Wirebond
-	-	Au	100	-	-	Fail	Fail
-	-	Au	200	-	-	Fail	Fail
-	-	Au	500	-	-	Fail	-
Ti	50	Au	200	-	-	Fail	-
Ti	200	Au	500	-	-	Fail	-
Al	50	Au	25	-	-	Fail	-
Al	100	Au	25	-	-	Fail	-
Al	850	Au	25	-	-	Fail	-
Al	1000	Au	25	-	-	Fail	Fail
Ti	25	Au	25	-	-	Fail	-
Ti	50	Au	50	250	2	Fail	Fail
Ti	250	Au	400	400	0.08	Fail	Fail
Ti	150	Au	150	400	2	Fail	Fail
Ti	150	Au	200	275	0.08	Fail	Fail
Cr	150	Al	150	275	2	Fail	-
		Al	200	275	2	Fail	-
In_2Se_3	500	Au	500	-	-	Pass	Fail
		In	1000	75	0.08	Pass	Pass

6.2.1 Charge Generation and Transport Properties

Mobility-Lifetime Product

The charge-carrier mobility lifetime product, $\mu\tau$, for samples L1 and L2 were determined via fitting the Hecht relation to the CCE as a function of applied bias. The charge carrier properties for sample L1 were investigated as a function of detector thickness. The fits of Equation 2.10 for two thickness of L2 are shown in Figure 6.3a. Figure 6.3b illustrates the relationship between $(\mu\tau)_e$ and thickness. For an initial thickness of $1700\,\mu$m, $(\mu\tau)_e$ was found to be $110 \times 10^6\,\mathrm{cm^2/V}$. As the sample was thinned through mechanical polishing, the $(\mu\tau)_e$ suffered proportionally to the thickness, x, according to the empirical fit,

$$(\mu\tau)_e = (1.67 \times 10^4\,\mathrm{cm^2/V})x^{2.65} \tag{6.1}$$

At the minimum investigated thickness, $307\,\mu$m, the $(\mu\tau)_e$ was reduced to $3.8 \times 10^{-6}\,\mathrm{cm^2/V}$. The reduction of mobility-lifetime product is attributed to an increase in bulk defects from the mechanical polishing process. An increase in defect density is correlated with a proportional decrease in τ.

L2 α spectra for electrons and holes, the first of its kind reported, is shown in Figure 6.4a. From the single-carrier approximation to the Hecht equation for charge collection efficiency, it is reasonable to estimate that $(\mu\tau)_h$ is a factor of 10 less than $(\mu\tau)_e$. Analysis of the CCE curve for L2 yields a $(\mu\tau)_e$ of $5.5 \times 10^{-6}\,\mathrm{cm^2/V}$, which agrees well with L1 and Bell et al. [59]. Further analysis of the preamplifier rise time for L2 and application of Equation 5.5, the electron mobility and lifetime were determined separately. The measured μ_e was $122\,\mathrm{cm^2/Vs}$, on par with other wide band gap materials. The irradiated sample demonstrated a trapping time constant, τ_e, of $45\,$ns, which is attributed to the radiation-induced defects.

Preamplifier current pulses demonstrated a steady incline after the initial fast rise due to charge drift through the bulk semiconductor. The slower, secondary rise is indicative of a shallow carrier drift with a detrapping time constant of the same order of magnitude as the charge integration time. Differentiation of the preamplifier pulses obviate the contribution of detrapped charge to the overall signal, as shown in Figure 6.5. The effective detrapping time constant (τ_D) denotes the emission rate of a charge-carrier trap, which is heavily dependent
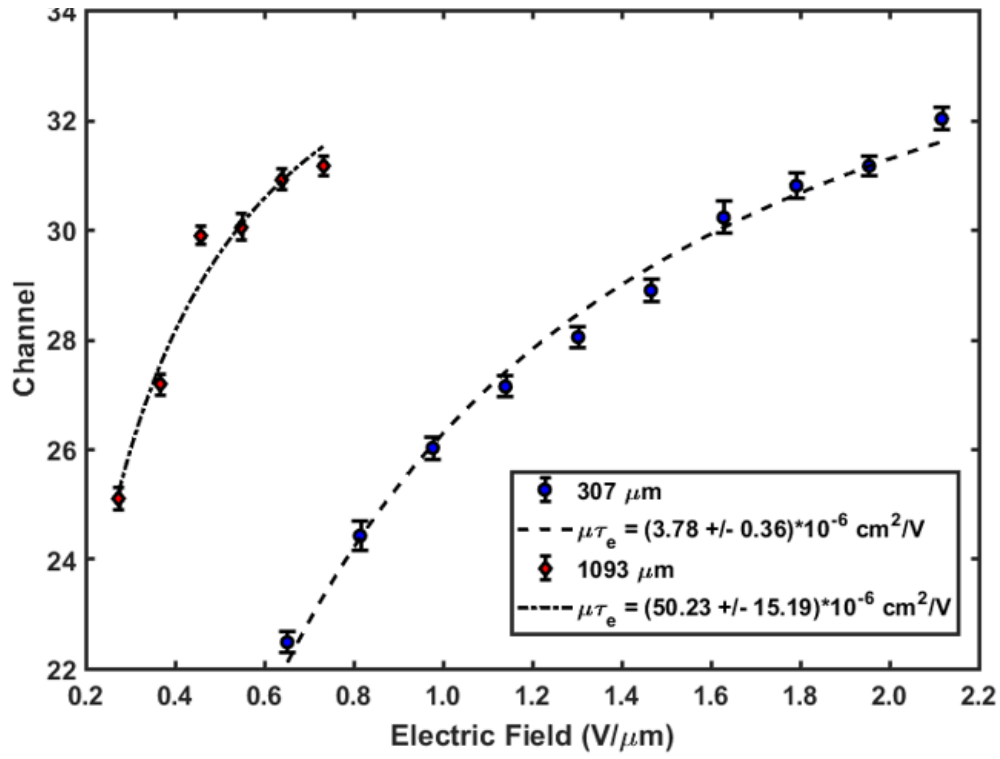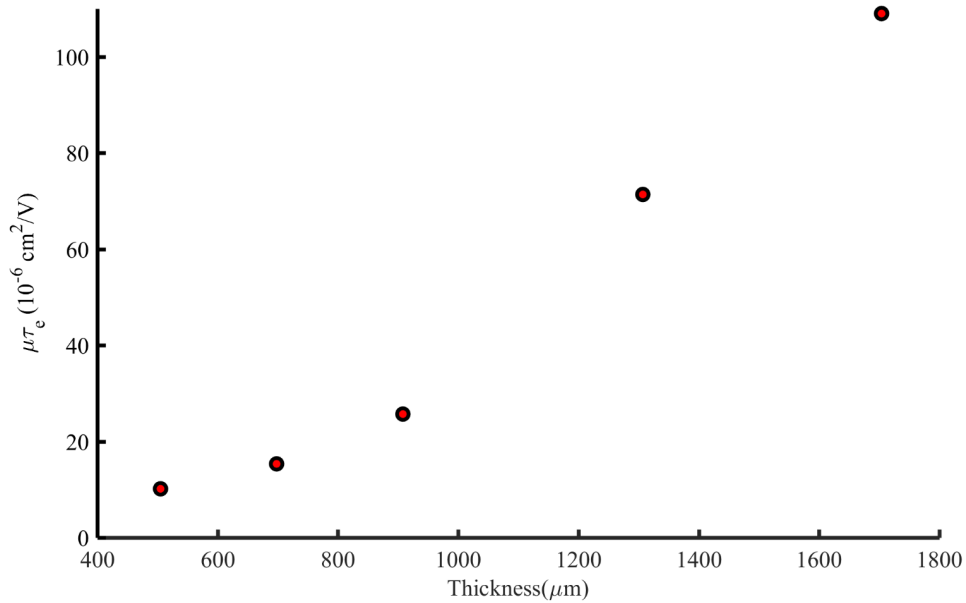
Figure 6.3: (a)Hecht fit to the peak α channel as a function of the external electric field for two thicknesses of sample L1. (b) Electron mobility-lifetime product for sample L1 as a function of sample thickness.
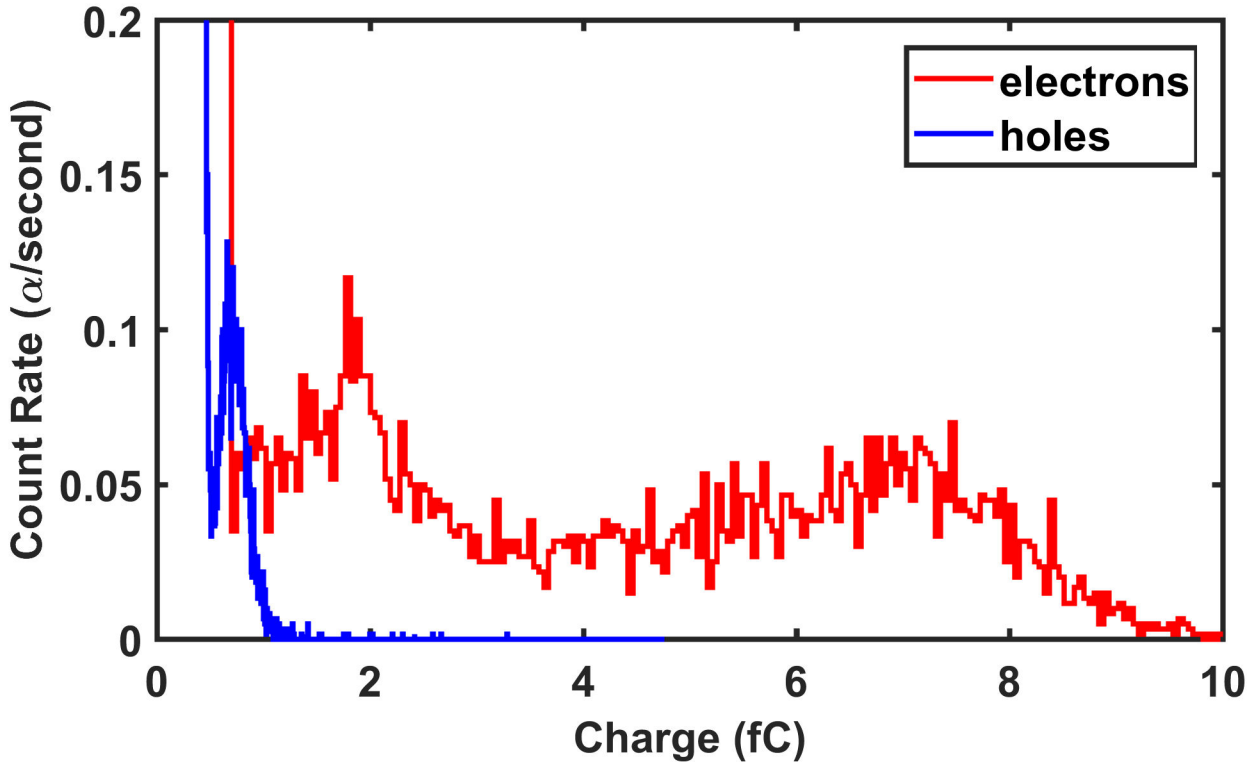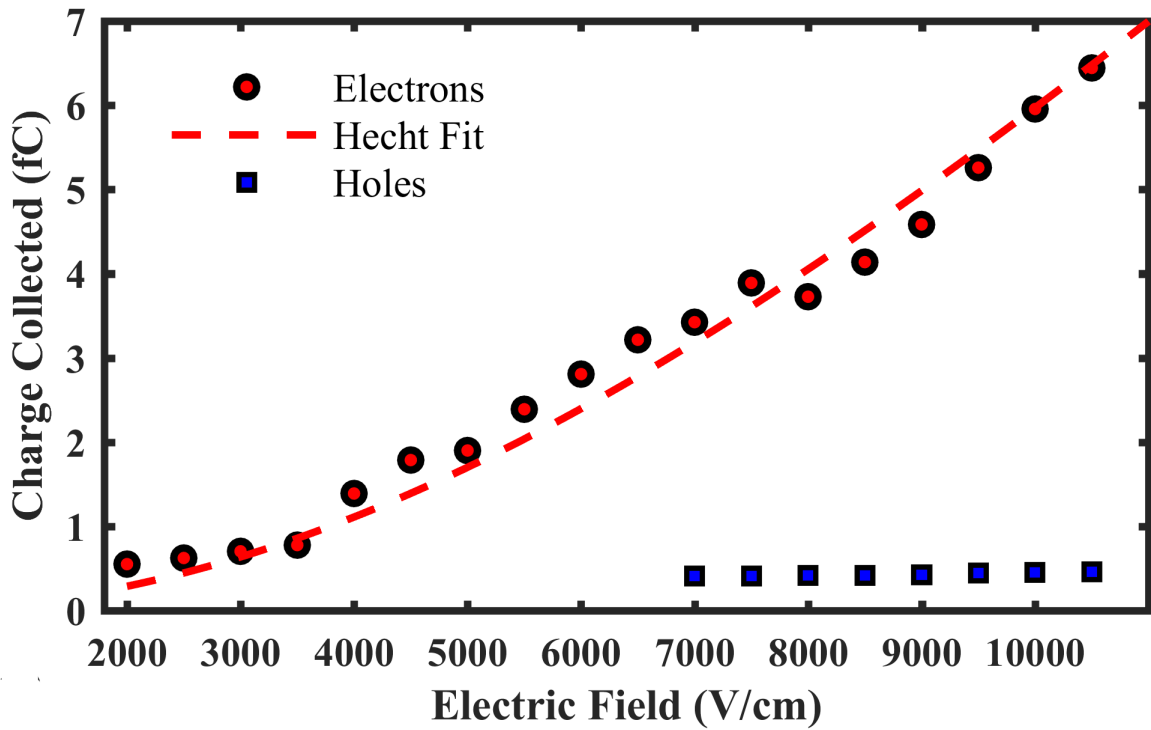
Figure 6.4: (a) Exemplar α spectra for electron and hole-only collection. (b) Hecht fit to the collected charge from α irradiation for electrons as a function of electric field. The charge collected from holes did not exhibit behavior congurent with the Hecht relation.
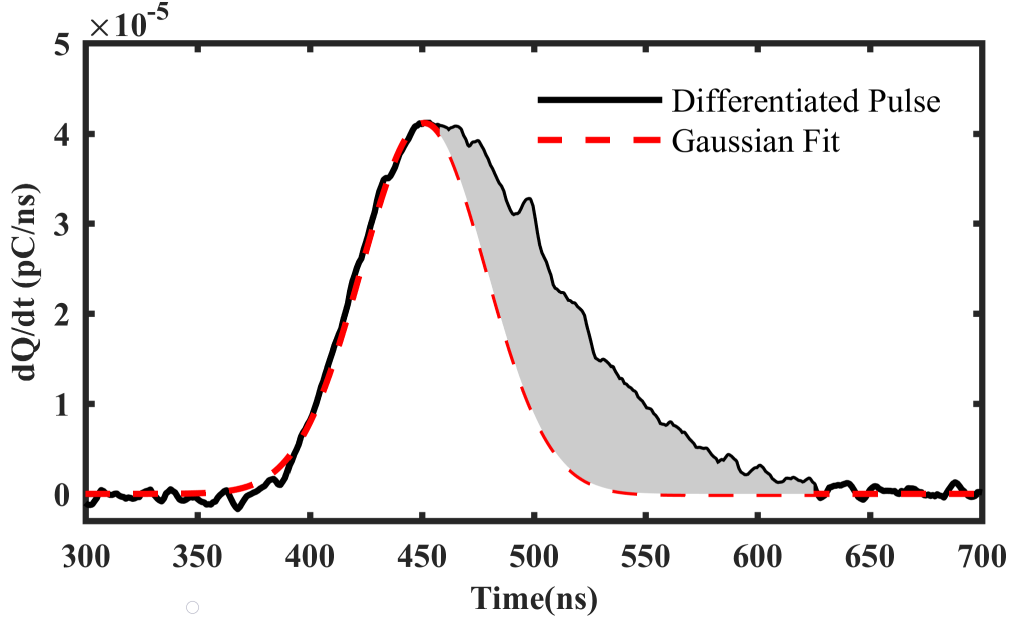
Figure 6.5: Differential charge pulse illustrating a shallow charge trap with a detrapping time within the integration time constant of the preamplifier.

on the trap depth. Equation 6.2 describes τ_D as function of the integrated signal, where V_0 is the applied bias and t_r is the transit time of the charge carriers, calculated from 10-90% of the preamplifier pulse amplitude. This analysis found that τ_D was 870 $\pm$ 40 ns [105], which is insufficient to manifest a strong impact on the observed charge collection for thin samples. However, for thicker samples, the probability for multiple trapping-escaping processes increases, which would lead to an increase in the effective detrapping time.

$$\tau_D = \tau \left[\frac{1}{V_0} \frac{dV(t)}{dt} \frac{1}{t_r} - 1 \right] \tag{6.2}$$

Mean Ionization Energy

The W-value discussed in this section is a derivative of the mean ionization energy of a semiconductor since it cannot be decouple from inherent charge losses in the system. Therefore, it is important to note that this value is less indicative of the energy to electron-hole pair conversion rate and more accurately described as an energy to collected charge conversion efficiency. For many semiconductor materials, these values are equivalent. The W-value for L1 was calculated from a linear fit to the W-value as a function of thickness. The

relationship between the mean ionization energy and detector thickness follows the intuitive relation between full charge collection and charge losses at defect sites. Figure 6.6 depicts this linear relationship, where the zero-thicknesss W-value is 380 eV/eh pair. A similar W-value of 370 eV/eh pair was observed for the irradiated L2. These values are significantly larger than the empirical formula established by Klein et al. [17], which predicts a mean ionization energy of 7.15 eV/eh pair. Large W-values are indicative of significant charge loss, effectively lowering the maximum collectible charge, which can be partially attributed to the radiative recombination mechanisms responsible for the scintillation properties of LISe. Combined with the dual scintillation/semiconduction detection results discussed in Section 4.3.2, it is clear that a majority of free carriers are trapped very close to the point of generation.

6.2.2 Polarization and Space-Charge Buildup

The preferential trapping at deep defect energies can strongly influence the charge uniformity of a semiconductor. Deep unneutralized trapping centers may result in the formation of an internal electric field that opposes the applied electric field. The so-called space-charge buildup effect reduces the effective electric field seen by the free carriers. This phenomenon results in a time-dependent detector response known as polarization. Previous α spectroscopy measurements performed by both the University of Tennessee and Fisk University cohorts have never demonstrated this effect. Post-irradiation, polarization was observed in L2 during the CCE characterization study. As shown in Figure 6.7a, the α spectral peak slowly drifted towards the noise floor while under bias. The polarization rate for L2 was estimated to 0.05 fC/min ($0.8\,\mathrm{V}/\mu\mathrm{m}$) for approximately 50 minutes at which the peak drift stabilized. Electric field and source rate were found to influence the polarization rate. Peak stabilization occurs when the trapping and detrapping rate of the deep traps responsible for this effect reach an equilibrium. Figure 6.7b depicts the α-induced polarization rate of L2 in the absence of an external field. A slight spectral shift to lower energies is observed without the influence of bias stabilizing within a few days of α exposure.

Neutron-induced polarization was studied to understand the origin of this phenomenon and gauge its effect on the long-term stability of LISe for constant operation applications. L2 was biased to 400 V ($0.8\,\mathrm{V}/\mu\mathrm{m}$) and exposed to a moderated plutonium-beryllium (PuBe)

86
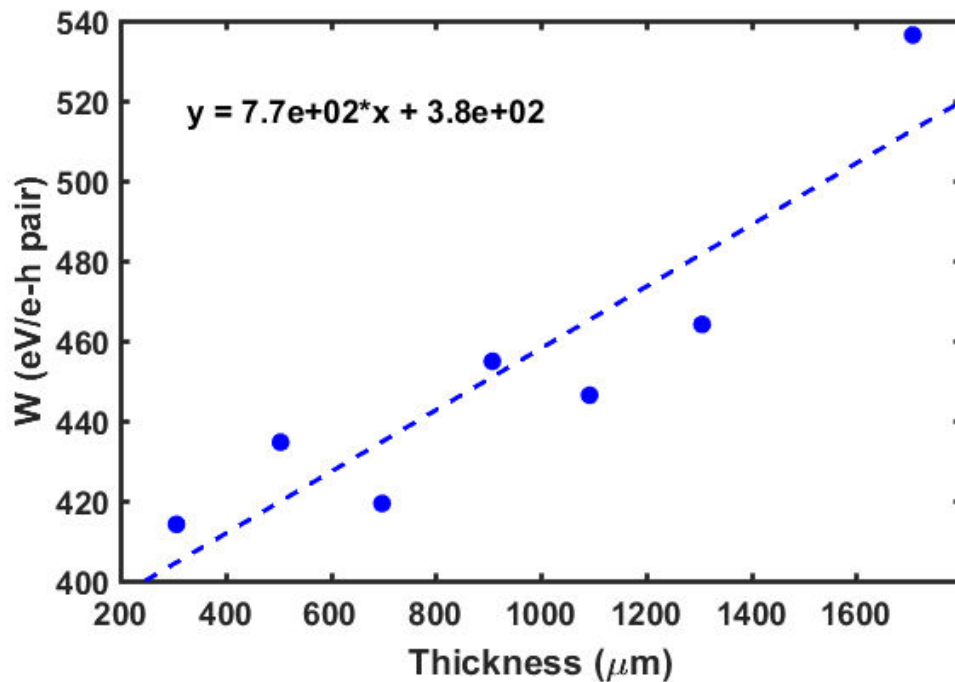
Figure 6.6: Mean ionization energy per electron hole pair, W, as a function of thickness for sample L1.
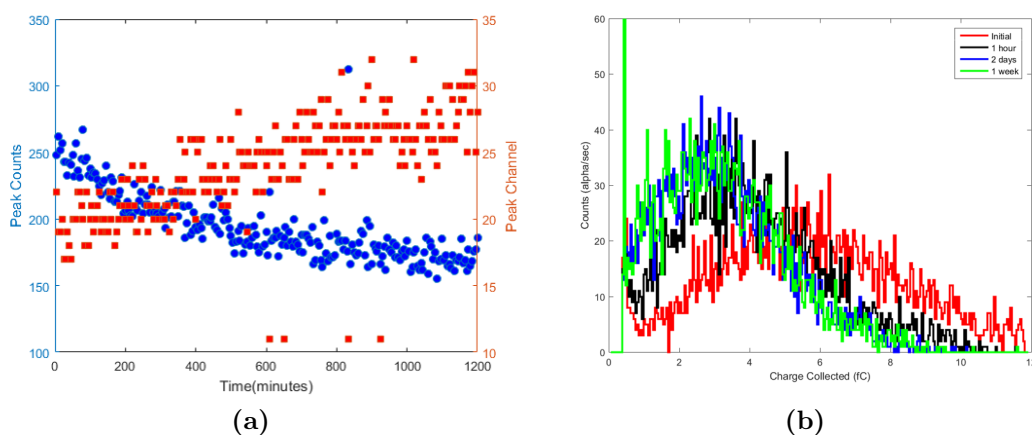
Figure 6.7: (a) Time-dependent α peak channel and count rate used to quantify the polarization rate of the irradiated sample L2. (b) Long term stability of L2 exposed to α particles for 1 hour, 2 days, and 1 week with no applied bias.

α-n source (2 Ci) for 18.5 hours while continuously recording spectra (acquisition time = 30 min). The initial and final spectra are plotted together in Figure 6.8a. The broad neutron spectrum is a result of unequal transport properties of electrons and holes in LISe as illustrated by the theoretical calculations shown in Figure 2.6. Polarization was not observed in this neutron-only field, but [115]In activation is clearly visible near the noise floor. It is important to note that the "knee" of the neutron spectrum corresponding to the 4.78 MeV Q-value of [6]Li thermal neutron capture appears at higher channels than equivalent energy α exposure. In fact, estimating W for the neutron response yields a value $(63\,\mathrm{eV/e-h})$ approximately six times smaller than the estimation from CCE measurements. Since α's are significantly less penetrating than neutrons, preferential trapping occurs near the exposed electrode, creating a space-charge build up, which screens drifting charge carriers from the applied electric field. This behavior is confirmed by mixed α-neutron field exposure, shown in Figure 6.8b, where the high energy tail of the neutron spectrum is shifted to lower channels in the presence of an α source.

Mitigation of the polarization effect is predicated on the immediate detrapping of trapped charge-carriers via some external excitation. One such technique requires exposing the crystal to sub-band gap energy photons, which excite the trapped charges from the lower energy defect state back to their respective bands. The photon energy required to reverse this process is indicative of the trap activation energy. Light-emitting diodes in the infrared, blue, and green regimes were used to further investigate the cause of polarization. Low energy infrared photons (1.32 eV) produced no change in the observed polarization rate or spectral peak shift, presumably because the deep trap responsible is more than 1.32 eV from the conduction and/or valence band. Higher energy blue photons shifted the electron and hole α peak by 44%. The most interesting result of this study is the difference in peak shift observed for green (1.98 eV) light. For electrons, the green-light induced peak shift is almost equivalent to the shift observed for blue photons. Conversely, the observed shift from 2.36 eV photons for electron-only collection is only 9% compared to 44% for hole-collection. Since electric field screening is caused by oppositely-charged, fixed charges, the deep electron trap responsible for hole-only polarization is deeper than 1.98 eV.

(a)

(b)
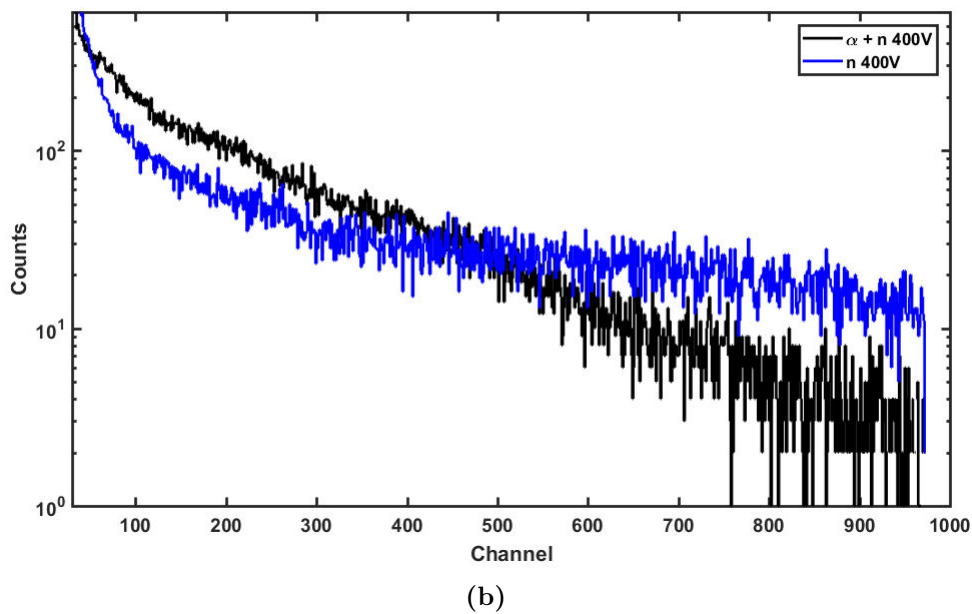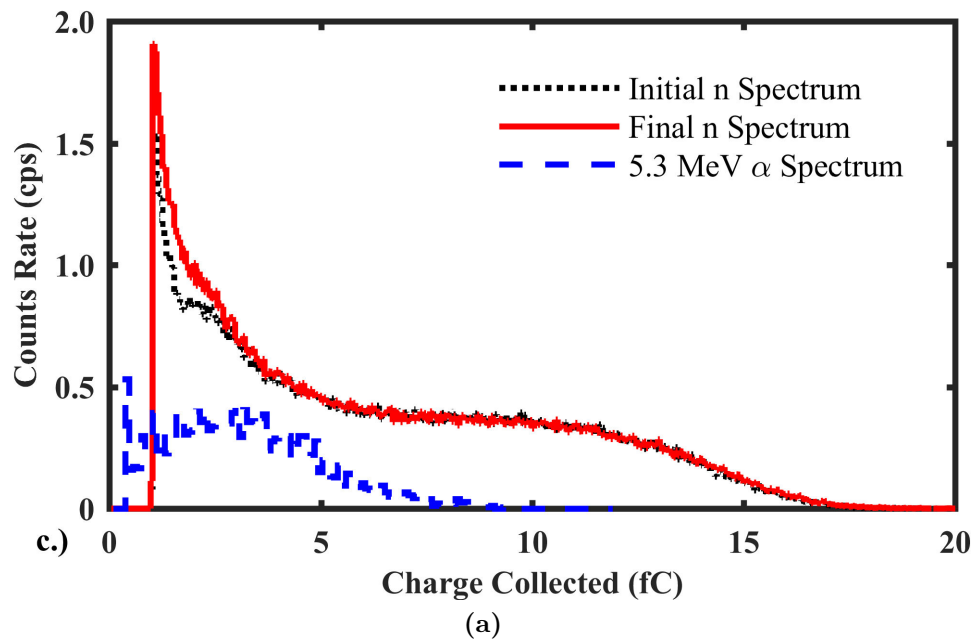
Figure 6.8: (a) Long term stability of the L2 neutron spectrum.(b)Neutron only and Mixed-field α-neutron irradiation of L2 for electrons. The α spectrum is included in (a) for reference. Note that (b) is a semi-logarithmic plot to emphasize the difference between mixed-mode and pure neutron fields.

6.2.3 Defect Characterization

To investigate the nature of neutron-induced electronic traps within L2, trap-filled limited voltage (V_{TFL}) measurements, as described in Section 5.3.2, were used to determine the electrically active trap density, N_t. Similarly, photo-induced transient current spectroscopy (PICTS) measurements, also described in Section 5.3.2, were used to determine trap activation energies, E_{Act}. For comparison, V_{TFL} measurements were conducted on L2, L3, and L4. The results, provided in Figure 6.9, indicate L2 has the highest trap density ($21 \times 10^9 \, \text{cm}^{-3}$) followed by L3 ($14 \times 10^9 \, \text{cm}^{-3}$) and then L4 ($8 \times 10^9 \, \text{cm}^{-3}$).

Previous experiments, discussed in Section 4.2.2, have determined the yellow color arises in crystals with near stoichiometric compositions [71, 76]. The unbalanced composition in the red crystals leads to deep trap sites, composed of Se vacancies, Li and In antisites, interstitials, and secondary phase inclusions [67]. Neutron irradiation of L2 resulted in at least 10^{12} lithium vacancies, not including secondary damage from the α and triton particle tracks, greatly exceeding N_t observed using V_{TFL}. The discrepancy may be attributed to room temperature annealing effects and/or the production of non-electrically active traps. Because the irradiated sample has an elevated trap density while retaining sufficient CCE to generate spectra, it can be concluded that neutron irradiation, at these levels, does not produce the detrimental traps observed in red, non-detector grade LISe.
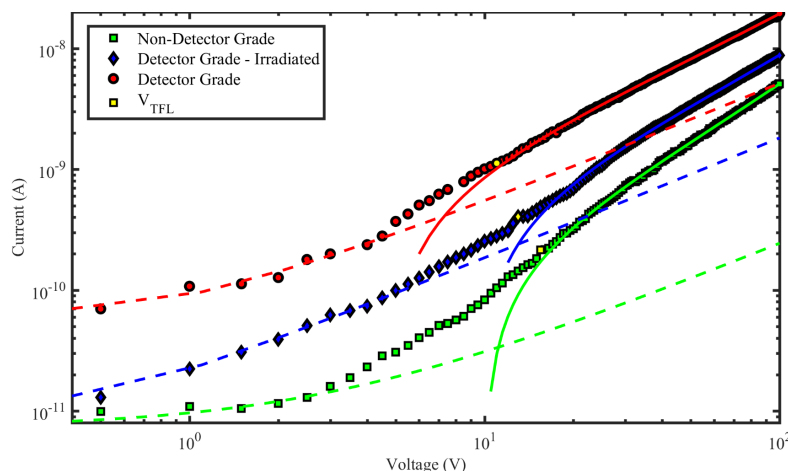
Figure 6.9: Trap-filled Limited Voltage measurements for samples L2 (blue), L3 (green), and L4 (red) used to determine the trap density. The log-log plot depicts the IV curve with fits to Ohm and Child's Law.

PICTS spectra revealed five charge carrier traps in the irradiated L2 as shown in Figure 6.10. Linear fits to the Arrhenius plot, Figure 6.10, in accordance with Equation 5.7, were used to determine the activation energy, $E_A$ct, and emission coefficient, e_0. The results are provided in Table 6.2 along with a comparison of previous PICTS results for yellow LISe from Cui et al. [67]. Of the five defect energies identified in this work, four are in close agreement with the values observed in [67]. Two defects at E_c - 0.36 eV and E_v + 0.30 eV were not observed in L2, but it can be reasonably assumed that those peaks are convoluted with the E_1 and H_1 contributing to the significant increase in uncertainty for those values when compared to E_A and H_A. The final deep trap at E_v - 0.80 eV was not identified by Cui et al., but the peak was present in their PICTS spectrum. It was excluded from their analysis due to poor fitting parameters. The tentative defect assignments from Cui et al. are supplied for reference. Additionally, Kamijoh et al. identified the deep trap H_3 as a lithium vacancy, while Cui et al. postulated that V_{LI} would exhibit energy depths near 0.1 eV. Coupled with V_{TFL}, these results suggest L2 polarization evolved from an increase in electrically-active deep trap density during neutron irradiation since no new peaks were observed in the PICTS spectra.

6.2.4   Miscellaneous Properties

Photoconductivity

In support of the use of the normalized two-gate method for PICTS analysis, the photoconductivity of LISe was investigated for white, green, and ultraviolet lights. Due to the low amplitude photocurrent within the temperature range, it was not possible to acquire PICTS spectra with the monoenergetic green and UV illumination. Figure 6.11 illustrates the photoconductivity for the dark condition and each of the light sources. The dark conductivity predictably increases exponentially with temperature due to the exponential relationship of free-carrier density as a function of temperature. All samples demonstrate strong temperature dependence of mobility for all temperatures. At low temperatures, there is an appreciable rise in conductivity, which is most pronounced for irradiated sample L2.
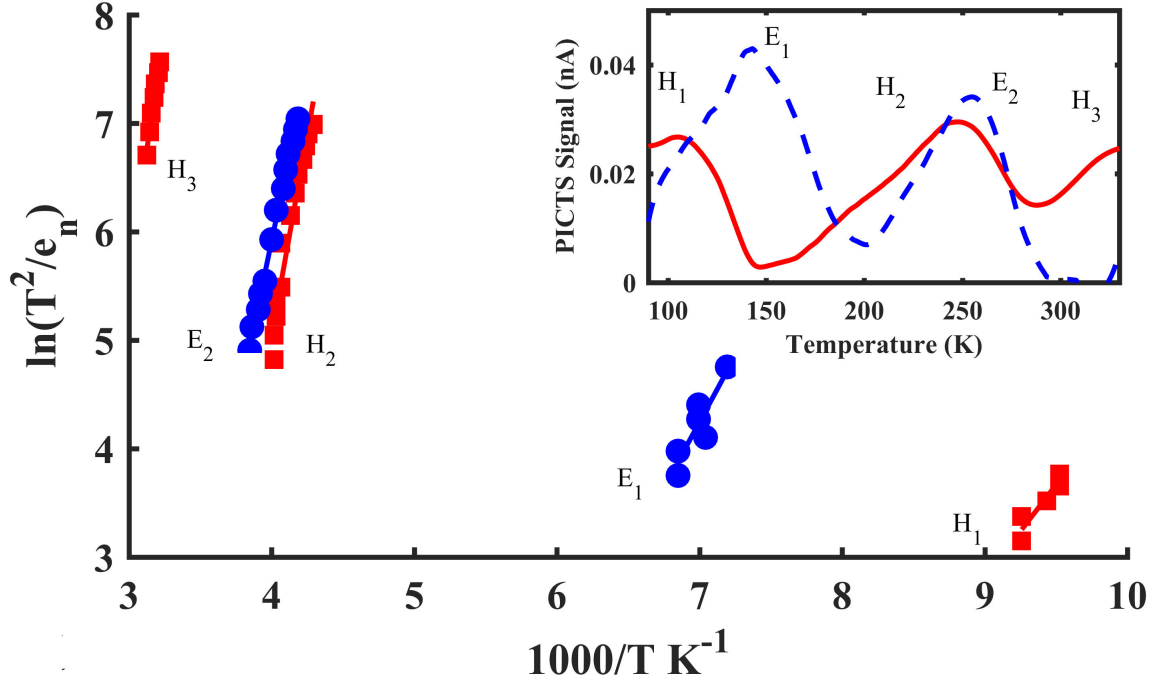
Figure 6.10: Arrhenius plots of the peak temperature as a function of the emission rate window, e_n, for five observed defect energies. (Inset) Comparison of PICTS spectra for $\pm 10\,\text{V}$ with an emission rate window of $198\,\text{s}^{-1}$ and pulse width of 100 ms.

Table 6.2: Activation energy (E_{Act}) and emission coefficient (e_0) for defect sites in L2 compared to previous PICTS measurements reported by Cui et al. [67].

			Cui et al. [67]			
Defect	$E_{Act}(eV)$	e_0 (K^{-2}s^{-1})	Defect	$E_{Act}(eV)$	e_0 (K^{-2}s^{-1})	Assignment
E$_1$*	0.21 ± 0.16	4×10^5	E$_A$	0.22 ± 0.02	5×10^5-5×10^6	$V_{Se}^{0/+}$
–	–	–	E$_B$	0.36 ± 0.03	7×10^8-7×10^{10}	$In_{Li}^{0/+}$
E$_2$	0.54 ± 0.03	2×10^8	E$_C$	0.55 ± 0.05	4×10^7-2×10^9	$In_{Li}^{+/2+}$
H$_1$*	0.15 ± 0.12	3×10^5	H$_A$	0.19 ± 0.03	3×10^5-3×10^8	$V_{In}^{0/-}$
–	–	–	H$_B$	0.30 ± 0.05	1×10^7-5×10^9	$Li_{In}^{0/-}$
H$_2$	0.64 ± 0.10	4×10^{10}	H$_C$	0.73 ± 0.03	5×10^{11}-5×10^{13}	$Li_{In}^{-/2-}$
H$_3$	0.80 ± 0.15	4×10^9	–	–	–	$V_{Li}^{0/-}$

*The shallow defects E$_1$ and H$_1$ identified in this study are likely convoluted with the additional defects identified by Cui et al., contributing to the significantly larger uncertainty for those defects.
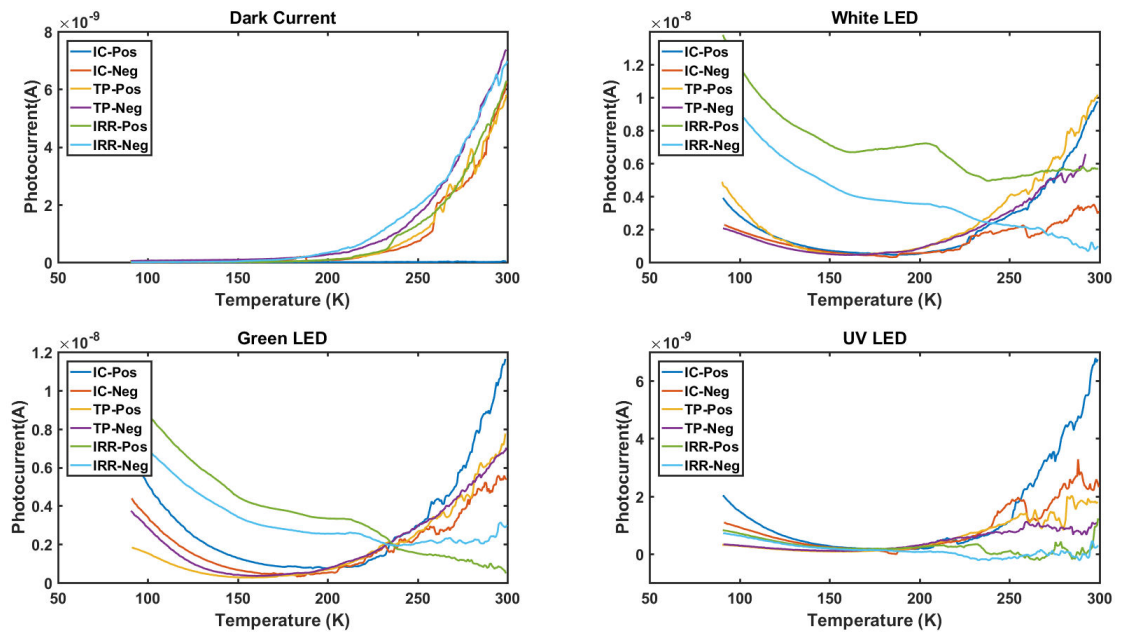
Figure 6.11: Photoconductivity measurements of samples L2 (IRR), L3 (IC), and L4 (TP) from 90 K to 330 K with a constant applied bias of ± 100 V. PC for (top left) dark current and (top right) white, (bottom left) green, and (bottom right) ultraviolet light. A strong temperature dependence is observed for charge carrier mobility.
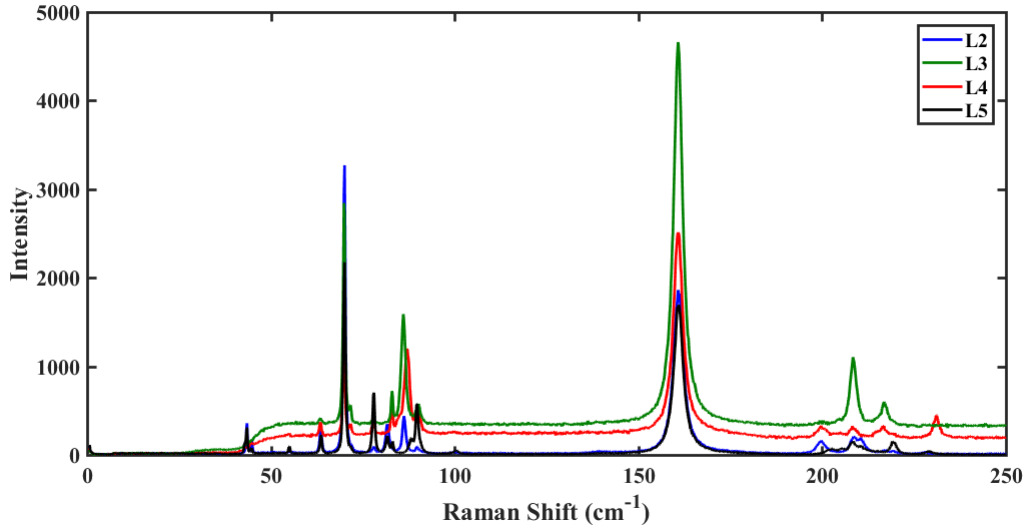
Figure 6.12: Raman spectra for samples L2, L3, L4, and scintillating L5.

Raman Spectroscopy

Raman spectra of L2, L3, L4, and L5, shown in Figure 6.12, present as many as 14 Raman active modes with the predominant peak located at $160.9\,\mathrm{cm^{-1}}$, which has been assigned to the A_1 symmetry of the Li-Se bond through the analysis of Raman spectra for $LiBC_2$ (B = In,Ga, C = Se, Te) crystals. The second largest peak at $70.6\,\mathrm{cm^{-1}}$ may be attributed to the In-Se bond [68]. As such, the two irradiated samples L2 and L5 showed an inversion of the dominant peaks indicating a Li-deficient state. Due to the significant difference in atomic mass, it is reasonable to assume that V_{Li} and Li_i generated by primary knock-on collisions comprise the majority of the increased defect density observed in L2. These results may indicate that lithium vacancies are the primary cause for reduced charge transport properties of Li-deficient red crystals and irradiation sample L2 with the caveat that In_2Se_3 precipitates dominate the properties of red crystals.

6.3 Fast Neutron Radiography

As a proof-of-principle, Timepix-coupled LISe was exposed to 9 MeV neutrons generated from a d(d,n) reaction. A highly attenuating copper block was used to demonstrate the spatial resolution via a knife-edge test. A series of 6470 frames (10 second exposure) were

<div align="center">

(a)　　　　　　　　　　　　　(b)

</div>

Figure 6.13: (a) Dark field and (b) Knife edge images for the Timepix-coupled LISe sensor for 9 MeV neutron exposure.

acquired over two days with a series of dark field (no beam) measurements taken at the beginning and end of each measurement day. The total integrated charge from the Van de Graaff accelerator was 108 mC for an average deuteron current of $3.35\,\mu$A.

A 1×1 in^2 stilbene scintillator mounted at 45° with respect to the beam axis recorded 1.21×10^8 neutrons (3750 neutrons/second) over the course of the measurement in agreement with the estimated 2×10^8 neutrons/sr MeV μC provided in Figure 5.16b. At a distance of 4.1 m from the source, the detector subtended a solid angle of 3.75×10^{-6} sr yielding an estimated neutron fluence of 3000 neutrons/second. With an expected efficiency of 2.7×10^{-5} neutron^{-1}, calculated from the numerous fast neutron interaction cross-sections with Li, In, and Se (See Appendix A), the total expected counts was estimated to be 2000 neutrons for a $528\,\mu$m detector thickness in an open beam. Figure 6.13a and 6.13b show the accumulated images for the dark field and knife-edge experiments, respectively.

Due to limitations in the aligning process, the knife edge inadvertently covered 75% (of the detector limiting neutron count rate. After masking the hot pixels, a total of 522 counts were recorded resulting in a measured efficiency of 2.68×10^{-5} neutron^{-1} in close agreement with the predicted value. Because of this and the low efficiency, the ESF was

calculated by integrating pixel columns perpendicular to the knife edge. Figure 6.14 shows the resulting one-dimensional profile. The profile for the open beam measurements at the CG-1D beamline is included for reference. Both profiles have been normalized to show the relative spatial response of an open beam for this detector. Due to time restrictions, it was not possible to collect both for fast neutrons. A combination of low count rate and knife-edge position make the calculation of MTF unreliable. The FWHM of the LSF much narrower than expected due to the sharp drop off at the detector edge. However, the spatial resolution can be estimated from the 10-90% intensity decrease observed in the ESF. Using this measure, the spatial resolution was found to be 1.55 mm from the interpolated fit to the ESF. These results are promising for future development of larger Timepix-coupled LISe detectors to increase efficiency. Significant increases in efficiency will reduce the acquisition time to achieve a desired spatial resolution while also improving contrast. Additionally, the use of the time-of-flight pickoff to reduce the contamination of lower energy neutrons can further reduce image unsharpness.
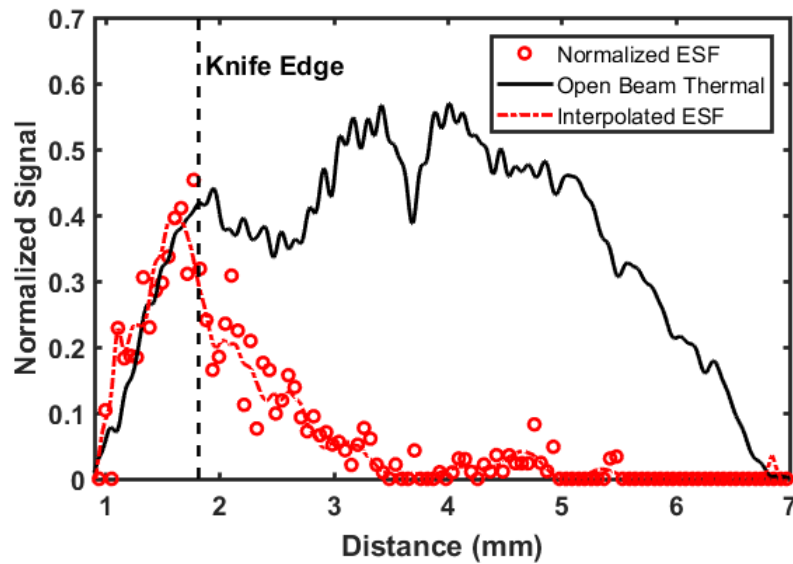
Figure 6.14: One-dimensional profiles for fast neutron knife edge and cold neutron open beam measurements showing the relative response as a function of position along the vertical axis of the detector.

Chapter 7

Conclusions

A robust mechanical contact has been identified for advanced packaging requirements such as pixelated detectors for neutron radiography. Due to its incorporation in the bulk of LISe, In provides excellent adhesion properties and IV characteristics. Additionally, In contacts were demonstrated as suitable bond pad material for ultrasonic wire bonding. The low melting point of In alleviated the need for elevated substrate temperature for gold wire bonding. Finally, a 16-channel pixel detector (LTNI) was fabricated and packaged. LTNI demonstrated a sub-pixel spatial resolution prompting further development of LISe for neutron radiography.

The fundamental charge carrier properties of LISe have been determined. This work provides novel insights into the fundamental strengths and limitations of this material as they pertain to radiation detection. LISe's performance is acutely influenced by sample preparation and care must be taken to ensure good device performance as evidenced by reduced charge transport for a mechanically thinned sample. High flux neutron irradiation of LISe generated an anomalous detector performance. Investigation of this phenomenon has shown that charge carrier traps created in the bulk of the semiconductor increases the charge collection efficiency of LISe. Adversely, a polarizing effect and reduced $\mu\tau_e$ are observed for this material. As a neutron detector, there is no observed degradation in the neutron spectrum from high flux irradiation. The irradiated crystal also demonstrated the unique ability to produce α spectra from hole collection. Polarization in LISe reduces the charge collected for alpha exposures as a function of time under bias. Further, rate of polarization is dependent on applied bias and (weakly) source rate. The improved

charge collection efficiency for both holes and electrons despite reduced transport properties could be attributed to the distribution of non-radiative and radiative traps post-irradiation. These results could provide insight behind the mechanism that creates the semiconductor-grade/scintillation-grade exclusivity for this material. Further studies are required to identify the dominant scintillation mechanism. V_{TFL} measurements showed an elevated trap density in the irradiated sample with reference to the poorly semiconducting non-detector grade sample demonstrating that trap type is a significant influence on the performance of the detector. The types and emission rates of the traps probed via PICTS are consistent with those previously observed for this material up 330 K. Finally, the observed polarization can be reversed by exposing the material to photons with sufficient energy, but no effect is seen for 1.32 eV photons hinting at the possibility of a very deep level near the middle of the band gap. Raman spectra demonstrated a correlation between irradiation and the predominance of the relative ratio of Li-Se and In-Se Raman vibrational modes indicating a Li-deficient state. Further research is required to develop a full model of the defect distribution in LISe and their influence on semiconduction and scintillation.

Finally, a knife-edge resolution test was performed on a Timepix-coupled LISe detector for monoenergetic fast neutron irradiation at Edwards Accelerator Laboratory. A series of 6470 frames were recorded at a exposure time of 5 seconds. The integrated image was compressed into a single pixel row to compensate for detection efficiency and flux limitations. The modulation transfer function was calculated to determine the spatial resolution. For 9 MeV quasi-monoenergetic neutrons, a spatial resolution of 1.55 mm was found. Further improvements in the detector fabrication process and increase in detector thickness are recommended to meet the requirements of fast neutron radiography. In conclusion, LISe is a promising material for neutron detection and imaging applications exhibiting excellent detection efficiency and sufficient detector performance.

Bibliography

[1] P. J. Van Heerden, *The crystal counter: a new instrument in nuclear physics...* Nv Noordhollandsche uitgevers maatschappij, 1945. 3

[2] P. Van Heerden, "A new apparatus in nuclear physics for the investigation of β-and γ-rays. part i," *Physica*, vol. 16, no. 6, pp. 505–516, 1950.

[3] P. Van Heerden and J. Milatz, "A new apparatus in nuclear physics for the investigation of β-and γ-rays. part ii," *Physica*, vol. 16, no. 6, pp. 517–527, 1950. 3

[4] E. Rutherford and H. Geiger, "An electrical method of counting the number of α - particles from radio-active substances," *Proceedings of the Royal Society of London Series A*, vol. 81, pp. 141–161, Aug. 1908. 3

[5] B. Gudden and R. Pohl, "Das quantenäquivalent bei der lichtelektrischen leitung," *Zeitschrift fur Physik*, vol. 17, pp. 331–346, Dec. 1923. 3

[6] W. Lehfeldt, "Über die elektrische leitfähigkeit von einkristallen," *Zeitschrift fur Physik*, vol. 85, pp. 717–726, Nov. 1933.

[7] R. Frerichs and R. Warminsky, "Die messung von β- und γ-strahlen durch inneren photoeffekt in kristallphosphoren," *Naturwissenschaften*, vol. 33, pp. 251–251, Oct. 1946. 3

[8] R. Hofstadter, J. Milton, and S. Ridgway, "Behavior of silver chloride crystal counters," *Physical Review*, vol. 72, no. 10, p. 977, 1947. 3

[9] R. Hofstadter, "Thallium halide crystal counter," *Physical Review*, vol. 72, no. 11, p. 1120, 1947.

[10] R. Hofstadter, "Crystal counters," *Proceedings of the IRE*, vol. 38, no. 7, pp. 726–740, 1950.

[11] W. Jentschke, "The crystal counter," *Physical Review*, vol. 73, no. 1, p. 77, 1948. 3

[12] W. M. Gibson, G. L. Miller, and P. F. Donovan, "Semiconductor particle spectrometers," in *Alpha-, Beta- and Gamma-ray Spectroscopy* (K. Siegbahn, ed.), p. 345, 1965. 3

[13] S. S. Friedland, J. W. Mayer, J. M. Denney, and F. Keywell, "Room temperature operated p-n junctions as charged particle detectors," *Review of Scientific Instruments*, vol. 31, pp. 74–75, Jan. 1960.

[14] N. A. Baily, R. J. Grainger, and J. W. Mayer, "Capabilities of lithium drifted p-i-n junction detectors when used for gamma-ray spectroscopy," *Review of Scientific Instruments*, vol. 32, pp. 865–866, July 1961.

[15] J. W. Mayer, "Use of ion implantation techniques to fabricate semiconductor nuclear particle detectors," *Nuclear Instruments and Methods*, vol. 63, pp. 141–151, 1968. 3

[16] A. Owens, *Compound Semiconductor Radiation Detectors*. Taylor & Francis, 2012. xi, 4, 6, 8, 10, 13, 20

[17] C. A. Klein, "Bandgap dependence and related features of radiation ionization energies in semiconductors," *Journal of Applied Physics*, vol. 39, pp. 2029–2038, Mar. 1968. 4, 5, 86

[18] P. Geng, W. Li, X. Zhang, X. Zhang, Y. Deng, and H. Kou, "A novel theoretical model for the temperature dependence of band gap energy in semiconductors," *Journal of Physics D Applied Physics*, vol. 50, p. 40LT02, Oct. 2017.

[19] M. L. Cohen and T. K. Bergstresser, "Band structures and pseudopotential form factors for fourteen semiconductors of the diamond and zinc-blende structures," *Physical Review*, vol. 141, pp. 789–796, Jan. 1966. 4

[20] L. A. Dubridge, "Theory of the energy distribution of photoelectrons," *Physical Review*, vol. 43, pp. 727–741, May 1933. 5

[21] J. McDougall and E. C. Stoner, "The computation of fermi-dirac functions," *Philosophical Transactions of the Royal Society of London Series A*, vol. 237, pp. 67–104, Feb. 1938. 5

[22] D. A. Neaman, *Semiconductor Physics and Devices: Basic Principles*. McGraw-Hill, 4th ed., 2003. 6

[23] W. Shockley, "Currents to conductors induced by a moving point charge," *Journal of applied physics*, vol. 9, no. 10, pp. 635–636, 1938. 6, 11, 53, 126

[24] S. Ramo, "Currents induced by electron motion," *Proceedings of the IRE*, vol. 27, no. 9, pp. 584–585, 1939. 6, 11, 53, 126

[25] M. A. Lampert, "Simplified theory of space-charge-limited currents in an insulator with traps," *Physical Review*, vol. 103, no. 6, p. 1648, 1956. 6, 8, 63

[26] G. F. Knoll, *Radiation Detection and Measurement.* John Wiley& Sons, Inc., 4th ed., 2010. 8, 9, 10, 18, 19, 21, 30

[27] Z. He, "Review of the shockley–ramo theorem and its application in semiconductor gamma-ray detectors," *Nuclear Instruments and Methods in Physics Research Section A: Accelerators, Spectrometers, Detectors and Associated Equipment*, vol. 463, no. 1, pp. 250–267, 2001. 9, 13, 126, 127

[28] J. Tersoff, "Theory of semiconductor heterojunctions: The role of quantum dipoles," *Physical Review B*, vol. 30, pp. 4874–4877, Oct. 1984. 10

[29] D. A. Neamen, "Semiconductor device physics: Basic principles," 2012. xi, 10, 12

[30] W. Shockley, "The theory of p-n junctions in semiconductors and p-n junction transistors," *Bell Labs Technical Journal*, vol. 28, no. 3, pp. 435–489, 1949. 10

[31] G. G. Harman, *Wire bonding in microelectronics.* McGraw-Hill, 2010. 10

[32] Y. Takahashi and M. Inoue, "Numerical study of wire bondinganalysis of interfacial deformation between wire and pad," *Journal of Electronic Packaging*, vol. 124, no. 1, pp. 27–36, 2002.

[33] G. G. Harman, *Reliability and Yield problems of Wire Bonding in Microelectronics: the application of materials and interface science.* na, 1991. 10

[34] C. Jacoboni, C. Canali, G. Ottaviani, and A. Alberigi Quaranta, "A review of some charge transport properties of silicon," *Solid State Electronics*, vol. 20, pp. 77–89, Feb. 1977. 11

[35] J. E. Turner and C. A. Kelsey, "Atoms, radiation and radiation protection," *Physics Today*, vol. 49, p. 68, Jan. 1996. 18

[36] J. J. Duderstadt, L. J. Hamilton, S. Moorthy, and C. C. Scott, "Nuclear reactor analysis by james j. duderstadt and louis j. hamilton," *IEEE Transactions on Nuclear Science*, vol. 24, pp. 1983–1983, June 1977. 18

[37] T. A. Wellington, B. A. Palles, J. A. Mullens, J. T. Mihalczo, D. E. Archer, T. Thompson, C. L. Britton, N. D. B. Ezell, M. N. Ericson, E. Farquhar, R. Lind, and J. Carter, "Recent fast neutron imaging measurements with the fieldable nuclear materials identification system[1]," *Physics Procedia*, vol. 66, pp. 432–438, 2015. 19

[38] J. T. Mihalczo, J. A. Mullens, J. K. Mattingly, and T. E. Valentine, "Physical description of nuclear materials identification system (nmis) signatures," *Nuclear Instruments and Methods in Physics Research A*, vol. 450, pp. 531–555, Aug. 2000. 19

[39] W. A. Peters, S. Ilyushkin, M. Madurga, C. Matei, S. V. Paulauskas, R. K. Grzywacz, D. W. Bardayan, C. R. Brune, J. Allen, J. M. Allen, Z. Bergstrom, J. Blackmon, N. T. Brewer, J. A. Cizewski, P. Copp, M. E. Howard, R. Ikeyama, R. L. Kozub, B. Manning, T. N. Massey, M. Matos, E. Merino, P. D. O'Malley, F. Raiola, C. S. Reingold, F. Sarazin, I. Spassova, S. Taylor, and D. Walter, "Performance of the versatile array of neutron detectors at low energy (vandle)," *Nuclear Instruments and Methods in Physics Research A*, vol. 836, pp. 122–133, Nov. 2016. 19

[40] D. S. McGregor, M. D. Hammig, Y. H. Yang, H. K. Gersch, and R. T. Klann, "Design considerations for thin film coated semiconductor thermal neutron detector 1: basics regarding alpha particle emitting neutron reactive films," *Nuclear Instruments and Methods in Physics Research Section A: Accelerators, Spectrometers, Detectors and Associated Equipment*, vol. 500, pp. 272–308, 2003. xii, 19, 20, 21, 23, 24

[41] I. S. Anderson, R. L. McGreevy, and H. Z. Bilheux, *Neutron Imaging and Applications.* New York, NY: Springer, 2009. 19, 31

[42] E. Tupitsyn, P. Bhattacharya, E. Rowe, L. Matei, Y. Cui, V. Buliga, M. Groza, B. Wiggins, A. Burger, and A. Stowe, "Lithium containing chalcogenide single crystals for neutron detection," *Journal of Crystal Growth*, vol. 393, 2014. xii, 21, 36, 41

[43] J. Jakubek, T. Holy, E. Lehmann, S. Pospisil, J. Uher, J. Vacik, and D. Vavrik, "Spatial resolution of Medipix-2 device as neutron pixel detector," *Nuclear Instruments and Methods in Physics Research Section A: Accelerators, Spectrometers, Detectors and Associated Equipment*, vol. 546, pp. 164–169, 2005. xii, 22, 25, 66

[44] T. C. Unruh, S. L. Bellinger, D. E. Huddleston, W. J. McNeil, E. Patterson, T. J. Sobering, and D. S. McGregor, "Design and operation of a 2-D thin-film semiconductor neutron detector array for use as a beamport monitor," *Nuclear Instruments and Methods in Physics Research Section A: Accelerators, Spectrometers, Detectors and Associated Equipment*, vol. 604, no. 1, pp. 150–153, 2009. 24

[45] J. Uher, C. Frojdh, J. Jakubek, C. Kenney, Z. Kohout, V. Linhart, S. Parker, S. Petersson, S. Pospisil, and G. Thungstrom, "Highly sensitive silicon detectors of thermal neutrons," in *Nuclear Science Symposium Conference Record, 2006. Institute of Electrical and Electronics Engineers*, vol. 3, pp. 1346–1348, 2006. xii, 25, 26

[46] J. Uher, C. Frojdh, J. Jakubek, C. Kenney, Z. Kohout, V. Linhart, S. Parker, S. Petersson, S. Pospisil, and G. Thungstrom, "Characterization of 3D thermal neutron semiconductor detectors," *Nuclear Instruments and Methods in Physics Research Section A: Accelerators, Spectrometers, Detectors and Associated Equipment*, vol. 576, no. 1, pp. 32–37, 2007. 25

[47] D. S. McGregor, W. J. McNeil, S. L. Bellinger, T. C. Unruh, and J. K. Shultis, "Microstructured semiconductor neutron detectors," *Nuclear Instruments and Methods in Physics Research Section A: Accelerators, Spectrometers, Detectors and Associated Equipment*, vol. 608, no. 1, pp. 125–131, 2009. xii, 27, 28

[48] S. L. Bellinger, R. Fronk, W. McNeil, T. Sobering, and D. S. McGregor, "Improved High Efficiency Stacked Microstructured Neutron Detectors Backfilled With

Nanoparticle 6LiF," *Institute of Electrical and Electronics Engineers Transactions of Nuclear Science*, vol. 59, no. 1, pp. 167–173, 2012. xii, 27, 28

[49] G. Fehrenbacher, J. Biersack, E. Cordes, and W. Wahl, "Response of converter semiconductor detectors on neutron radiation," *Radiation Measurements*, vol. 28, pp. 429–434, 1997. 31

[50] A. Simpson, S. Jones, M. Clapham, and S. McElhaney, "A review of neutron detection technology alternatives to helium-3 for safeguards applications," in *INMM 52nd Annual Meeting*, vol. 8, 2011. 31

[51] R. Satija, D. L. Jacobson, M. Arif, and S. Werner, "In situ neutron imaging technique for evaluation of water management systems in operating pem fuel cells," *Journal of Power Sources*, vol. 129, no. 2, pp. 238–245, 2004. 31

[52] J. M. Hall, S. Asztalos, P. Biltoft, J. Church, M.-A. Descalle, T. Luu, D. Manatt, G. Mauger, E. Norman, D. Petersen, *et al.*, "The nuclear car wash: Neutron interrogation of cargo containers to detect hidden snm," *Nuclear Instruments and Methods in Physics Research Section B: Beam Interactions with Materials and Atoms*, vol. 261, no. 1-2, pp. 337–340, 2007. 31

[53] R. Nelson, J. Hunter, R. Schirato, S. Vogel, A. Swift, T. Ickes, B. Ward, A. Losko, and A. Tremsin, "Neutron imaging developments at lansce," in *APS Division of Nuclear Physics Meeting Abstracts*, p. DH.003, Oct. 2015.

[54] A. Swift, R. Schirato, E. McKigney, J. Hunter, and B. Temple, "Time gating for energy selection and scatter rejection: High-energy pulsed neutron imaging at lansce," in *Radiation Detectors: Systems and Applications XVI*, vol. 9595 of *SPIE Proceedings*, p. 95950J, Sept. 2015. 31

[55] M. R. Hawkesworth and J. Walker, "Review: Radiography with neutrons," *Journal of Materials Science*, vol. 4, pp. 817–835, Sept. 1969. xii, 32, 33

[56] P. Trtik and E. H. Lehmann, "Isotopically-enriched gadolinium-157 oxysulfide scintillator screens for the high-resolution neutron imaging," *Nuclear Instruments and*

Methods in Physics Research Section A: Accelerators, Spectrometers, Detectors and Associated Equipment, vol. 788, pp. 67–70, 2015. 34

[57] W. Yang, T. Bin, H. Heyong, L. Bin, T. Ke, S. Yong, Y. Wei, and C. Chao, "The study of zinc sulphide scintillator for fast neutron radiography," *Physics Procedia*, vol. 43, pp. 205–215, 2013. 34

[58] T. Negran, H. Kasper, and A. Glass, "Pyroelectric and electrooptic effects in liins2 and liinse2," *Materials Research Bulletin*, vol. 8, no. 6, pp. 743–748, 1973. 35

[59] Z. W. Bell, D. Carpenter, S. Cristy, V. Lamberti, A. Burger, B. F. Woodfield, T. Niedermayr, I. Dragos Hau, S. E. Labov, S. Friedrich, *et al.*, "Neutron detection with cryogenics and semiconductors," *physica status solidi (c)*, vol. 2, no. 5, pp. 1592–1605, 2005. 35, 82

[60] E. Tupitsyn, P. Bhattacharya, E. Rowe, L. Matei, M. Groza, B. Wiggins, A. Burger, and A. Stowe, "Single crystal of LiInSe2 semiconductor for neutron detector," *Applied Physics Letters*, vol. 101, no. 20, p. 202101, 2012. 35, 36, 39, 46

[61] L. Isaenko, A. Yelisseyev, S. Lobanov, V. Petrov, F. Rotermund, G. Slekys, and J.-J. Zondy, "Liinse$_2$: A biaxial ternary chalcogenide crystal for nonlinear optical applications in the midinfrared," *Journal of Applied Physics*, vol. 91, pp. 9475–9480, June 2002. 35, 36, 37

[62] T. Kamijoh and K. Kuriyama, "Single crystal growth and characterization of liinse $_2$," *Journal of Crystal Growth*, vol. 51, pp. 6–10, Jan. 1981. 35, 39

[63] A. C. Stowe, B. Wiggins, P. Bhattacharya, E. Tupitsyn, M. Groza, L. Matei, S. Keivan, E. H. Herrera, E. D. Lukosi, and A. Burger, "Improving neutron detection in semiconducting 6LiInSe2 crystals," in *SPIE* (A. Burger, L. Franks, R. B. James, and M. Fiederle, eds.), vol. 9213 of *Hard X-Ray, Gamma-Ray, and Neutron Detector Physics XVI*, p. 92130B, SPIE. xiii, 36, 41, 42

[64] T. Ma, C. Zhu, Z. Lei, C. Yang, L. Sun, and H. Zhang, "Growth and characterization of liinse$_2$ single crystals," *Journal of Crystal Growth*, vol. 415, pp. 132–138, Apr. 2015. 37, 39

[65] T. Ma, H. Zhang, J. Zhang, Z. Lei, C. Zhu, and C. Yang, "Preparation and optical properties of liinse$_2$ crystals," *Journal of Crystal Growth*, vol. 448, pp. 122–127, Aug. 2016.

[66] L. Dai, C. Tan, Z. Yan, and Y. Xu, "Investigations on growth and property of mid-infrared lithium selenoindate single crystals," *Modern Physics Letters B*, vol. 30, p. 1650290, Aug. 2016.

[67] Y. Cui, P. Bhattacharya, V. Buliga, E. Tupitsyn, E. Rowe, B. Wiggins, D. Johnstone, A. Stowe, and A. Burger, "Defects in 6LiInSe2 neutron detector investigated by photo-induced current transient spectroscopy and photoluminescence," *Applied Physics Letters*, vol. 103, no. 9, p. 092104, 2013. x, xiii, 39, 40, 60, 90, 91, 92

[68] A. Eifler, V. Riede, J. Brückner, S. Weise, V. Krämer, G. Lippold, W. Schmitz, K. Bente, and W. Grill, "Band gap energies and lattice vibrations of the lithium ternary compounds liinse2, liins2, ligase2 and ligas2," *Japanese Journal of Applied Physics*, vol. 39, no. S1, p. 279, 2000. 66, 94

[69] P. Vijayakumar, M. Magesh, A. Arunkumar, G. Anandha Babu, P. Ramasamy, and S. Abhaya, "Investigations on synthesis, growth, electrical and defect studies of lithium selenoindate single crystals," *Journal of Crystal Growth*, vol. 388, pp. 17–21, Feb. 2014. 37, 39

[70] V. Palanimuthu, M. Murugesan, A. Alagesan, A. B. Govindan, and R. Perumalsamy, "Investigations on synthesis, growth and physical characterizations of lithium selenoindate single crystal,"

[71] V. Petrov, J.-J. Zondy, O. Bidault, L. Isaenko, V. Vedenyapin, A. Yelisseyev, W. Chen, A. Tyazhev, S. Lobanov, G. Marchev, and D. Kolker, "Optical, thermal, electrical,

damage, and phase-matching properties of lithium selenoindate," *Journal of the Optical Society of America B Optical Physics*, vol. 27, p. 1902, Aug. 2010. 39, 90

[72] J.-J. Zondy, V. Petrov, A. Yelisseyev, S. Lobanov, and L. Isaenko, *Orthorhombic Crystals of Lithium Thioindate and Selenoindate for Nonlinear Optics in the Mid-IR*, pp. 67–104. 2008. 39

[73] B. Wiggins, E. Tupitsyn, P. Bhattacharya, E. Rowe, E. Lukosi, O. Chvala, A. Burger, and A. Stowe, "Investigation of non-uniformity and inclusions in 6LiInSe2 utilizing laser induced breakdown spectroscopy (LIBS)," in *SPIE* (M. Fiederle, A. Burger, L. Franks, and R. B. James, eds.), vol. 8852, p. 88520M, SPIE. 37

[74] B. Lorenz, "High pressure raman investigation of liinse2 in the β-nafeo2 structure," *Journal of Physics and Chemistry of Solids*, vol. 58, no. 3, pp. 399–402, 1997. xv, 37, 65, 66

[75] T. Omata, H. Nagatani, I. Suzuki, and M. Kita, "Wurtzite-derived ternary i–iii–o2 semiconductors," *Science and technology of advanced materials*, vol. 16, no. 2, p. 024902, 2015. xiii, 37, 38

[76] S. Weise, *Züchtung und Charakterisierung von Kristallen im System Li2Se-In2Se3*. Shaker Verlag GmbH, 2002. 37, 39, 90

[77] I. G. Vasilyeva, A. A. Pochtar, and L. I. Isaenko, "Origin of the solid solution in the liinse$_2$-in$_2$se$_3$ system," *Journal of Solid State Chemistry France*, vol. 220, pp. 91–96, Dec. 2014. 37

[78] L. Isaenko, A. Yelisseyev, S. Lobanov, P. Krinitsin, and M. Molokeev, "Structure and optical properties of li2ga2ges6 nonlinear crystal," *Optical Materials*, vol. 47, pp. 413–419, 2015. 37

[79] V. Badikov, V. Chizhikov, V. Efimenko, T. Efimenko, V. Panyutin, G. Shevyrdyaeva, and S. Scherbakov, "Optical properties of lithium indium selenide," *Optical Materials*, vol. 23, no. 3-4, pp. 575–581, 2003. 37

[80] C.-G. Ma and M. G. Brik, "First principles studies of the structural, electronic and optical properties of liinse$_2$ and liinte$_2$ chalcopyrite crystals," *Solid State Communications*, vol. 203, pp. 69–74, Feb. 2015. 37

[81] G. Li, J. K. C. Abbott, J. D. Brasfield, P. Liu, A. Dale, G. Duscher, P. D. Rack, and C. S. Feigerle, "Structure characterization and strain relief analysis in cvd growth of boron phosphide on silicon carbide," *Applied Surface Science*, vol. 327, pp. 7–12, 2015. 39

[82] H. J. Beister, S. Ves, W. Hönle, K. Syassen, and G. Kühn, "Structural phase transitions and optical absorption of liinse$_2$ under pressure," *Physical Review B*, vol. 43, pp. 9635–9642, Apr. 1991. 39

[83] T. Kamijoh, T. Nozaki, and K. Kuriyama, "A photoluminescence study on lithium ternary compounds," *Nuovo Cimento D Serie*, vol. 2, pp. 2029–2033, Nov. 1983.

[84] Y. Li, W. Fan, H. Sun, X. Cheng, P. Li, and X. Zhao, "Computational insight into the effect of monovalent cations on the electronic, optical, and lattice dynamic properties of xinse$_2$ (x = cu, ag, li)," *Journal of Applied Physics*, vol. 109, pp. 113535–113535–10, June 2011.

[85] B. Wiggins, M. Groza, E. Tupitsyn, E. D. Lukosi, K. Stassun, A. Burger, and A. C. Stowe, "Scintillation properties of semiconducting 6LiInSe2 crystals to ionizing radiation," *Nuclear Instruments and Methods in Physics Research Section A*, 2016. 39, 41, 42

[86] E. D. Lukosi, "Lithium Indium Diselenide Sensor for Neutron Transmission Imaging," in *SPIE* (E. H. Herrera, A. C. Stowe, B. Wiggins, and A. Burger, eds.), p. 15, PSND 2014 Workshop, 2014. 41

[87] E. Lukosi, E. Herrera, A. C. Stowe, R. Milburn, D. Richardson, B. Wiggins, A. Burger, O. Chvala, L. Santodonato, and H. Bilheux, "Investigation of a lithium indium diselenide detector for neutron transmission imaging," in *Hard X-Ray, Gamma-Ray,*

and *Neutron Detector Physics XVI*, vol. 9213 of *SPIE Proceedings*, p. 92130D, Sept. 2014.

[88] E. Lukosi, O. Chvala, and A. Stowe, "Response functions of semiconducting lithium indium diselenide," *Nuclear Instruments and Methods in Physics Research Section A: Accelerators, Spectrometers, Detectors and Associated Equipment*, vol. 822, pp. 9–14, 2016. xiii, 42, 44, 45

[89] Z. W. Bell, A. Burger, L. Matei, M. Groza, A. Stowe, J. Tower, A. Kargar, and H. Hong, "Neutron detection with liinse2," in *SPIE*, vol. 9593, pp. 95930D–95930D–13, 2014. xiii, 42

[90] E. Herrera, D. Hamm, B. Wiggins, R. Milburn, A. Burger, H. Bilheux, L. Santodonato, O. Chvala, A. Stowe, and E. Lukosi, "Lise pixel detector for neutron imaging," *Nuclear Instruments and Methods in Physics Research A*, vol. 833, pp. 142–148, Oct. 2016. 41

[91] E. D. Lukosi, D. Richardson, A. C. Stowe, B. Wiggins, and A. Burger, eds., *Neutron Detection and Imaging Using Pixelated LiInSe2 Semiconducting Detector*, ANS RPSD, 2016. 43, 48

[92] E. Lukosi, E. Herrera, D. Hamm, K.-M. Lee, B. Wiggins, P. Trtik, D. Penumadu, S. Young, L. Santodonato, H. Bilheux, A. Burger, L. Matei, and A. C. Stowe, "Lithium indium diselenide: A new scintillator for neutron imaging," *Nuclear Instruments and Methods in Physics Research A*, vol. 830, pp. 140–149, Sept. 2016.

[93] E. D. Lukosi, E. H. Herrera, D. S. Hamm, A. Burger, and A. C. Stowe, "Neutron imaging with lithium indium diselenide: Surface properties, spatial resolution, and computed tomography," *Nuclear Instruments and Methods in Physics Research A*, vol. 872, pp. 181–186, Nov. 2017. xiii, 44, 45

[94] E. Herrera, D. Hamm, A. Stowe, J. Preston, B. Wiggins, A. Burger, and E. Lukosi, "Neutron imaging with timepix coupled lithium indium diselenide," *Journal of Imaging*, vol. 4, no. 1, p. 10, 2017. xiii, xv, 43, 45, 46, 66, 68

[95] M. Ohring, S. Zarrabian, and A. Grogan, *Materials Science of Thin Films.* Academic Press, second edition ed., 2002. 49

[96] K. Zanio, W. Akutagawa, and J. W. Mayer, "Transport properties of semiinsulating cdte using nuclear particles," *Applied Physics Letters*, vol. 11, no. 1, pp. 5–7, 1967. 53

[97] C. Hurtes, M. Boulou, A. Mitonneau, and D. Bois, "Deep-level spectroscopy in high-resistivity materials," *Applied Physics Letters*, vol. 32, no. 12, pp. 821–823, 1978. 57

[98] J. Balland, J. Zielinger, M. Tapiero, J. Gross, and C. Noguet, "Investigation of deep levels in high-resistivity bulk materials by photo-induced current transient spectroscopy. ii. evaluation of various signal processing methods," *Journal of Physics D: Applied Physics*, vol. 19, no. 1, p. 71, 1986. 58

[99] S. Takeshita, *Modeling of space-charge-limited current injection incorporating an advanced model of the Poole-Frenkel effect.* PhD thesis, Clemson University, 2008. xiv, 64

[100] R. W. Finlay, C. E. Brient, D. E. Carter, A. Marcinkowski, S. Mellema, G. Randers-Pehrson, and J. Rapaport, "The ohio university beam swinger facility," *Nuclear Instruments and Methods in Physics Research*, vol. 198, pp. 197–206, July 1982. 67

[101] Z. Meisel, C. R. Brune, S. M. Grimes, D. C. Ingram, T. N. Massey, and A. V. Voinov, "The edwards accelerator laboratory at ohio university," *Physics Procedia*, vol. 90, pp. 448–454, 2017. xv, 67, 69

[102] P. Vontobel, E. H. Lehmann, R. Hassanein, and G. Frei, "Neutron tomography: Method and applications," *Physica B Condensed Matter*, vol. 385, pp. 475–480, Nov. 2006. 70

[103] S. H. Williams, A. Hilger, N. Kardjilov, I. Manke, M. Strobl, P. A. Douissard, T. Martin, H. Riesemeier, and J. Banhart, "Detection system for microimaging with neutrons," *Journal of Instrumentation*, vol. 7, p. 2014, Feb. 2012. xv, 71, 73

[104] E. D. Lukosi, D. Hamm, M. Rust, A. C. Stowe, B. Wiggins, and A. Burger, eds., *Design of High-Spatial Resolution Neutron Imager using Single Crystal Lithium Indium Diselenide*, IEEE NSS-MIC, Nov. 2015. 80

[105] K. Zanio, W. Akutagawa, and R. Kikuchi, "Transient Currents in Semi-Insulating CdTe Characteristic of Deep Traps," *Journal of Applied Physics*, vol. 39, no. 6, pp. 2818–2828, 1968. 85

[106] D. A. Brown, M. B. Chadwick, R. Capote, A. C. Kahler, A. Trkov, M. W. Herman, A. A. Sonzogni, Y. Danon, A. D. Carlson, M. Dunn, D. L. Smith, G. M. Hale, G. Arbanas, R. Arcilla, C. R. Bates, B. Beck, B. Becker, F. Brown, R. J. Casperson, J. Conlin, D. E. Cullen, M.-A. Descalle, R. Firestone, T. Gaines, K. H. Guber, A. I. Hawari, J. Holmes, T. D. Johnson, T. Kawano, B. C. Kiedrowski, A. J. Koning, S. Kopecky, L. Leal, J. P. Lestone, C. Lubitz, J. I. Márquez Damián, C. M. Mattoon, E. A. McCutchan, S. Mughabghab, P. Navratil, D. Neudecker, G. P. A. Nobre, G. Noguere, M. Paris, M. T. Pigni, A. J. Plompen, B. Pritychenko, V. G. Pronyaev, D. Roubtsov, D. Rochman, P. Romano, P. Schillebeeckx, S. Simakov, M. Sin, I. Sirakov, B. Sleaford, V. Sobes, E. S. Soukhovitskii, I. Stetcu, P. Talou, I. Thompson, S. van der Marck, L. Welser-Sherrill, D. Wiarda, M. White, J. L. Wormald, R. Q. Wright, M. Zerkle, G. Žerovnik, and Y. Zhu, "Endf/b-viii.0: The 8th major release of the nuclear reaction data library with cielo-project cross sections, new standards and thermal scattering data," *Nuclear Data Sheets*, vol. 148, pp. 1–142, Feb. 2018. 121

[107] M. B. Chadwick, P. Obložinský, M. Herman, N. M. Greene, R. D. McKnight, D. L. Smith, P. G. Young, R. E. MacFarlane, G. M. Hale, S. C. Frankle, A. C. Kahler, T. Kawano, R. C. Little, D. G. Madland, P. Moller, R. D. Mosteller, P. R. Page, P. Talou, H. Trellue, M. C. White, W. B. Wilson, R. Arcilla, C. L. Dunford, S. F. Mughabghab, B. Pritychenko, D. Rochman, A. A. Sonzogni, C. R. Lubitz, T. H. Trumbull, J. P. Weinman, D. A. Brown, D. E. Cullen, D. P. Heinrichs, D. P. McNabb, H. Derrien, M. E. Dunn, N. M. Larson, L. C. Leal, A. D. Carlson, R. C. Block, J. B. Briggs, E. T. Cheng, H. C. Huria, M. L. Zerkle, K. S. Kozier, A. Courcelle, V. Pronyaev, and S. C. van der Marck, "Endf/b-vii.0: Next generation evaluated nuclear data library

for nuclear science and technology," *Nuclear Data Sheets*, vol. 107, pp. 2931–3060, Dec. 2006.

[108] M. B. Chadwick, M. Herman, P. Obložinský, M. E. Dunn, Y. Danon, A. C. Kahler, D. L. Smith, B. Pritychenko, G. Arbanas, R. Arcilla, R. Brewer, D. A. Brown, R. Capote, A. D. Carlson, Y. S. Cho, H. Derrien, K. Guber, G. M. Hale, S. Hoblit, S. Holloway, T. D. Johnson, T. Kawano, B. C. Kiedrowski, H. Kim, S. Kunieda, N. M. Larson, L. Leal, J. P. Lestone, R. C. Little, E. A. McCutchan, R. E. MacFarlane, M. MacInnes, C. M. Mattoon, R. D. McKnight, S. F. Mughabghab, G. P. A. Nobre, G. Palmiotti, A. Palumbo, M. T. Pigni, V. G. Pronyaev, R. O. Sayer, A. A. Sonzogni, N. C. Summers, P. Talou, I. J. Thompson, A. Trkov, R. L. Vogt, S. C. van der Marck, A. Wallner, M. C. White, D. Wiarda, and P. G. Young, "Endf/b-vii.1 nuclear data for science and technology: Cross sections, covariances, fission product yields and decay data," *Nuclear Data Sheets*, vol. 112, pp. 2887–2996, Dec. 2011.

[109] A. C. Kahler, R. E. MacFarlane, R. D. Mosteller, B. C. Kiedrowski, S. C. Frankle, M. B. Chadwick, R. D. McKnight, R. M. Lell, G. Palmiotti, H. Hiruta, M. Herman, R. Arcilla, S. F. Mughabghab, J. C. Sublet, A. Trkov, T. H. Trumbull, and M. Dunn, "Endf/b-vii.1 neutron cross section data testing with critical assembly benchmarks and reactor experiments," *Nuclear Data Sheets*, vol. 112, pp. 2997–3036, Dec. 2011. 121

[110] O. Frisch, "British atomic energy report," *BR-49*, vol. 65, 1944. 126

[111] P. N. Luke, "Single-polarity charge sensing in ionization detectors using coplanar electrodes," *Applied Physics Letters*, vol. 65, no. 22, pp. 2884–2886, 1994. 126

[112] P. Luke, "Unipolar charge sensing with coplanar electrodes-application to semiconductor detectors," *IEEE Transactions on Nuclear Science*, vol. 42, no. 4, pp. 207–213, 1995.

[113] P. Luke, "Electrode configuration and energy resolution in gamma-ray detectors," *Nuclear Instruments and Methods in Physics Research Section A: Accelerators, Spectrometers, Detectors and Associated Equipment*, vol. 380, no. 1-2, pp. 232–237, 1996. 126

[114] T. H. Prettyman, K. D. Ianakiev, S. A. Soldner, and C. Szeles, "Effect of differential bias on the transport of electrons in coplanar grid cdznte detectors," *Nuclear Instruments and Methods in Physics Research A*, vol. 476, pp. 658–664, Jan. 2002. 126

[115] B. W. Sturm, *Gamma-ray spectroscopy using depth-sensing coplanar grid cadmium zinc tellurium semiconductor detectors.* PhD thesis, University of Michigan, 2007.

[116] J. M. Perez, Z. He, and D. Webe, "Stability and characteristics of large czt coplanar electrode detectors," *IEEE Transactions on Nuclear Science*, vol. 48, pp. 272–277, June 2001.

[117] P. N. Luke, J. S. Lee, M. Amman, and K. M. Yu, "Noise reduction in cdznte coplanar-grid detectors," *IEEE Transactions on Nuclear Science*, vol. 49, pp. 1950–1953, Aug. 2002.

[118] P. N. Luke, M. Amman, J. S. Lee, and H. Yaver, "Coplanar-grid cdznte detector with three-dimensional position sensitivity," *Nuclear Instruments and Methods in Physics Research A*, vol. 439, pp. 611–618, Jan. 2000. 135

[119] P. N. Luke, M. Amman, J. S. Lee, B. A. Ludewigt, and H. Yaver, "A cdznte coplanar-grid detector array for environmental remediation," *Nuclear Instruments and Methods in Physics Research A*, vol. 458, pp. 319–324, Feb. 2001.

[120] Z. He, G. F. Knoll, D. K. Wehe, and J. Miyamoto, "Position-sensitive single carrier cdznte detectors," *Nuclear Instruments and Methods in Physics Research A*, vol. 388, pp. 180–185, Feb. 1997.

[121] Z. He, G. F. Knoll, D. K. Wehe, and Y. F. Du, "Coplanar grid patterns and their effect on energy resolution of cdznte detectors," *Nuclear Instruments and Methods in Physics Research A*, vol. 411, pp. 107–113, Feb. 1998. 126, 135

[122] A. U. Manual, *Silvaco*, 2010. 127

[123] M. Amman and P. N. Luke, "Optimization criteria for coplanar-grid detectors," *IEEE Transactions on Nuclear Science*, vol. 46, pp. 205–212, June 1999. 127

Appendices
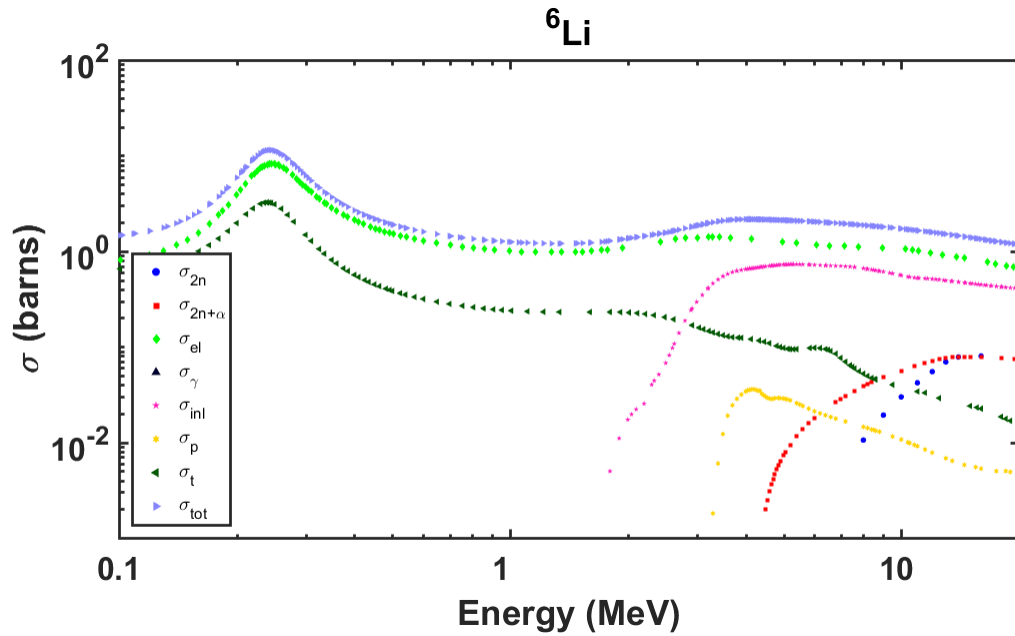
A Fast Neutron Reaction Cross-sections

A.1 Lithium

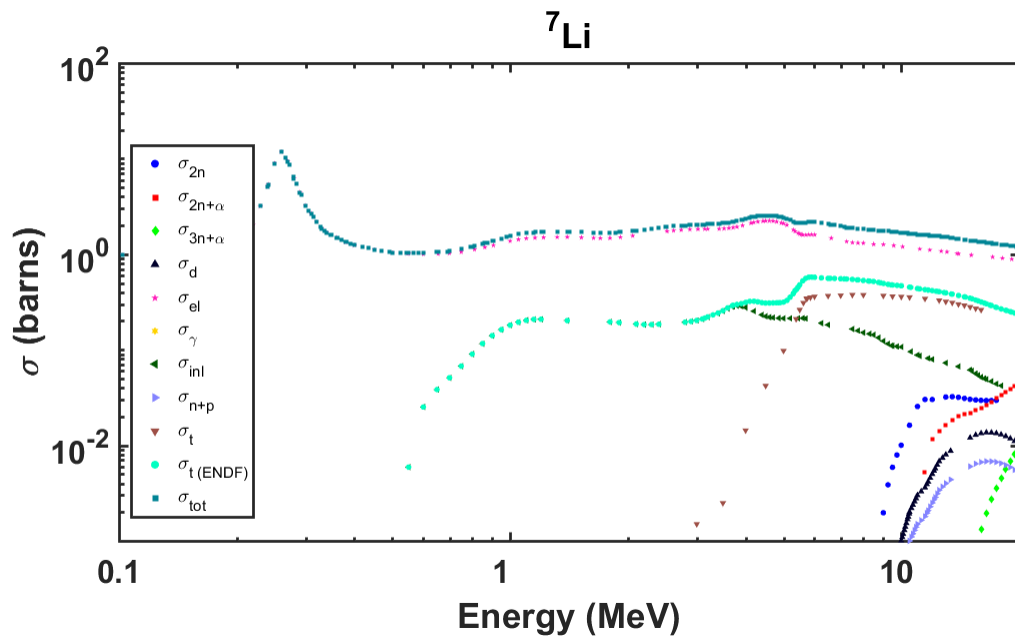**Figure A.1:** Fast neutron reaction cross-sections for ^{6}Li.

Figure A.2: Fast neutron reaction cross-sections for ^{7}Li.
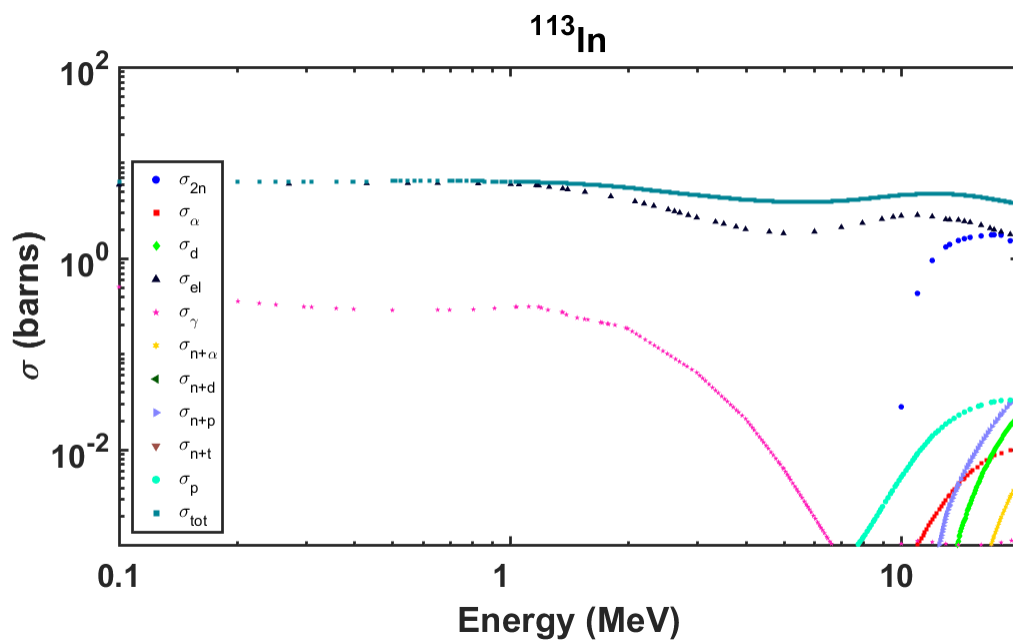
A.2   Indium

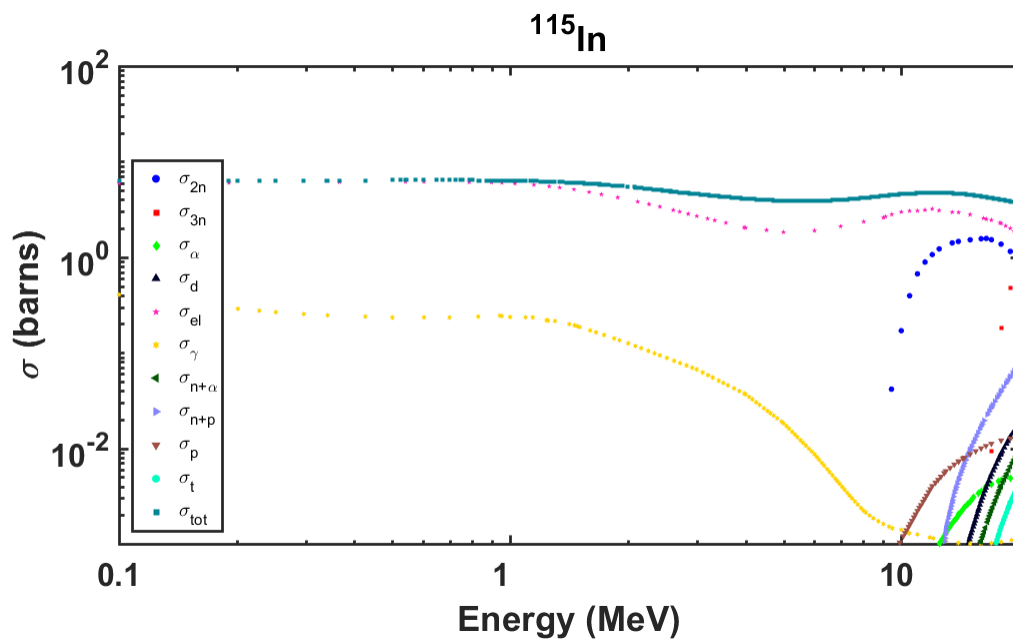**Figure A.3:** Fast neutron reaction cross-sections for ^{113}In.

Figure A.4: Fast neutron reaction cross-sections for ^{115}In.
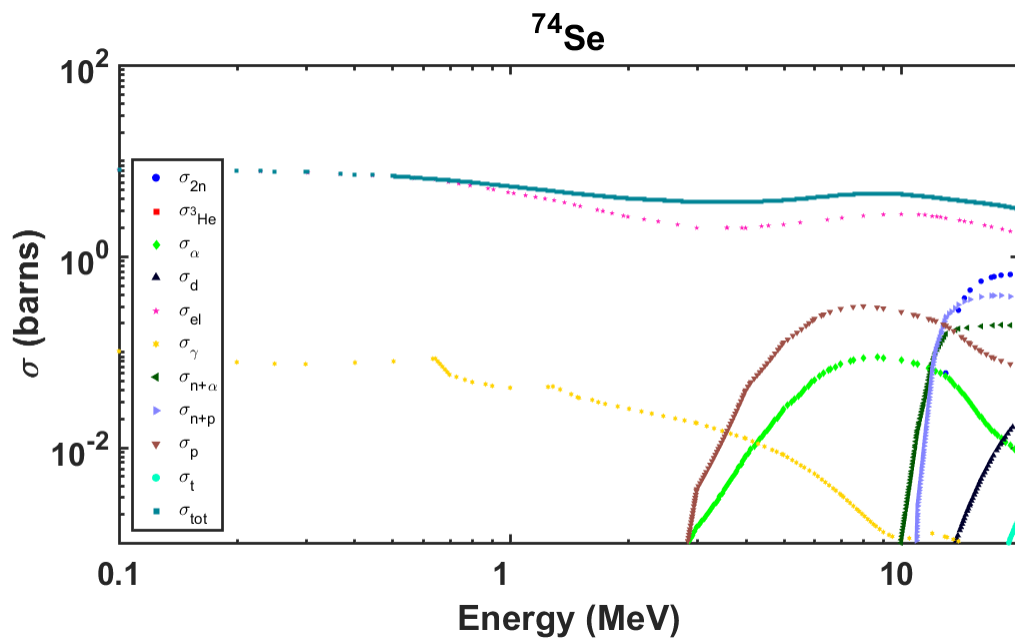
A.3 Selenium

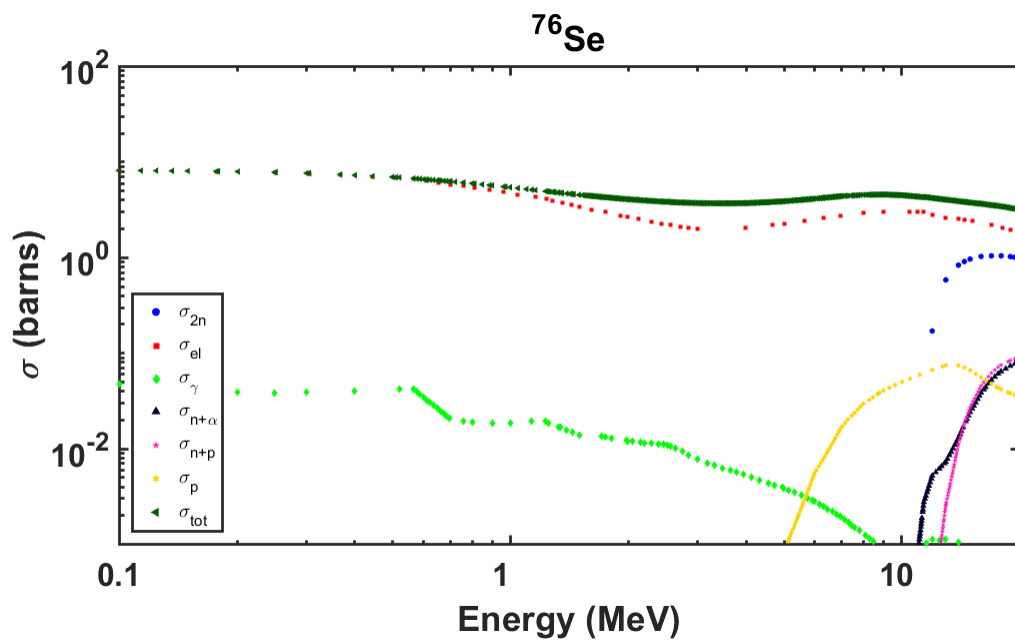**Figure A.5:** Fast neutron reaction cross-sections for ^{74}Se.

Figure A.6: Fast neutron reaction cross-sections for ^{76}Se.
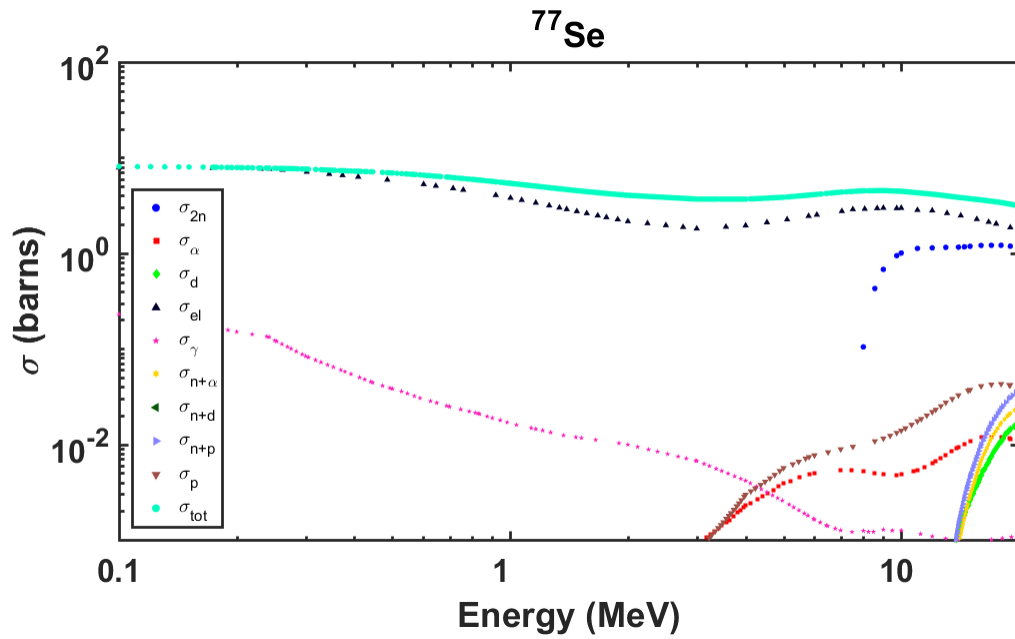
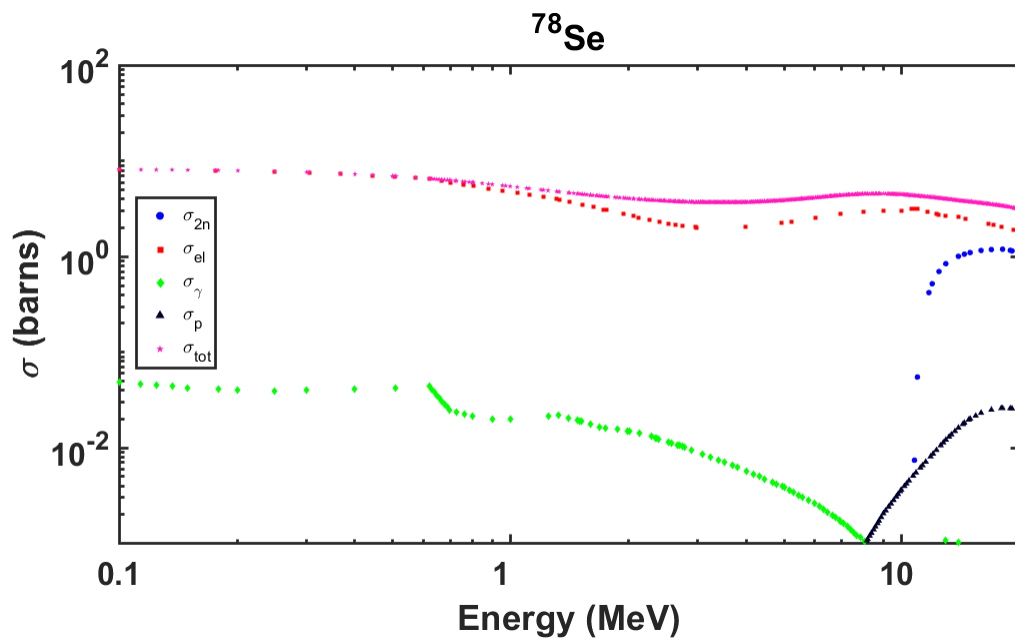**Figure A.7:** Fast neutron reaction cross-sections for ^{77}Se.

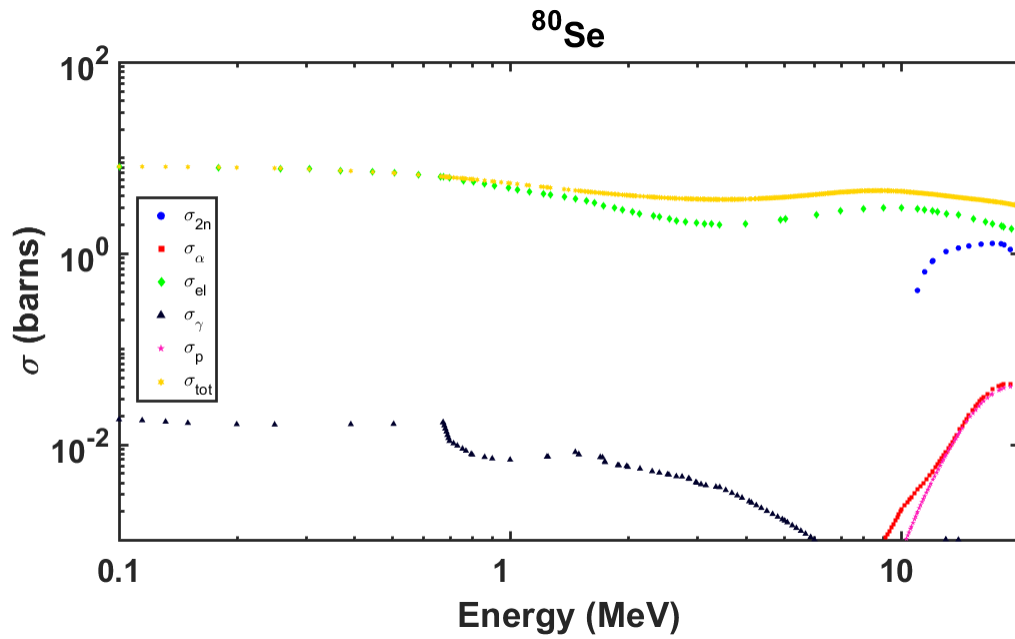**Figure A.8:** Fast neutron reaction cross-sections for ^{78}Se.

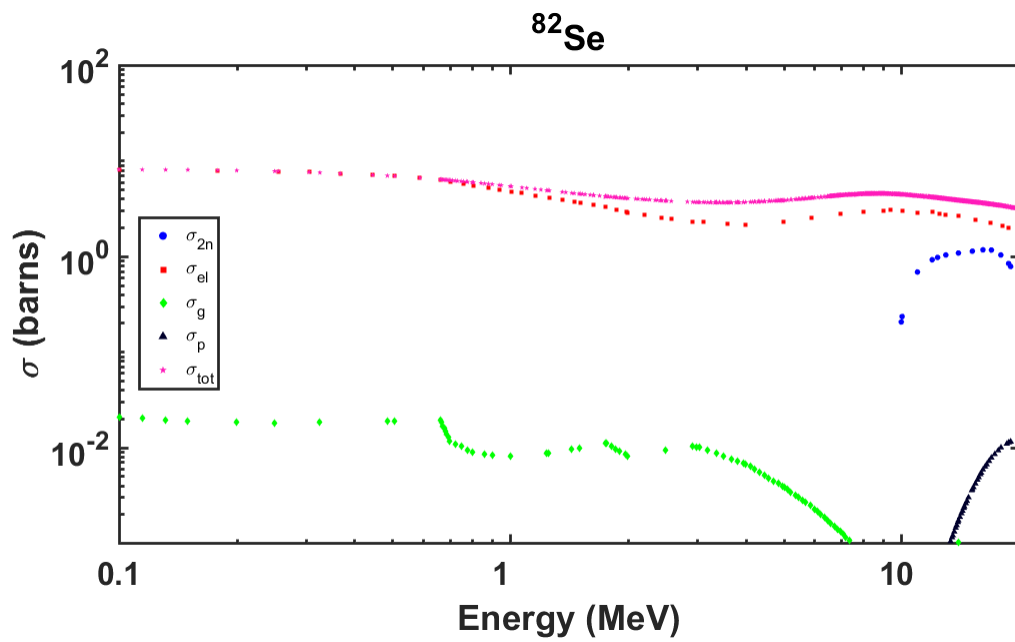**Figure A.9:** Fast neutron reaction cross-sections for ^{80}Se.

Figure A.10: Fast neutron reaction cross-sections for ^{82}Se.

A.4   Total

The total macroscopic cross section, Σ_{tot} is calculated from the microscopic cross sections, σ, density ($\rho = 4.47\,\mathrm{g/cm^{-3}}$), molecular weight, ($M = 279.07\,\mathrm{g/mol}$), and isotopic composition of LISe. The primary isotopes found in enriched LISe and their isotopic abundances are ^{6}Li (95%), ^{7}Li (5%), ^{113}In (4.3%), ^{113}In (95.7%), ^{74}Se (0.86%), ^{76}Se (9.23%), ^{77}Se (7.6%), ^{78}Se (23.69%), ^{80}Se (49.80%), and ^{82}Se (8.82%) where In and Se are in accordance with their natural isotopic abundance. The total macroscopic cross section for each isotope, $\Sigma_{tot}(X)$, is given by

$$\Sigma_{tot}(X) = N_X \sigma_{tot} \tag{1}$$

where σ_{tot} is the summation of the neutron interaction cross-sections for isotope X, as shown in Figures A.1 - A.10, which were acquired from the Evaluated Nuclear Data File [106–109]. The atomic density of each isotope in LISe, N_X, is given by the equation

$$N_X = \frac{\rho N_A}{M}[a/o(X)] \tag{2}$$

where ρ is the density in $\mathrm{g/cm^3}$, N_A is Avogadro's constant (6.023×10^{23} atoms/mol), M is the total molar weight of the molecular species, and $a/o(X)$ is the atom fraction of isotope X in the molecular unit. LISe is composed of approximately 25% Li, 25% In, and 50% Se so the isotopic abundances for each element is weighted according to these fractions to give the atom fraction of each isotope with respect to LISe. Therefore, N_X for each isotope is

$$
\begin{aligned}
N_{^6\mathrm{Li}} &= \frac{(4.47\,\mathrm{g/cm^3})\,(0.6023 \times 10^{-24}\,\mathrm{atoms/mol})}{279.07\,\mathrm{g/mol}}[(0.25)\,(0.95)] \\
&= 2.29 \times 10^{21}\,\mathrm{atoms/cm^3}
\end{aligned} \tag{3}
$$

$$
\begin{aligned}
N_{^7\mathrm{Li}} &= \frac{(4.47\,\mathrm{g/cm^3})\,(0.6023 \times 10^{-24}\,\mathrm{atoms/mol})}{279.07\,\mathrm{g/mol}}[(0.25)\,(0.05)] \\
&= 0.12 \times 10^{21}\,\mathrm{atoms/cm^3}
\end{aligned} \tag{4}
$$

$$N_{^{113}\text{In}} = \frac{(4.47\,\text{g/cm}^3)\,(0.6023 \times 10^{-24}\,\text{atoms/mol})}{279.07\,\text{g/mol}}\,[(0.25)\,(0.043)]$$

$$= 0.10 \times 10^{21}\,\text{atoms/cm}^3$$

(5)

$$N_{^{115}\text{In}} = \frac{(4.47\,\text{g/cm}^3)\,(0.6023 \times 10^{-24}\,\text{atoms/mol})}{279.07\,\text{g/mol}}\,[(0.25)\,(0.957)]$$

$$= 2.31 \times 10^{21}\,\text{atoms/cm}^3$$

(6)

$$N_{^{74}\text{Se}} = \frac{(4.47\,\text{g/cm}^3)\,(0.6023 \times 10^{-24}\,\text{atoms/mol})}{279.07\,\text{g/mol}}\,[(0.25)\,(0.0086)]$$

$$= 0.04 \times 10^{21}\,\text{atoms/cm}^3$$

(7)

$$N_{^{76}\text{Se}} = \frac{(4.47\,\text{g/cm}^3)\,(0.6023 \times 10^{-24}\,\text{atoms/mol})}{279.07\,\text{g/mol}}\,[(0.25)\,(0.0.923)]$$

$$= 0.45 \times 10^{21}\,\text{atoms/cm}^3$$

(8)

$$N_{^{77}\text{Se}} = \frac{(4.47\,\text{g/cm}^3)\,(0.6023 \times 10^{-24}\,\text{atoms/mol})}{279.07\,\text{g/mol}}\,[(0.25)\,(0.076)]$$

$$= 0.37 \times 10^{21}\,\text{atoms/cm}^3$$

(9)

$$N_{^{78}\text{Se}} = \frac{(4.47\,\text{g/cm}^3)\,(0.6023 \times 10^{-24}\,\text{atoms/mol})}{279.07\,\text{g/mol}}\,[(0.25)\,(0.2369)]$$

$$= 1.14 \times 10^{21}\,\text{atoms/cm}^3$$

(10)

$$N_{^{80}\text{Se}} = \frac{(4.47\,\text{g/cm}^3)\,(0.6023 \times 10^{-24}\,\text{atoms/mol})}{279.07\,\text{g/mol}}\,[(0.25)\,(0.498)]$$

$$= 2.40 \times 10^{21}\,\text{atoms/cm}^3$$

(11)

$$N_{^{82}\text{Se}} = \frac{(4.47\,\text{g/cm}^3)\,(0.6023 \times 10^{-24}\,\text{atoms/mol})}{279.07\,\text{g/mol}}\,[(0.25)\,(0.0882)] \tag{12}$$

$$= 0.43 \times 10^{21}\,\text{atoms/cm}^3$$

Finally, the macroscopic cross section at a given neutron energy can be calculated in the following manner.

$$\begin{aligned}
\Sigma_{tot}(\text{LISe}) = {} & N_{^6\text{Li}}\,\sigma_{tot}(^6\text{Li}) \,+\, N_{^7\text{Li}}\,\sigma_{tot}(^7\text{Li}) \\
& + N_{^{113}\text{In}}\,\sigma_{tot}(^{113}\text{In}) \,+\, N_{^{115}\text{In}}\,\sigma_{tot}(^{115}\text{In}) \\
& + N_{^{74}\text{Se}}\,\sigma_{tot}(^{74}\text{Se}) \,+\, N_{^{76}\text{Se}}\,\sigma_{tot}(^{76}\text{Se}) \\
& + N_{^{77}\text{Se}}\,\sigma_{tot}(^{77}\text{Se}) \,+\, N_{^{78}\text{Se}}\,\sigma_{tot}(^{78}\text{Se}) \\
& + N_{^{80}\text{Se}}\,\sigma_{tot}(^{80}\text{Se}) \,+\, N_{^{82}\text{Se}}\,\sigma_{tot}(^{82}\text{Se})
\end{aligned} \tag{13}$$

In order for a neutron interaction to be detectable, the reaction products must deposit enough energy into the detector to record a pulse above a given threshold. Absorption reactions that produce heavy charged particles with sufficiently short ranges (less than the dimensions of the detector) are generally detectable events. In elastic scattering reactions, the energy transferred from the neutron (E_n) to the target nucleus (E_R) is given by the equation,

$$E_R = \frac{4A}{(1+A)^2}\,\left(cos^2\theta\right) E_n \tag{14}$$

where A is the atomic mass of the target nucleus and θ is the scattering angle in the lab reference frame. Therefore, the total energy transferred to the target nucleus is inversely proportional to the atomic mass of the recoiling target nucleus. As such, little energy is transferred to the In $(E_{max} \approx 0.035 E_n)$ and Se $(E_max \approx 0.05 E_n)$ isotopes. Conversely, an incident neutron can transfer up to 48.98% and 43.75% of its kinetic energy to ^{6}Li and ^{7}Li nuclei, respectively. Similarly, inelastic scattering reactions are only relevant for ^{6}Li where the recoiling nucleus decays into $d + \alpha$. Thus, the detectable macroscopic cross-section, Σ_{det},

is the summation of the subset of reactions that deposit energy within the detector volume, as shown in Figure A.11. For 9 MeV neutrons from the d(d,n) reaction used in the fast neutron imaging study in Section 6.3, the total and detectable cross sections are 0.0253 and 0.0157 cm^{-1}, respectively.

Detection efficiency, ϵ, is a function of Σ_{det} and the thickness of the sensor, d, as shown in Equation 15.

$$\epsilon = 1 - exp\left(-\Sigma_{det}d\right) \tag{15}$$

Figure A.12 depicts the relationship between detector thickness and detection efficiency for a monoenergetic 9 MeV neutron beam. For a 10 cm thick detector, the detection efficiency is 14.5%. For the 528 μm thick detector used for the fast neutron studies, the total interaction and detection efficiencies are 0.133% and 0.083%, respectively. Scattering reactions with In and Se constitute the majority of the detection efficiency losses.
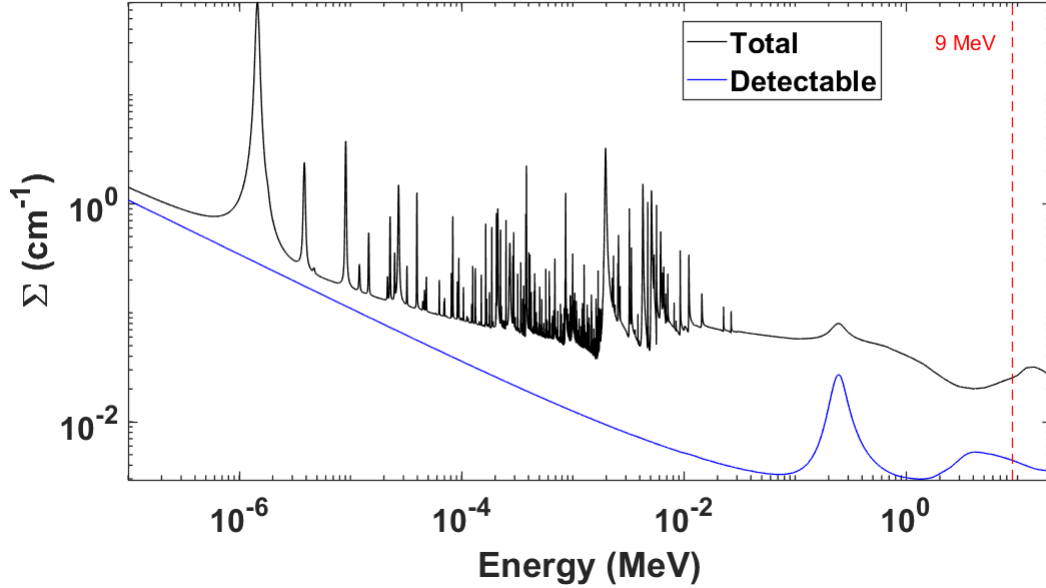
Figure A.11: Total and detectable macroscopic cross section for LISe enriched to 95% ^{6}Li content. Detectable interactions include absorption interactions with heavy charged particle products and scattering reactions with Li isotopes. The large peak in Σ_{det} comes from the elastic scattering reaction with ^{6}Li and ^{7}Li.
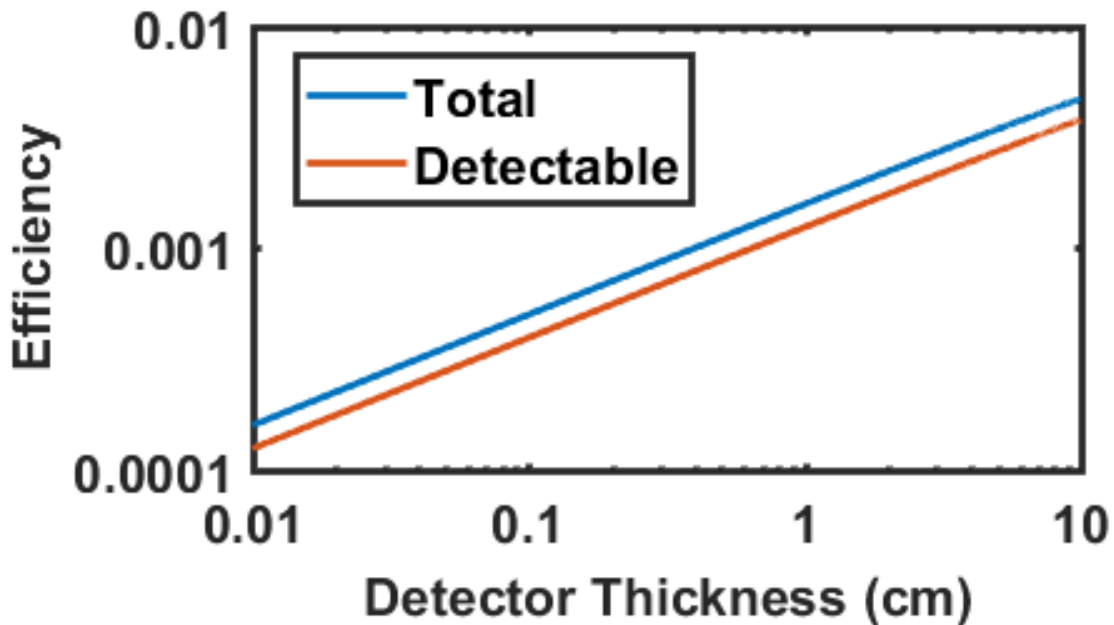

Figure A.12: Total and detectable interaction efficiency for LISe enriched to 95% ^{6}Li content. Detectable interactions include absorption interactions with heavy charged particle products and scattering reactions with Li isotopes. Efficiency loss is attributed to the In and Se scattering reactions.

B   Interdigitated Coplanar Readout

B.1   Theory of Operation

O. Frisch first introduced his unipolar charge sensing technique as a means to reduce the contribution of slow-moving ions in gas-filled ion chambers. By placing a wire mesh grid (or so-called Frisch grid) near the anode, only the electron drift near the anode would contribute to the signal increasing resolution [110]. Luke et al. introduced the interdigitated coplanar grid as a virtual Frisch grid, since placing an electrode within the bulk of a solid state detector is challenging to say the least [111–113]. These techniques rely on the principles of the Shockley-Ramo theorem, which dictates the movement of charge and the induced current these moving charges create [23, 24]. He et al. provide an excellent review of the underlying principles that drive unipolar charge sensing [27]. Several studies have employed this technique to improve the energy resolution of the widely used γ-sensitive semiconductor cadmium zinc telluride (CZT) due to the material's poor hole transport [114–121]. In short, the design consists of an anode with two sets of interdigitated strips as shown in Fig. B.1.

One grid is placed at slightly higher voltage (collecting grid) than the other (non-collecting grid). At distances far away from the cathode, the electric field appears constant, but as the charges drift closer to the anode, the weighting potential of the two electrodes diverge quickly as seen in Fig. B.2a. Subtraction of these two signals produces a signal dependent only on the more mobile electrons since all of the signal is produced very close to the anode
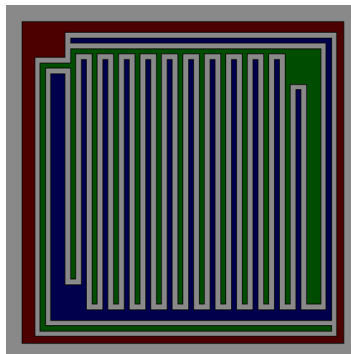

Figure B.1: Interdigitated coplanar readout contact design where blue and green 'digits' are the collecting and non-collecting grids, red is the guard ring, and silver is the bare crystal.

(See Fig. B.2b). This has the effect of increasing energy resolution at the cost of reducing signal magnitude.

B.2 Simulations

Using Silvaco, the weighting potential for various strip widths and pitches have been simulated to determine the optimum configuration [122]. These simulations demonstrate 95% of the induced signal is generated within one strip pitch of the the anode, which agrees with He [27]. It also demonstrates that the profile of the weighting potential is strongly dependent on the strip pitch and only weakly dependent on the strip width. Figures B.2a-B.16b show the three dimensional weighting potential in LISe where the collecting grid was biased at +1 V with respect to the non-collecting grid. These simulations guide the design of the interdigitated coplanar mask for LISe. There are trade offs to consider when implementing this technique for single polarity charge sensing including interdigit capacitance and surface leakage, dead layer thickness, and charge readout uniformity [123].
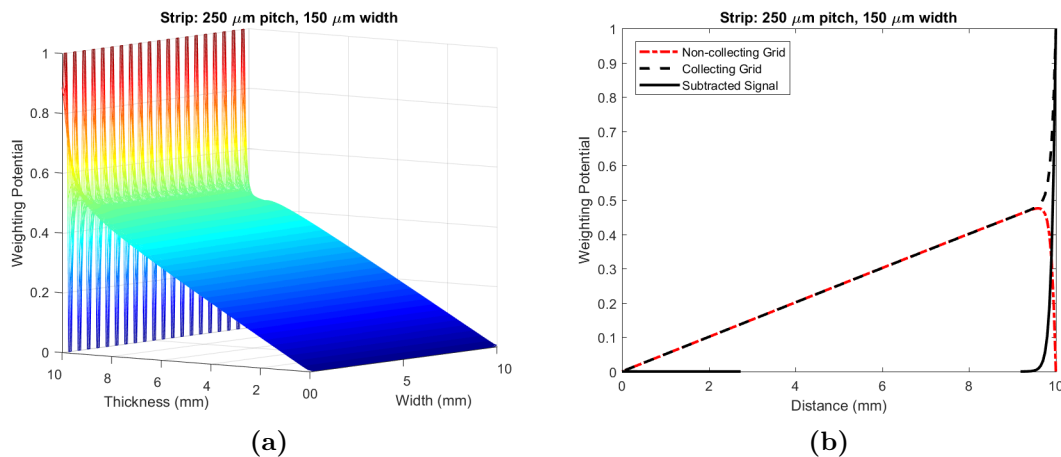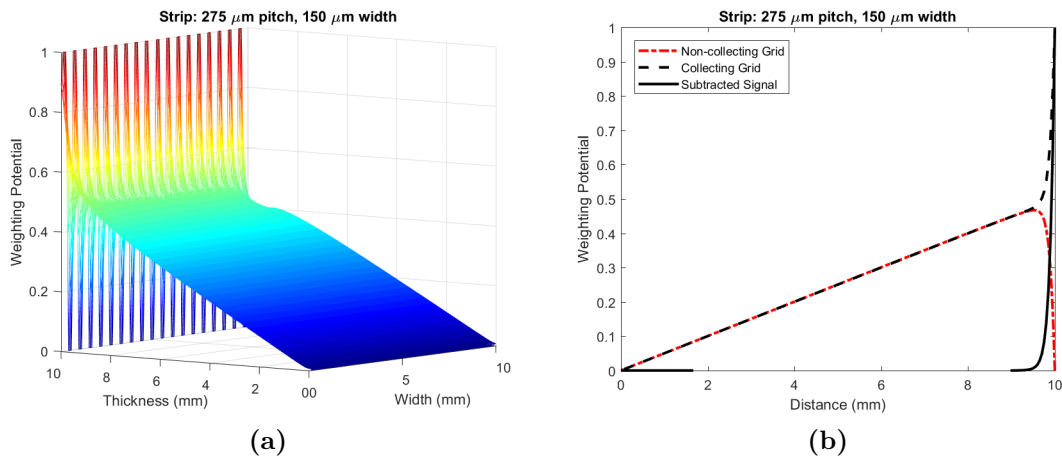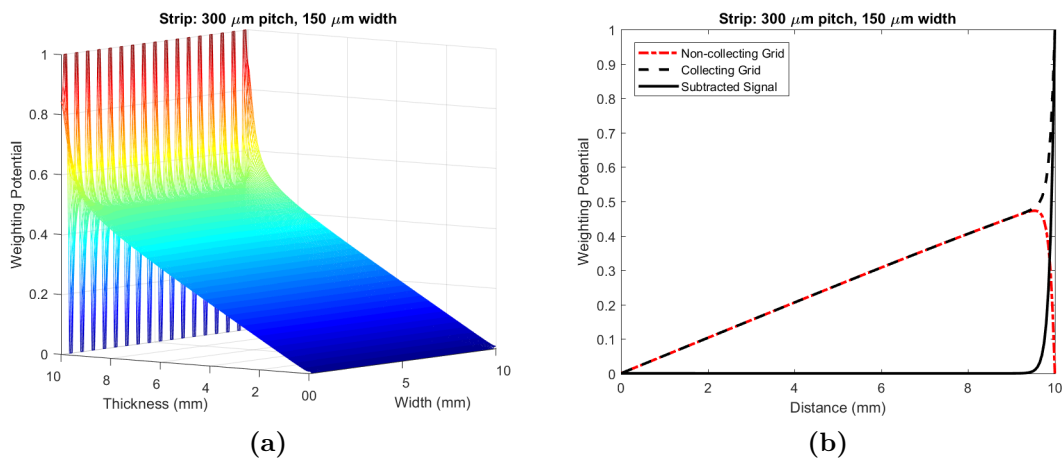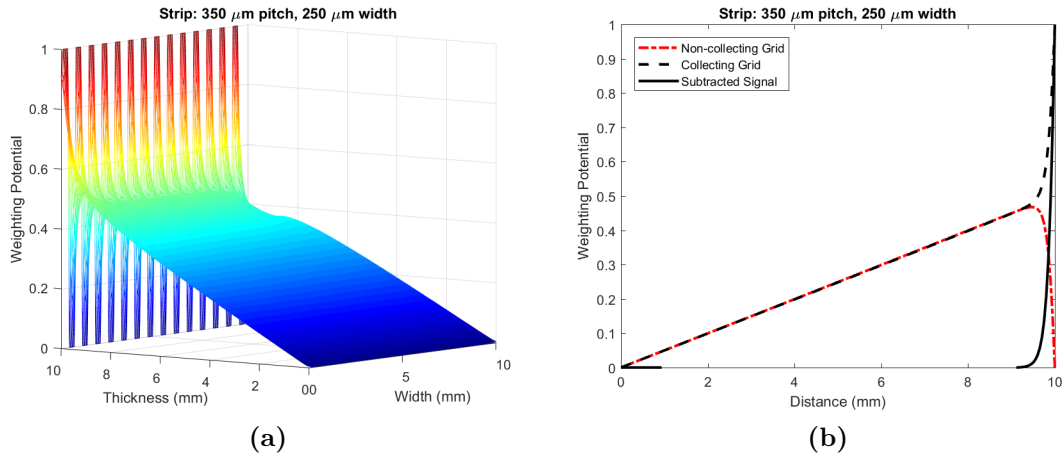

Figure B.2: (a) Three-dimensional and (b) one-dimensional view of the weighting potential within LISe for a interdigitated coplanar grid as simulated using Silvaco. The strips were $150\,\mu$m wide with $100\,\mu$m spacing and the collecting grid was biased at +1 V with respect to the non-collecting grid.
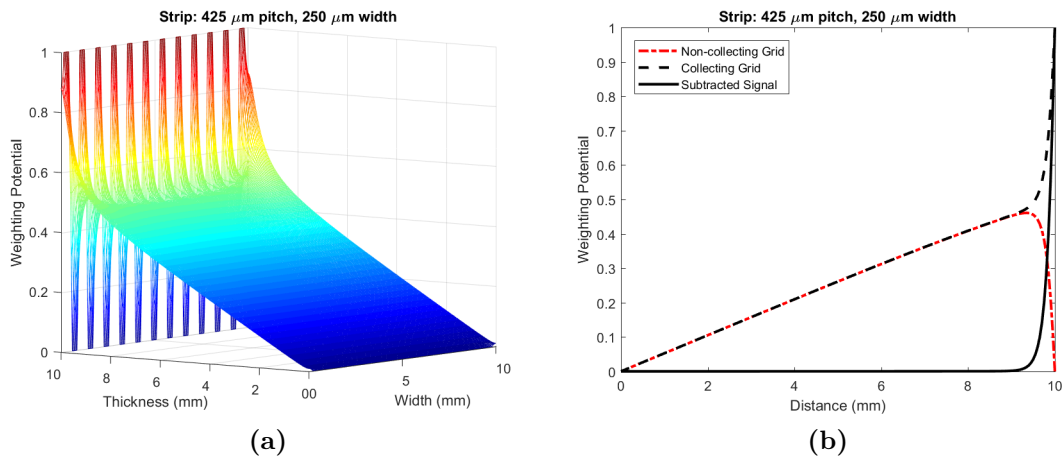
Figure B.3: (a) Three-dimensional and (b) one-dimensional view of the weighting potential within LISe for a interdigitated coplanar grid as simulated using Silvaco. The strips were $150\,\mu$m wide with $125\,\mu$m spacing and the collecting grid was biased at $+1$ V with respect to the non-collecting grid.

Figure B.4: (a) Three-dimensional and (b) one-dimensional view of the weighting potential within LISe for a interdigitated coplanar grid as simulated using Silvaco. The strips were $150\,\mu$m wide with $150\,\mu$m spacing and the collecting grid was biased at $+1$ V with respect to the non-collecting grid.
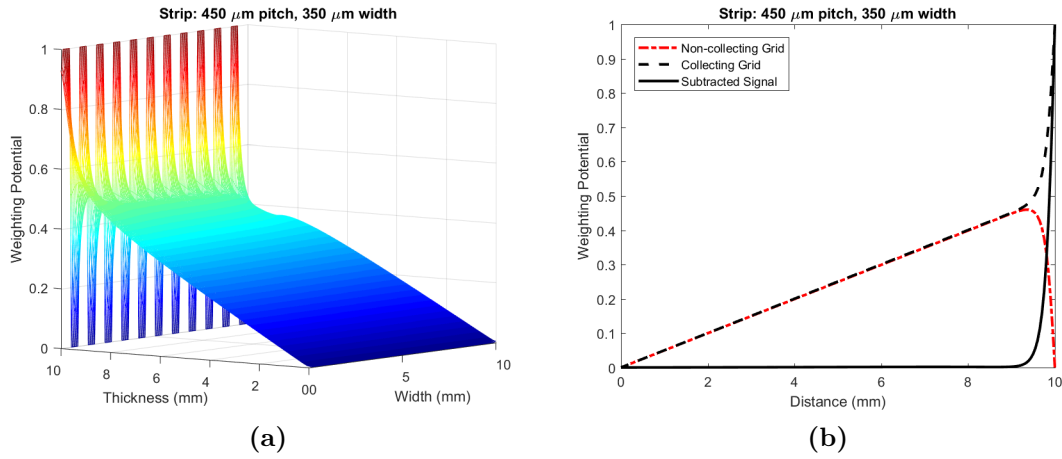
Figure B.5: (a) Three-dimensional and (b) one-dimensional view of the weighting potential within LISe for a interdigitated coplanar grid as simulated using Silvaco. The strips were $250\,\mu\text{m}$ wide with $100\,\mu\text{m}$ spacing and the collecting grid was biased at $+1$ V with respect to the non-collecting grid.
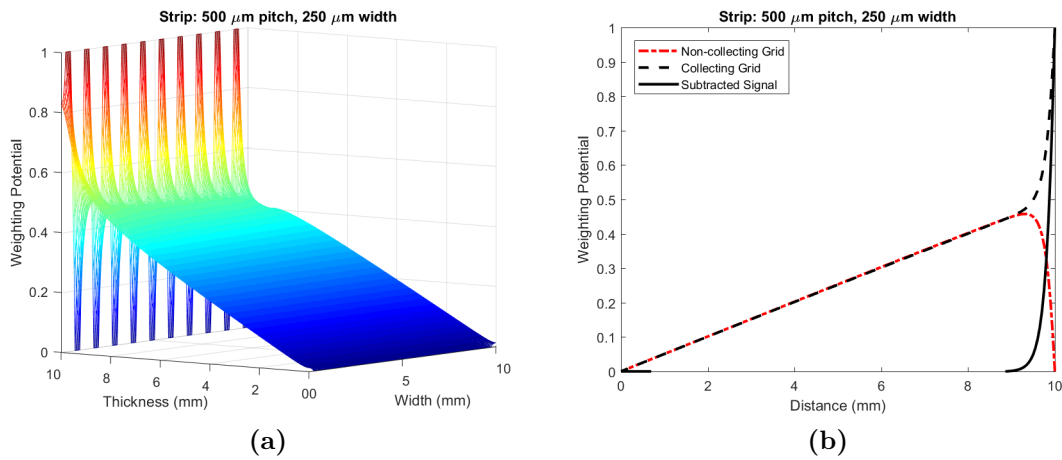

Figure B.6: (a) Three-dimensional and (b) one-dimensional view of the weighting potential within LISe for a interdigitated coplanar grid as simulated using Silvaco. The strips were $250\,\mu\text{m}$ wide with $175\,\mu\text{m}$ spacing and the collecting grid was biased at $+1$ V with respect to the non-collecting grid.
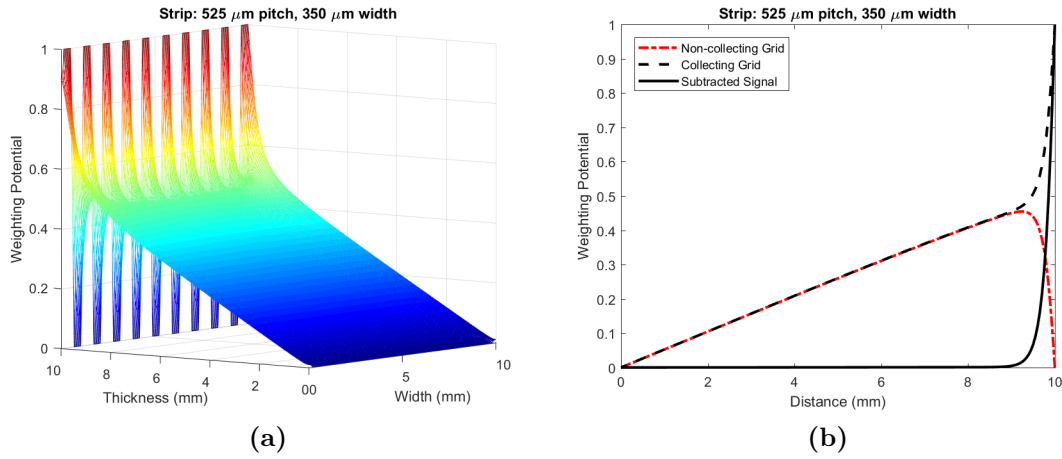
Figure B.7: (a) Three-dimensional and (b) one-dimensional view of the weighting potential within LISe for a interdigitated coplanar grid as simulated using Silvaco. The strips were $350\,\mu$m wide with $100\,\mu$m spacing and the collecting grid was biased at $+1$ V with respect to the non-collecting grid.

Figure B.8: (a) Three-dimensional and (b) one-dimensional view of the weighting potential within LISe for a interdigitated coplanar grid as simulated using Silvaco. The strips were $250\,\mu$m wide with $250\,\mu$m spacing and the collecting grid was biased at $+1$ V with respect to the non-collecting grid.
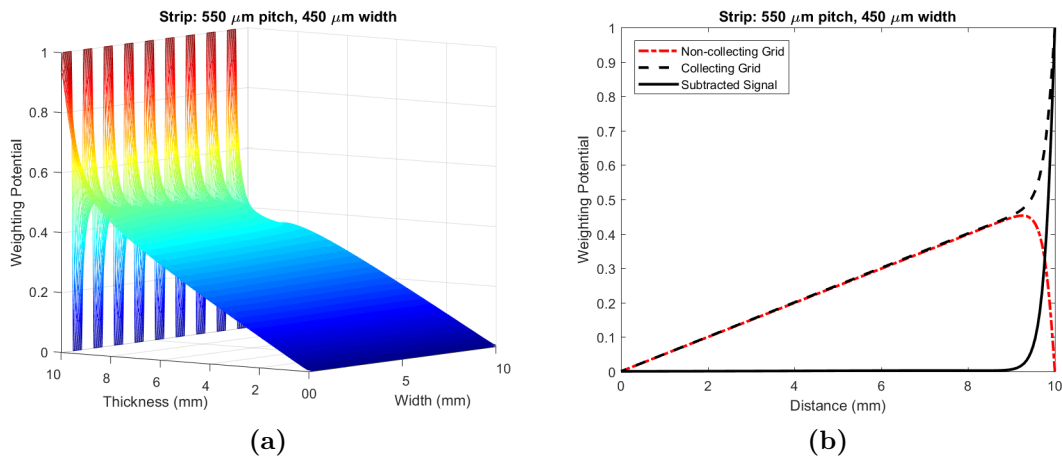
Figure B.9: (a) Three-dimensional and (b) one-dimensional view of the weighting potential within LISe for a interdigitated coplanar grid as simulated using Silvaco. The strips were $350\,\mu$m wide with $175\,\mu$m spacing and the collecting grid was biased at $+1$ V with respect to the non-collecting grid.
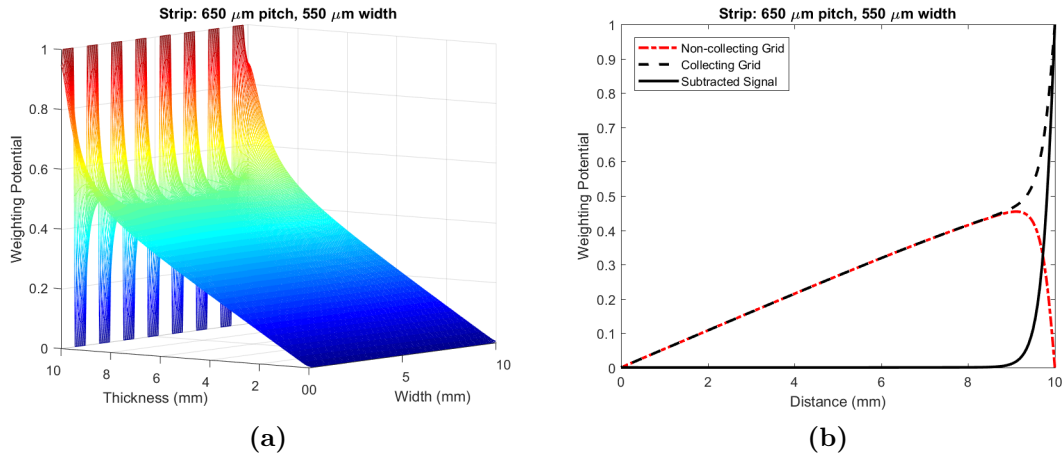

Figure B.10: (a) Three-dimensional and (b) one-dimensional view of the weighting potential within LISe for a interdigitated coplanar grid as simulated using Silvaco. The strips were $450\,\mu$m wide with $100\,\mu$m spacing and the collecting grid was biased at $+1$ V with respect to the non-collecting grid.
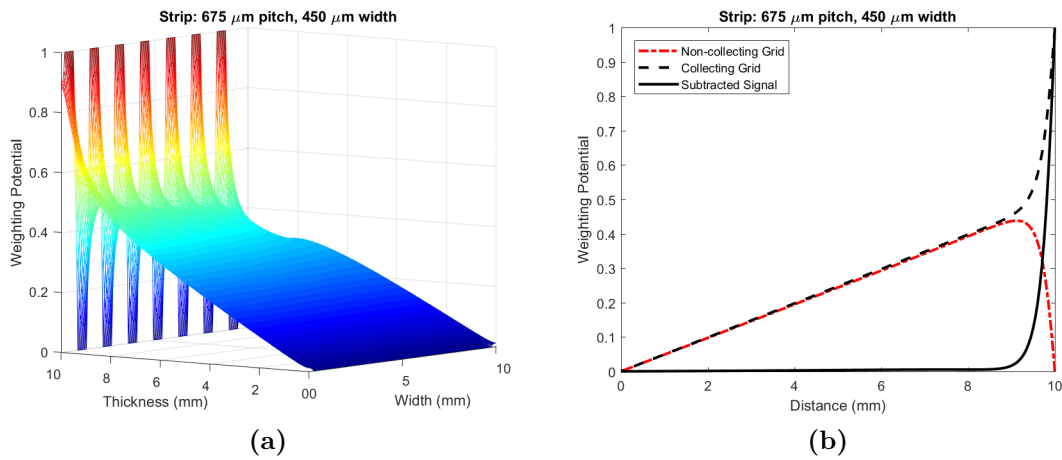
Figure B.11: (a) Three-dimensional and (b) one-dimensional view of the weighting potential within LISe for a interdigitated coplanar grid as simulated using Silvaco. The strips were $550\,\mu$m wide with $100\,\mu$m spacing and the collecting grid was biased at $+1$ V with respect to the non-collecting grid.

Figure B.12: (a) Three-dimensional and (b) one-dimensional view of the weighting potential within LISe for a interdigitated coplanar grid as simulated using Silvaco. The strips were $450\,\mu$m wide with $225\,\mu$m spacing and the collecting grid was biased at $+1$ V with respect to the non-collecting grid.
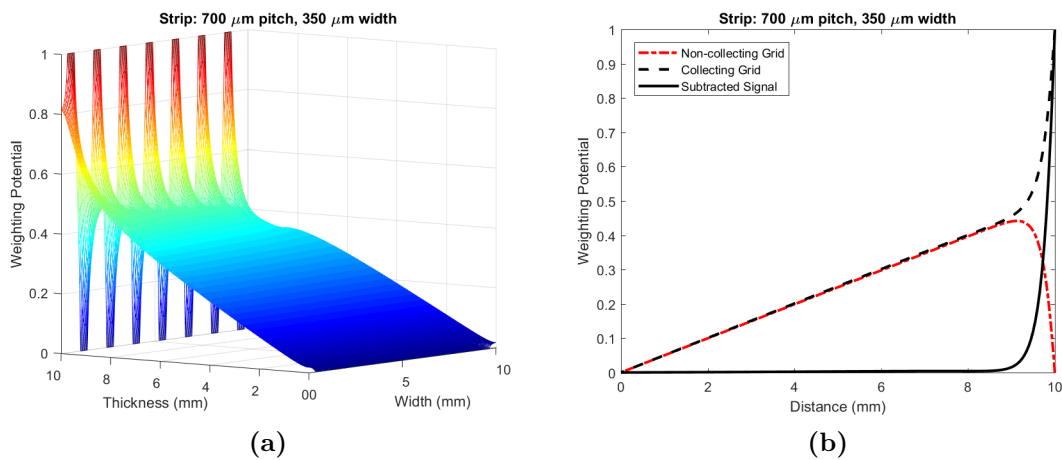
Figure B.13: (a) Three-dimensional and (b) one-dimensional view of the weighting potential within LISe for a interdigitated coplanar grid as simulated using Silvaco. The strips were $350\,\mu$m wide with $350\,\mu$m spacing and the collecting grid was biased at $+1$ V with respect to the non-collecting grid.
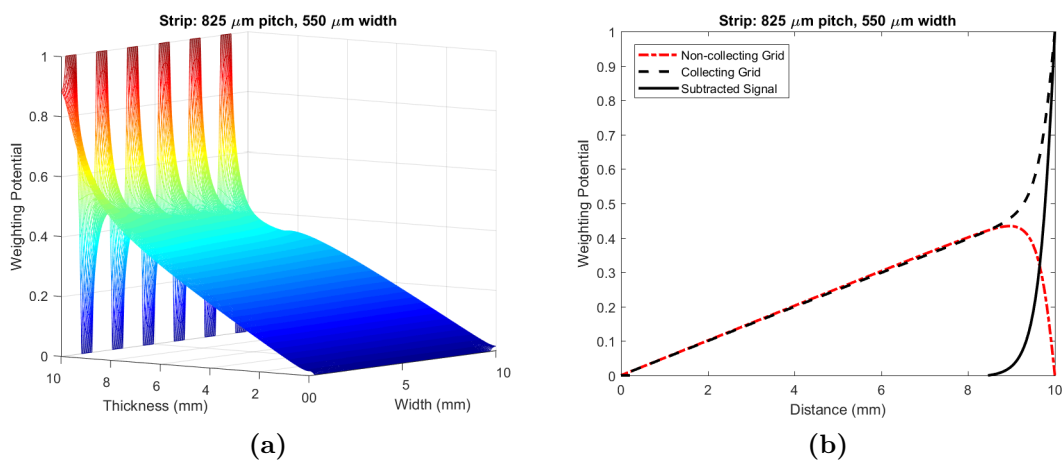

Figure B.14: (a) Three-dimensional and (b) one-dimensional view of the weighting potential within LISe for a interdigitated coplanar grid as simulated using Silvaco. The strips were $550\,\mu$m wide with $275\,\mu$m spacing and the collecting grid was biased at $+1$ V with respect to the non-collecting grid.
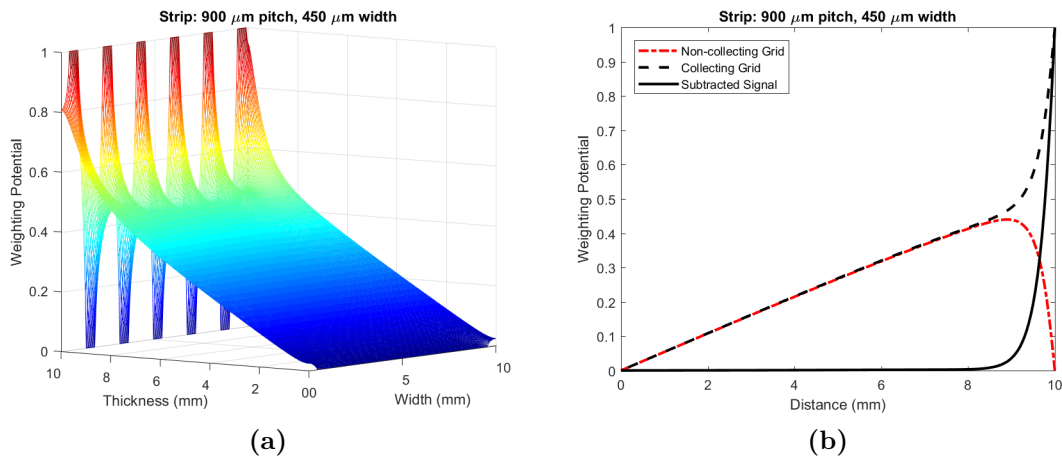
Figure B.15: (a) Three-dimensional and (b) one-dimensional view of the weighting potential within LISe for a interdigitated coplanar grid as simulated using Silvaco. The strips were $450\,\mu$m wide with $450\,\mu$m spacing and the collecting grid was biased at $+1$ V with respect to the non-collecting grid.
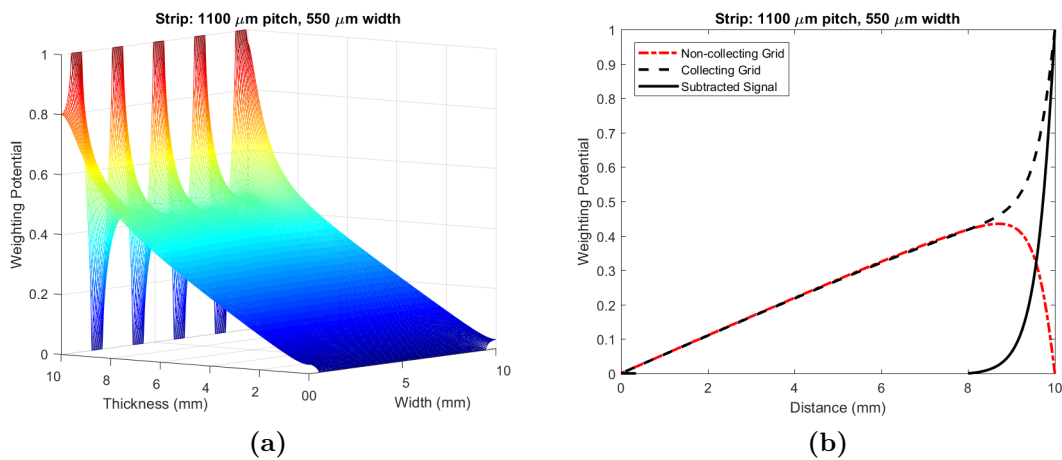

Figure B.16: (a) Three-dimensional and (b) one-dimensional view of the weighting potential within LISe for a interdigitated coplanar grid as simulated using Silvaco. The strips were $550\,\mu$m wide with $550\,\mu$m spacing and the collecting grid was biased at $+1$ V with respect to the non-collecting grid.

B.3   Shadow Mask Design and Readout Board

A shadow mask was designed in AutoCAD and manufactured via laser cutting a $1\,\text{cm}^2$ thin steel sheet with a width of $400\,\mu\text{m}$ and a pitch of $600\,\mu\text{m}$ covering a 5×5 mm^2 area, which is shown in Figure B.17. A 3rd generation device configuration was chosen, which provides uniformity in the weighting potential to compensate for edge effects [121]. While the geometric parameters of the shadow mask dictate some limitations of the individual design, further tuning of the applied bias and ΔV between the collecting and non-collecting grids can be used to optimize the performance of the energy resolution of the detector. Furthermore, electron trapping can degrade the spectral performance of a detector through a depth dependent charge collection efficiency effect. To combat this deleterious effect, only a portion of the non-collecting grid's signal may be subtracted, which effectively removes the position dependency since the magnitude of the non-collecting grid signal is proportional to the interaction depth. Additionally, a digital correction may be applied by also collecting the cathode signal to determine the depth of interaction and applying a correction factor to the collecting grid signal [118].

Using EAGLE, a detector board has been designed and fabricated as shown in Figure B.18. The crystal will be mounted to the board via ultrasonic gold wire bonding. The anode signals will be conditioned using two CREMAT CR-110 preamplifers. The signals will be subtracted using a CAEN FAN IN/FAN OUT to invert the non-collecting grid signal, then sum the two signals. The resulting unipolar signal is then passed to a CAEN DT5770 Desktop Digitizer. The detector is expected to exhibit improved spectral resolution.
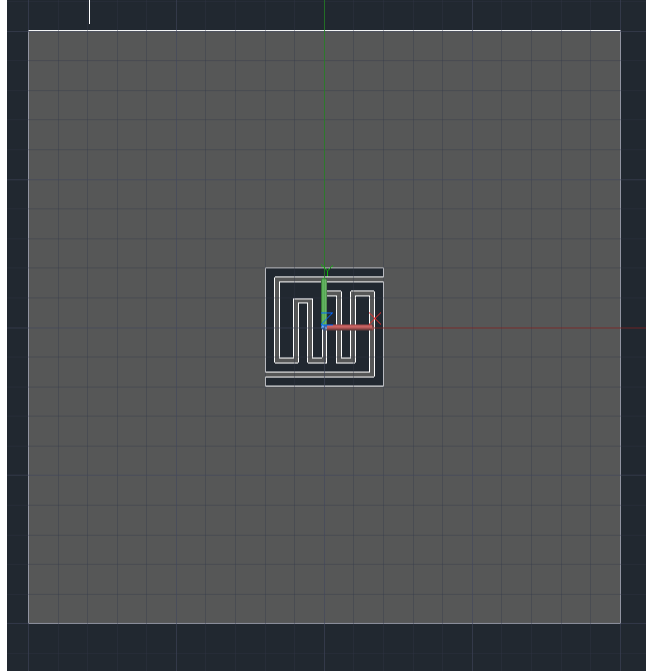
Figure B.17: CAD image of interdigitated coplanar grid shadow mask for physical vapor deposition. The strips have a width of $400\,\mu$m and a pitch of $600\,\mu$m covering a 5×5 mm^2 area.
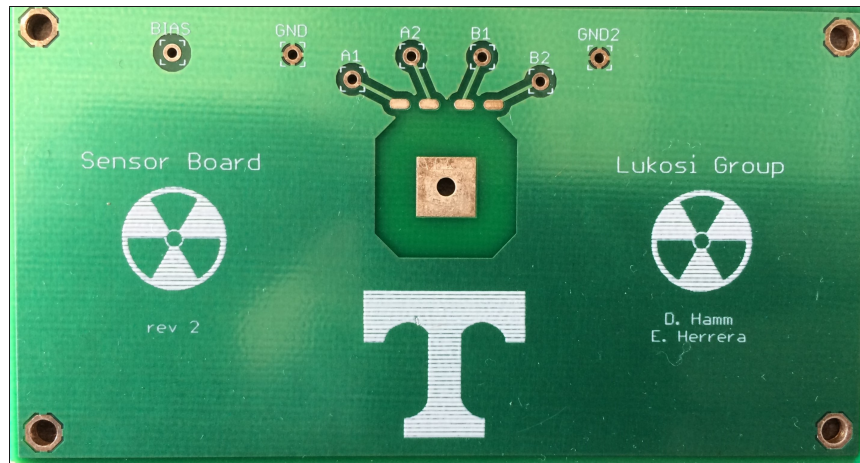

Figure B.18: Printed circuit board for a coplanar readout design with a wire bonding pads for the collecting grid, non-collecting grid, and guard ring designed in EAGLE and manufactured by Sunstone.

Vita

Daniel S. Hamm is the youngest child of Lori Perry and the late David Hamm. He was born and raised in Selmer, Tennessee where he graduated from McNairy Central High School at the top of his class. He attended the University of Tennessee, Knoxville as a member of the second cohort of Haslam Scholars where he studied Nuclear Engineering. As an undergraduate, he participated in the Nuclear Engineering Science Laboratory Synthesis internship program where he worked with the Fusion and Materials for Nuclear Science Division where developed a laser-induced breakdown spectroscopy system for beryllium identification. After completing his Bachelor of Science in Nuclear Engineering in 2014, he accepted a Nuclear Energy University Programs fellowship to continue his education at the University of Tennessee predicated on the development of a novel neutron sensitive detection material, which is the basis of this dissertation. Daniel earned a Master of Science in Nuclear Engineering in 2016 and Doctor of Philosophy in Nuclear Engineering in 2018 while specializing in radiation detector development. Daniel will be applying his knowledge and expertise as a Corp Engineering Specialist position at Consolidated Nuclear Security Y-12 National Security Complex.